Measurement of the $W \to e\nu$ cross-section in proton-proton collisions at $\sqrt{s} = 7$ TeV with the ATLAS detector at the LHC and Monte Carlo studies for $W \to \tau\nu$ observability potential

Paweł Malecki

Henryk Niewodniczański
Institute of Nuclear Physics
Polish Academy of Sciences

Thesis submitted for the Degree of Doctor of Philosophy in Physics
Prepared under the supervision of Prof. Elżbieta Richter-Wąs

Kraków, April 2011

Streszczenie

Detektor ATLAS jest największym z czterech detektorów na Wielkim Zderzaczu Hadronów (LHC), usytuowanym w laboratorium CERN w Szwajcarii. Jako jeden z dwóch detektorów przeznaczenia ogólnego nadaje się doskonale do obserwacji procesów Modelu Standardowego (SM), poszukiwania bozonu Higgsa, czy cząstek Supersymetrycznych, ale także do pomiarów z fizyki B oraz fizyki ciężkich jonów. Zapewnia on pokrycie niemal pełnego kąta bryłowego wokół punktu zderzenia i pozwala na szczegółowe i dokładne badania przypadków zderzeń proton - proton.

Niniejsza rozprawa doktorska prezentuje dwa aspekty analiz procesów Modelu Standardowego. Przedstawiony został pomiar przekroju czynnego dla procesu $W \to e\nu$, przeprowadzony na pierwszych 315 nb^{-1} danych zebranych przez eksperyment ATLAS. Zaprezentowano m. in. opis procedury wyboru przypadków sygnału, oszacowanie ilości przypadków tła, a także obliczenie niepewności systematycznej. Otrzymany wynik jest zgodny z opublikowanym przez Współpracę ATLAS oraz z przewidywaniami teoretycznymi. Zaprezentowano także studia nad mozliwością obserwacji procesu $W \to \tau\nu$ w eksperymencie ATLAS, oparte na analizie danych pochodzących z symulacji Monte Carlo i skupione na optymalizacji procedury wyboru przypadków sygnału, włączając selekcję na poziomie układu wyzwalania (*trigger*) oraz *offline*. Przygotowana analiza wskazywała na możliwośc obserwacji sygnału w eksperymencie ATLAS dla scałkowanej świetlności poniżej 100 pb^{-1}. Obserwacja ta, przygotowana przez współpracę ATLAS, została przeprowadzona w dużym zakresie w oparciu o analizę przygotowaną w ramach prezentowanej rozprawy doktorskiej.

Jako dodatkowy materiał praca prezentuje procedurę odwikływania (*unfolding*) widma pedu kosmicznych mionów w zalezności od ich ładunku. Prace nad opmiarem asymetrii ładunkowej mionów kosmicznych nie zostały przez współpracę ATLAS dokończone, ani opublikowane, gdyż otrzymane niepewności systematyczne nie pozwoliły na dokonanie znaczącego wkładu do wyników światowych.

Abstract

The ATLAS detector is the largest of the four experiments at the Large Hadron Collider (LHC) located at CERN, Switzerland. It is one of two so-called general-purpose detectors, not designed for observations of a particular branch of high-energy physics, but suitable for most expected measurements, including Standard Model (SM) tests, Higgs boson searches, Supersymmetry (SUSY) searches, but also aspects of B-physics and Heavy Ion collisions. It provides almost full solid-angle coverage around the beam crossing point and allows for detailed and precise studies of collision events.

This thesis presents two aspects of SM analyses. A description of a measurement of $W \to e\nu$ cross-section at $\sqrt{s} = 7$ TeV based on first 315 nb^{-1} is given with the description of signal events selection, background estimation and assessment of systematic uncertainties. The result, obtained as a part of this thesis is compatible both with the result published by the ATLAS Collaboration and with theoretical expectations. A study on the possibility of observing the $W \to \tau\nu$ process is also presented. This analysis is based on Monte Carlo simulated events and was focused on the optimization of signal extraction criteria, including the selection at trigger and offline level. It has been shown that for the integrated luminosity below 100 pb^{-1} signal observation should be feasible. This observation has been already made by the ATLAS experiment, to large extent following the analysis steps presented in this thesis.

As an additional material completed during the course of doctoral studies, an unfolding of cosmic muon charge-dependent momentum spectrum is presented. The analysis of cosmic muon charge ratio was however not completed by the Collaboration, because the systematic uncertainties did not allow for a significant contribution to world results.

Acknowledgements

I would like to thank, in the first place, my supervisor, prof. dr hab. Elżbieta Richter - Wąs for introducing me into the reality of the work in the ATLAS Collaboration and for her guidance and help in my studies on all the problems presented in this thesis.

I would also like to thank all the members of Cracow ATLAS group for creating a great atmosphere and for all the help I received from them in understanding the problems of physics and software of ATLAS.

I have benefited from collaborating with various ATLAS working groups, especially with the Tau Working Group and Standard Model Working Group, during my stays at CERN, but also while working in Cracow.

This work was partially supported by:

- Polish Government grant NN202 292038
- International Programmes no co-financed from foreign funds, 665/N-CERN-ATLAS/2010/0
- International Programmes no co-financed from foreign funds, 319/N-CERN/2008/09/0
- Polish Government grant NN202 006434
- Polish Government grant NN202 127937

Contents

Chapter 1

Introduction

Following the discovery of W and Z bosons in 1983 [1], the properties of these particles have been thoroughly measured in many experiments on hadron-hadron machines, including UA1 and UA2 at $Sp\bar{p}S$ collider at CERN [2] with $\sqrt{s}$ = 540 GeV and D0 [5] and CDF [4] at Tevatron accelerator at Fermilab, with $\sqrt{s} = 1.8$ TeV and $\sqrt{s} = 1.96$ TeV. Precise measurements of the Z-boson properties were obtained with the LEP accelerator at CERN [3] with electron-positron collisions and, recently, at Tevatron experiments for W-boson.

Theoretical calculations of the electroweak intermediate bosons production properties in hadron-hadron interactions have been conducted and provide a very precise information, acknowledging higher-order perturbative corrections [6]. They are sensitive to various properties of the Quantum Chromodynamics (QCD), namely Parton Density Functions (PDF) of a proton, so a precise measurement of their properties at the energy of the Large Hadron Collider (LHC) will provide new and very significant constraints on the Standard Model (SM) predictions in previously experimentally inaccessible energy region [7].

At the Large Hadron Collider (LHC) the W and Z bosons are produced abundantly, allowing for first observations of their appearance and measurements of their properties at very early stage of data-taking. First and already fundamental tests of SM predictions at such high energy scale can therefore be made even with quite small data sample, but the full projected dataset will provide a very detailed insight into electroweak bosons production properties in previously unexplored kinematic domain. Moreover, proton-proton collisions are significantly different from proton-antiproton interactions (conducted at Tevatron and $Sp\bar{p}S$) in terms of electroweak boson production (i.e. W charge asymmetry is expected at the LHC [7]). Apart from better understanding of SM, the W and Z-related measurements are also crucial in describing the SM background from New Physics (NP) processes. The di-lepton, or lepton+missing energy final states are predicted for many Beyond-Standard-Model (BSM) phenomena, such as the decays of supersymmetric (SUSY) particles [8]. The last but not least reason for the importance of SM measurements is the detector and software commissioning. Basic reconstruction and identification of objects, such as leptons or missing energy, can be studied with the decays of W and Z bosons. The energy scale at different levels can be also constrained with data-driven estimations, i.e. with high statistics of $Z \to ee$ decays.

Chapters 2 and 3 and Appendices A, B present the original work performed by the author, or pieces of work, to which he has made a significant contribution. Author's work consisted of:

- A contribution to the $W \to e\nu$ observation and cross-section measurement with first ATLAS data, published by the ATLAS Collaboration in [17] and in so-called supporting notes, internal to the ATLAS Collaboration: [21]-[25]. The author's analysis, parallel and compatible with the published one, containing full procedure of signal and background extraction, cross section determination and calculation of uncertainties is presented in Chapter 2.

- Full analysis chain for the $W \to \tau\nu$ process signal extraction for $\sqrt{s}$ = 14 TeV, including development of analysis code, finding optimal trigger menu and selection cuts with high-statistics Monte Carlo samples with both full and fast detector simulation, and an outlook on this analysis with $\sqrt{s} = 10$ TeV. This has been published in ATLAS notes: [19], [20] and is presented in Chapter 3. Author's contribution is also included in the chapter on τ-leptons of [27].

- The Krakow ATLAS group has been developing a tau reconstruction package, *tau1p3p* for many years. The author has taken part in validation and tests of the package and also in optimisation of trigger menu for $W \to \tau\nu$ channel studies presented in this thesis.

- Author has taken active part in the ATLAS detector operation, performing detector shifts in the Atlas Control Room at the Transition Radiation Tracker control desk, especially during the re-start of the LHC in November and December 2010 and during the 7 TeV 2010 run.

- Author has taken part in the cosmic muon charge asymmetry measurement with 2008 cosmic data. Author has developed a method to unfold detector effects on the transverse momentum spectra of incoming muons. This analysis was not published, as systematic uncertainties turned out to be too large to make a significant contribution with respect to earlier measurements. Part of this work is documented in Appendix B

- A significant amount of author's work has been dedicated to exploiting the maximum potential of local available computing clusters, the Tier-2 site at Cyfronet (see [28]), and a Tier3 cluster at the Institute of Nuclear Physics, including managing the software versions and data samples for analyses conducted by the whole Kraków ATLAS group.

The results presented in this dissertation have been previously published in ATLAS Communications or Physics notes ([19]) or providing material contributing to results published in [20], [17], [21]-[25] and [27]. The results were discussed during many meeting of the ATLAS Tau and e/gamma Working Groups. The author has presented the overall results measurement on W/Z production cross-sections by ATLAS Collaboration at Epiphany Conference 2011 [26].

This thesis is organized in the following way. In the first Chapter an introductionary overview on the electroweak boson physics is given, describing the motivation of the observation of W-bosons at the LHC. A brief description of the ATLAS experimental setup is also given in this Chapter. Chapter 2 reports the measurement of W-boson cross-section in electron-neutrino channel with first 315 nb^{-1} of data collected by ATLAS in spring and summer 2010. Description of analysis strategy and expected detector performance, which would allow for $W \to \tau\nu$ observation in ATLAS is addressed in Chapter 3. Finally, the last Chapter provides a summary of presented work.

It has to be noted, that this thesis was prepared at a time of rapid changes of predicted LHC running conditions. The first approach to $W \to \tau\nu$ analysis was made, when the proton-proton center-of-mass energy was assumed to be 14 TeV, and Monte Carlo samples produced with this assumption were used for these studies. An update was made, when the predictions changed to 10 TeV and corresponding Monte Carlo was produced. These studies were made in preparation of "first data analysis", and the estimated integrated luminosity of first year of data-taking was 100 pb^{-1}, so the presented results are normalized to this number. Due to the delays in LHC start-up and its heavy damage in 2008, it turned out, that preparation of $W \to \tau\nu$ channel analysis on real data is beyond the timescale for this thesis. Therefore, the electron channel studies have been undertaken with the experimental data analysis, as the dataset size requirements for the first measurements were much lower than for the τ channel.

1.1 The Large Hadron Collider

The Large Hadron Collider [9] at CERN has been designed and constructed to study the nature of particles and their interactions at previously unavailable energy regime. Exploration of Standard Model phenomena at very high energies is being performed, together with ongoing searches for New Physics signatures, since December 2009. It is expected, that new constraints on the SM parameters will be found to help the understanding of its inconsistencies. Moreover, the LHC is thought of as a *discovery machine*. Many Beyond-Standard-Model theories are about to be deeply investigated, as the LHC is capable of providing the first information on the existence of extra-dimensions or supersymmetric partners of Standard Model particles. A better understanding of the universe is expected to be the key result of the LHC operation.

The accelerator is built in a circular tunnel of 27 km circumference, that has been previously occupied by the LEP collider. The designed energy of colliding proton beams of 7 TeV has not been reached in 2009 and 2010, when the machine was operating with 3.5 TeV of energy per beam. The proton-proton center-of-mass energy of $\sqrt{s} = 7$ TeV however is still the highest energy ever available for collider physics, with $\sqrt{s} = 1.96$ TeV being the previous limit achieved by the Tevatron accelerator at Fermilab, and already allows for performing measurements at previously inaccessible energy regions. In addition, the LHC may also accelerate and collide heavy ion beams, currently with 2.76 TeV per nucleon pair, achieved with lead ion beams in December 2010.

There are four large particle detectors at the LHC ring. Two of them, ATLAS (A Toroidal LHC ApparatuS, described in much more detail in Section 1.2) and CMS (Compact Muon Solenoid) cover almost full solid angle around the interaction point and are considered general-purpose detectors, suitable for most of desired measurements and discoveries of New Physics. Two other experimental set-ups have been constructed for dedicated studies, namely heavy ion collisions (ALICE - A Large Ion Collider Experiment) and heavy flavor physics (LHCb).

1.2 The ATLAS detector

The ATLAS detector [10] is the largest of the four experiments at Large Hadron Collider. Being the general-purpose detector, focused on complete measurement of events from various classes it has a cylindrical symmetry and provides almost full solid angle coverage. All detector subsystems are subdivided into three parts - the central one, called the barrel, and two symmetric end-caps. Figure 1.1 presents an overview of the system.

Various subdetectors are indicated, including the innermost part, the Inner Detector (ID), responsible for charged particle tracking, the calorimeters, that measure energies of produced particles, and muon system, used for detection and measurements of muons. Besides, a forward detectors, not shown on the Figure, are present, or under construction and development. The ATLAS detector is 44 m long and has a diameter of 25 m. Such size is a consequence of requirements on detector capabilities at very high collision energies, giving a good transverse momentum resolution with long lever arm and providing almost full containment of showers in thick calorimeter layers. Another key part of the ATLAS hardware system is the fast electronics for trigger and data acquisition, optimized for very high event rates expected and already observed at the LHC.

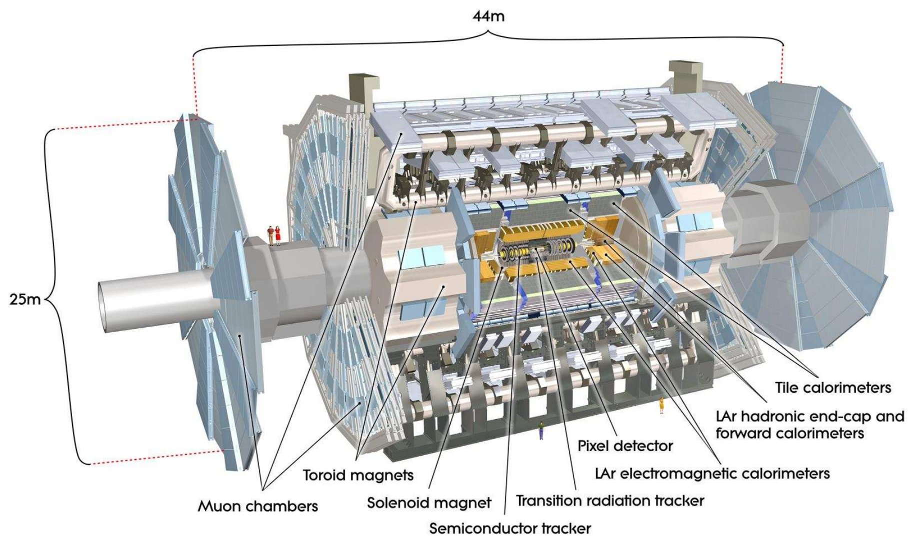

Figure 1.1: ATLAS detector overview

ATLAS provides extremely good coverage in pseudorapidity η[1]. Track reconstruction of charged particles is possible up to $|\eta| < 2.5$. Measurement of energies of particles and jets is possible up to $|\eta| < 3.2$ in both electromagnetic and hadronic parts. A forward hadron calorimeter provides pseudorapidity coverage within $3.1 < |\eta| < 4.9$. Forward detectors can reach even farther with $5.4 < |\eta| < 6.1$ for the luminosity detector LUCID and $|\eta| > 8.3$ for the zero-degree calorimeter (ZDC). Muon detection is possible up to $|\eta| < 2.7$.

An overview of the main subsystems is given in the following Subsections.

1.2.1 Inner Detector

The subdetector placed closest to the interaction point is the Inner Detector. Immersed in $B = 2$T magnetic field provides tracking and momentum measurement for charged particles over 5 units of rapidity in the central region. It consists of three parts presented in Fig. 1.2.

The innermost one is the most precise Pixel detector, with three concentric layers, parallel to the beam, in the barrel region and three disks, perpendicular to the beam axis, in each endcap, giving typically 3 hits per charged particle track traversing the detector. The layer closest to the beampipe is often referred to as the B-layer and the granularity of silicon pixel sensors is finest here. The pixel detector has over 80M of readout channels

[1] In the ATLAS coordinate system the z-axis is parallel to the beam-line and points towards the anti-clockwise direction of the beam in LHC ring. The x-axis points towards the ring center, setting the $\phi = 0$ value of the azimuthal angle and the y-axis points upwards. The transverse quantities (like transverse momentum p_T or missing transverse energy E_T^{Miss}) are defined in the $x - y$ plane. The polar angle θ is measured starting from the positive direction of z-axis and pseudorapidity η is defined as $\eta = -ln tan\theta/2$. The distance in $\eta - \phi$ is defined as $\Delta R = \sqrt{\Delta\eta^2 + \Delta\phi^2}$. A slight ambiguity occurs, as the R as a coordinate is defined as a transverse distance from the z-axis, $R = \sqrt{x^2 + y^2}$, but this is mostly clear from the context.

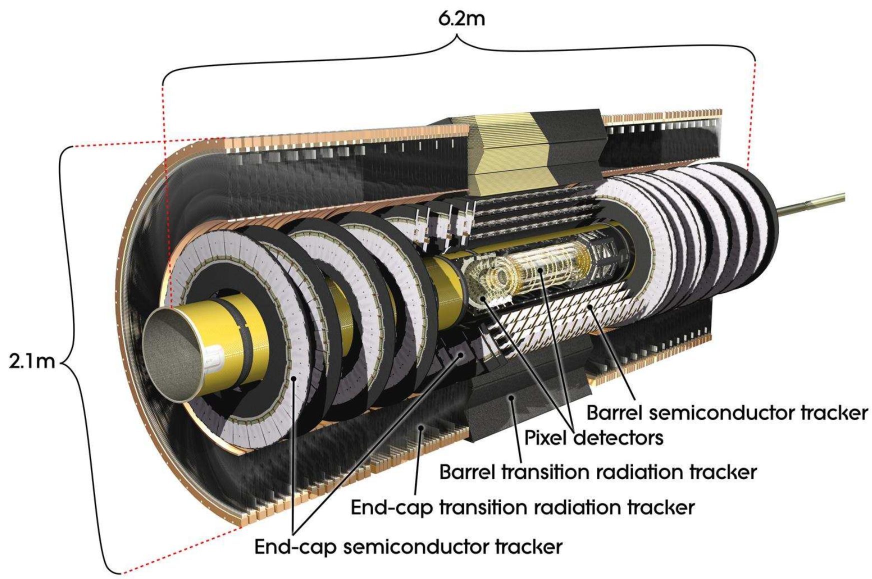

Figure 1.2: ATLAS Inner Detector overview

and the designed resolution of hit position in $R-\phi$ is 10 μm, whilst in the z (or R in endcaps) coordinate the resolution is 115 μm.

The Semi-Conductor Tracker (SCT) is another precision tracking detector located just behind the pixel detector looking from the interaction point. Built of silicon micro-strips provides 17 μm hit position resolution in $R-\phi$ and 580 μm in z (or R in endcaps). Its structure is similar to that of Pixels, with 4 cylindrical layers in barrel part and 9 disks in each endcap. Total number of readout channels is approximately 6 M.

Large number of hits per track is provided by the last of the tracking detectors, the Transition Radiation Tracker (TRT). Typically 36 spacepoints per track are expected up to $|\eta| < 2.0$. The TRT is built of straw tubes of 4 mm in diameter, providing only $R-\phi$ information with accuracy of 130μm in 350k of electronics channels. In addition, its construction allows for e/π discrimination using the differences between transition radiation induced signals from different particle types.

A combination of fine-precision silicon detectors with large number of spacepoints from the TRT provides good pattern-recognition and high precision in both $R-\phi$ and z coordinates. Momentum measurement precision is extended with the hits in the outer radius of the Transition Radiation Tracker.

1.2.2 Calorimetry

The calorimeter system is responsible for measurements of the energy of the particles (both charged and neutral) produced in collision, and is used for reconstructing jets and transverse missing energy of an event. A particle entering the calorimeter initiates a shower of particles of either electromagnetic or hadronic nature, which is then detected and its energy is measured in active layers. The ATLAS sampling calorimeter system consists of several parts that are presented in Fig. 1.3. It provides the coverage up to $|\eta| < 4.9$. Each

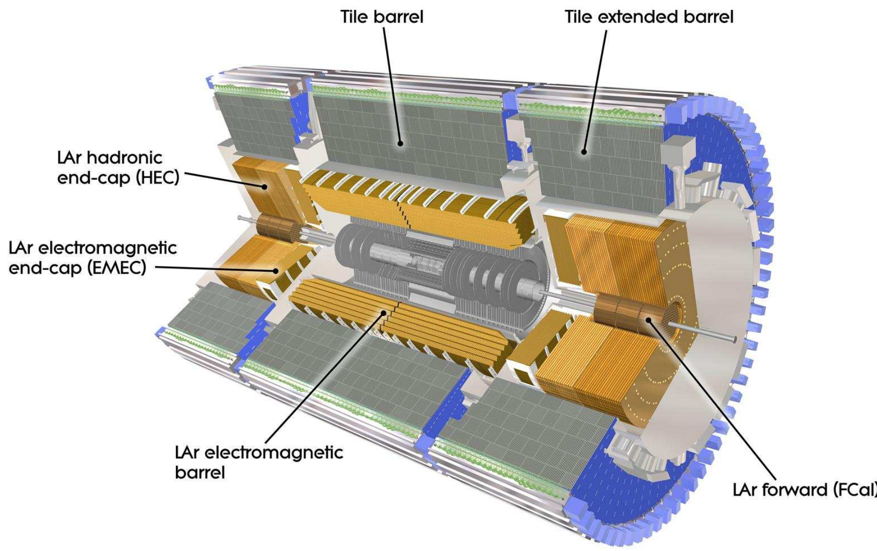

Figure 1.3: ATLAS Calorimeters overview

subsystem is segmented transversally and longitudinally into cells grouped in layers, with variable size, depending on the cell position, allowing for studies of shower shapes which greatly help in the process of identification of particles and jets.

The electromagnetic (EM) calorimeter, with Liquid Argon (LAr) as an active material and lead plates as an absorber, provides a coverage up to $|\eta| < 3.2$, with fine-granularity region matching the acceptance of the ID, $|\eta| < 2.5$, allowing for precise measurements of electrons and photons. Its total thickness is above $22X_0$ (X_0 is the radiation length) in barrel region and over $24X_0$ in endcaps.

Liquid Argon is also used as an active material in parts of hadronic calorimeter, Forward (FCal, with first layer optimized for electromagnetic measurements) and endcap (HEC). Also, plastic scintillating tiles with steel absorber are used in the Tile part located just on top of EM calorimeter. The approximate thickness of 9.7λ (λ is the interaction length) is sufficient for good resolution of measurements of high-energy jets and is sufficient to reduce punch-through effects to Muon Spectrometer well below the rate of genuine muon production.

1.2.3 Muon chambers

The Muon Spectrometer (MS) forms the outermost layer of sensors in ATLAS. It is designed to measure tracks of high-momentum muons with tracking chambers of various types within a toroidal magnetic field around the detector, averaging from 0.5T to 2T. In the barrel region the muon chambers are grouped in three cylindrical layers around the beam axis. In addition, three disks of detectors are present in each endcap.

Most of the coverage of the muon system is achieved with Monitoring Drift Tubes (MDT). Cathode Strip Chambers (CSC) provide the possibilities of precise muon track measurements in the forward regions, $2 < |\eta| < 2.7$. Resistive Plate Chambers (RPC) and

Thin-Gap Chambers (TGC) are used for triggering purposes and allow the measurement of second track coordinate, orthogonal to that measured by precision chambers.

1.2.4 Trigger system

The designed event rate at the LHC is 40 MHz. With the average event size of 1.3 MB it is neither possible nor useful to record and store all the events. A robust trigger system is therefore used. The ATLAS trigger system consists of three levels, namely L1, L2 and Event Filter. The first level uses only a limited part of the detector information and its decisions are taken by dedicated fast electronic systems, within the time of 2.5μs. It searches for high-momentum muons, electrons, hadronically-decaying τ's, jets and photons, exploiting the data from muon trigger chambers and reduced-granularity information from calorimeters. It reduces the event rate down to 75 kHz. Higher levels (High-Level Trigger, HLT) of trigger system are software-based and the information (already filtered at L1) is processed at dedicated computer farms to refine the information from L1-defined Regions of Interest (RoI) with full information from all detectors. Level-2, using simple and fast algorithms, reduces the event rate down to 3.5 kHz with decision time around 40 ms. Final refinement is made at Event Filter (EF), which reduces the rate down to 200 Hz. Algorithms used at this final selection step are based on the offline software and their average decision time is 4 s.

1.2.5 Data processing and ATLAS computing model

In comparison to earlier experiments, the amount of data recorded by the ATLAS detector, even after extensive trigger selection, is unprecedently large. Event rate of 200 Hz and its average size of 1.5 MB require an enormous computing power to be processed. A Grid infrastructure has therefore been developed to allow for distributed data management and computing.

Event Data Model

The data from collision events in ATLAS is strongly refined before being available for analysis. Many intermediate file formats for storing the information have been developed in the recent years. The Event Summary Data (ESD), with average event size of 500 kB, provides all the information needed for re-reconstruction of events, including calorimeter cells, hits from Inner Detector, together with already reconstructed tracks, clusters and candidates for electrons, muons and τ's. In a reduced form of so-called Distilled ESD (dESD) files, this information is available for performance studies in dedicated groups. Physics analysis was intended to be done on Analysis Object Data (AOD), with 100 kB of information per event on average, containing reduced information from the ESD, focused on particle candidates, jets and other physics objects, together with more detailed data on their identification. In the analysis of first data in 2009 and 2010 however the most convenient format, Derived Physics Data (DPD) was used in form of ROOT ntuples. Many different flavors of these data became available, containing only the information relevant to particular studies (i.e. so-called *egamma ntuples* were used for $W \to e\nu$ studies presented in this thesis). At the time of writing the strategy for further ATLAS analyses is evolving and it is not yet clear, which data format will be used as a baseline.

Grid infrastructure

As a matter of fact, it is not possible that a single computer-centre would handle the needs of ATLAS data analysis. Therefore, already at the R& D stage of LHC experiments, the Grid idea was developed. A large number of various-size computer centres have been connected with fast networks to form a common infrastructure, allowing for distributed data management and computing. They are grouped in hierarchical architecture, with CERN's Tier-0 being the central point for data distribution. Eleven Tier-1 sites, located in large computer centres all over the world, storing a proportional share of raw and reconstructed data and allowing for large-scale reprocessing. Data files are also distributed to around 140 of smaller, local Tier-2 sites, with Kraków's Cyfronet (CYF) being no exception. Specific analysis tasks can be conducted on these sites. Even smaller Tier-3 sites exist, providing helpful computer resources for individual studies, like the Tier-3 site of Institute of Nuclear Physics. The author has made a significant contribution to the development of this particular site, taking care of keeping the required ATLAS software up-to-date and managing the data samples for local analyses of the Kraków ATLAS group.

1.3 Standard Model physics at the LHC

1.3.1 Introduction

Following the idea of Glashow, Weinberg and Salam [11] in the 1960's, the Standard Model (SM) has been extensively tested for over forty years with experiments performed in a wide range of available energies, leading to discoveries of intermediate vector bosons, W and Z [1] and measurements of their properties, such as production cross-sections, masses, decay widths and branching fractions, with increasing precision ([2] - [5]). The Standard Model does, however, require the existence of currently unobserved particle, namely the Higgs boson [12]. One of the LHC's main goals is the discovery (or exclusion) of this boson and determination of its basic properties, which would give a crucial hint on Beyond the Standard Model (BSM) searches.

1.3.2 The Standard Model

The Standard Model [13] describes the elementary constituents of the universe and interactions between them. It is a gauge field theory, based on the symmetry group $SU(3)_C \times SU(2)_L \times U(1)_Y$, with the first term being responsible for Quantum Chromodynamics (the theory of strong interactions of color objects, namely quarks and gluons) and the other two describing the sector of electroweak forces.

Two kinds of fields are described by the SM. The *fermion* fields (with spin $s = 1/2$) describe the fundamental constituents - quarks and leptons, forming three generations (see Table 1.1). The *bosons* (with integer spin) mediate interactions between the fields. Four of them are available in the electroweak sector, with one related to the $U(1)_Y$ symmetry group, denoted as B and three corresponding to $SU(2)_L$ group generators, denoted W^i $(i = 1, 2, 3)$. The actual particles carrying the electroweak interactions are the combinations of these fields (symmetric and antisymmetric combination of first two W^i fields form $W^{\pm}$ bosons, whereas W^3 and B are combined into Z^0 boson and photon via θ_W Weinberg mixing angle). Similarly, eight gluon fields represent eight generators of the $SU(3)_C$ group.

Fundamental fermions		
generation	quarks (charge)	leptons (charge)
I	u (+2/3e)	$\nu_e(0)$
	d (−1/3e)	$e^-(-1e)$
II	c (+2/3e)	$\nu_\mu(0)$
	s (−1/3e)	$\mu^-(-1e)$
III	t (+2/3e)	$\nu_\tau(0)$
	b (−1/3e)	$\tau^-(-1e)$

Table 1.1: Elementary fermions and their properties.

It has been proven, that W and Z bosons are heavy, massive particles. However, introducing mass terms into the $SU(2)_L \times U(1)_Y$ lagrangian breaks its gauge invariance. Therefore, a mechanism of spontaneous symmetry breaking has been introduced by Higgs and others [12], being the minimal add-on to the model and conserving unitarity an renormalizability of the theory. Its simplest formulation requires an $SU(2)$ doublet of complex scalar fields. Its neutral term acquires a vacuum expectation value (VEV) leading to spontaneous breaking of $SU(2)_L \times U(1)_Y$ symmetry, which is reduced to $U(1)_Q$ electromagnetic symmetry. Four new degrees of freedom appear, out of which three are absorbed in W and Z longitudinal polarization states, and the remaining one corresponds to a scalar particle, the famous Higgs boson (H). It is the only missing piece of the Standard Model, that has not yet been observed. Fermions acquire their masses with Yukawa-type interactions with the Higgs field.

Many of the Standard Model parameters are not derived from any theory, but have to be measured experimentally. A finite number of these parameters are needed to constraint the model. Three quantities serve as a typical input to the Standard Model, namely ([14]):

- The fine-structure constant, α_s, which is the coupling constant of electromagnetic interactions. It changes with energy scale of the process, and its value at 0-energy scale is $\alpha_s = 1/137.035999084(51)$, currently known with the best precision from $e^\pm$ anomalous magnetic moment observations.

- Fermi constant G_F which determines the strength of charged current. It is measured with muon lifetime and the result is $G_F = 1.166364(5) \times 10^{-5}$ GeV^{-2}. It is obtained with muon-lifetime measurements.

- Mass of Z-boson, $M_Z = 91.1876 \pm 0.0021$ known from LEP lineshape scans.

These three parameters correspond to three degrees of freedom in the gauge sector, two coupling constants of the $SU(2)_L \times U(1)_Y$ group and one vacuum-expectation-value of the Higgs field. With this input, every SM process can be calculated at tree-level (when hadron flavor mixing processes are included, one needs also the parameters of Cabibbo-Kobayashi-Maskawa matrix). For higher-order calculations at loop-level, another parameters are needed:

- fermion masses, contributing to photon self-energy, as well, as weak-boson self energy and vertex corrections, with the most significant contribution from the top-quark mass;

- the mass of the Higgs boson m_H, with small, logarithmic effect;
- strong coupling constant at Z-mass energy scale, $\alpha_S(M_Z^2)$.

The precision of estimation of the input parameters (and not missing orders in radiative corrections) is the main limitation on the precision of predictions obtained within the SM framework. Mixing the input from experimental measurements and the best-known theoretical predictions helps in obtaining constraints for the least-known SM parameters, such as the Higgs boson mass.

1.3.3 Electroweak bosons at the LHC

The W and Z bosons are abundantly produced at hadron-hadron colliders, with no exception in case of the LHC. The main processes, contributing to weak boson production in proton-proton collisions are shown in Fig. 1.4, with quark-antiquark annihillation being the first-order term.

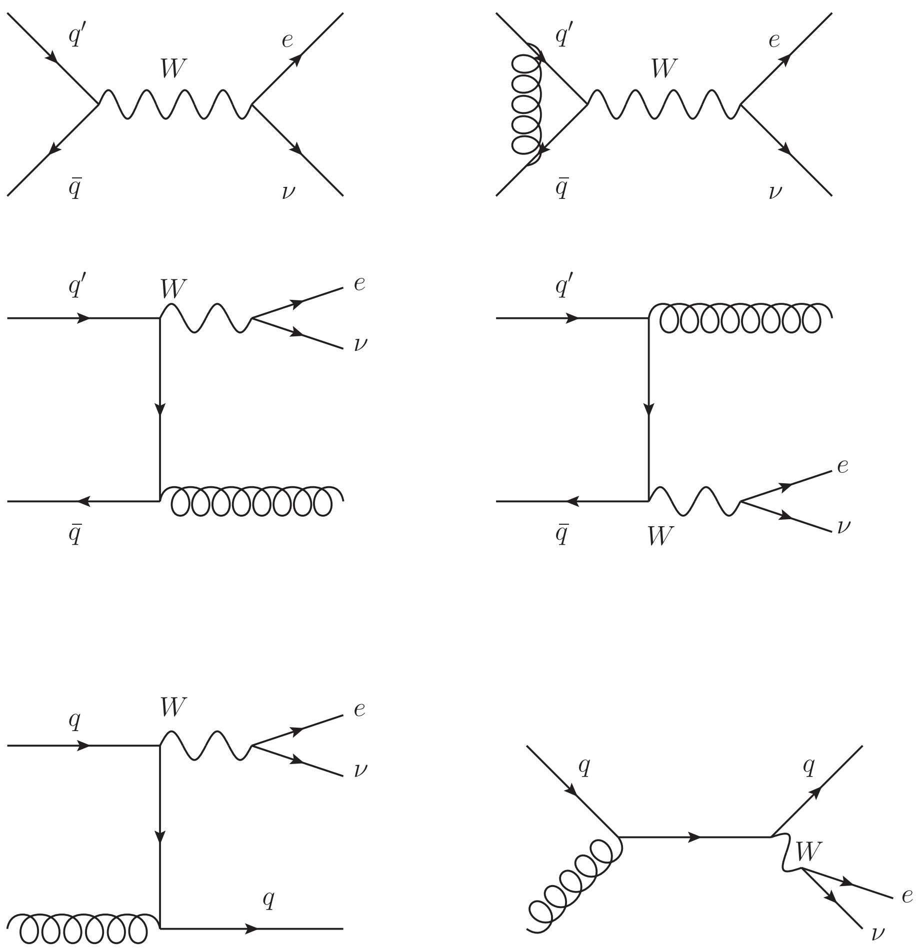

Figure 1.4: The W boson production processes. The Feynman diagram for the Born term is presented in the upper-left plot, with examples of higher-leading order diagrams on other plots .

The cross-section for inclusive production of vector intermediate bosons in proton-proton interactions can be written in the following way [15]:

$$\sigma_{W(Z)} = \sum_{ab} \sigma_{ab \to W(Z)} \otimes PDF(x_a, x_b, Q^2). \tag{1.1}$$

It is a convolution of $ab \to W(Z)$ parton-parton cross-section with Parton Distribution Functions (PDF) of partons a and b inside two incoming protons. It is then summed over all partons. Quantities x_a and x_b represent momentum fraction carried by parton a and b respectively. The PDF's cannot be calculated in the perturbative QCD and are extracted from global fit to experimental data, mainly from Deep-inelastic Scattering (DIS) experiments [7]. The hard-process cross-section ($\sigma_{ab \to W(Z)}$) is, however, easily computable. On the other hand, the cross-section is an observable and can be directly measured with the rate of $W(Z)$ events occuring in collisions. It can be expressed as follows:

$$\sigma_{W(Z)} \times BR(W(Z) \to \ell\nu(\ell\ell)) = \frac{N_{obs} - N_{bkg}}{\alpha_{W(Z)} \epsilon_{W(Z)} L_{int}}. \tag{1.2}$$

In the above N_{obs} denotes number of events passing final selection. Number of background events N_{bkg} (estimated during the data analysis) must be then subtracted. In the denominator there are two factors, that are used to "correct" the number of observed signal events to get the number of actually produced ones, the $\alpha_{W(Z)}$ states for detector and selection procedure acceptance, and describes the fraction of events that actually have the chance to be selected. The $\epsilon_{W(Z)}$ denotes the efficiency of selection of events provided they are contained within acceptance. The integrated luminosity of the analyzed data sample is denoted L_{int}.

Comparing equations 1.1 and 1.2 one can solve them to extract the PDF's [15]. The LHC will provide the information on Parton Distribution Functions in (x, Q^2) regions, that were previously not accessible in low-Q^2 experiments (HERA and fixed-target). For the Q^2 of the order of W-mass (say $Q^2 = 10^4$ GeV^2) and rapidity coverage $|y| < 2.5$ with the nominal collision energy $\sqrt{s} = 14$ TeV the x range is within 10^{-4} and 10^{-1}, see Fig. 1.5. With the current theoretical knowledge of the W production cross-section, computed at NNLO [6], a precise measurement is sensitive to higher-order QCD corrections at this energy regime. In addition, the PDF uncertainty is the main theoretical uncertainty in the W-mass measurement at the LHC [16].

1.3.4 ATLAS program for W/Z boson measurements

The ATLAS program for early physics involves extensive studies on electroweak boson properties, which are crucial in understanding the Standard Model at sufficiently precise level. It is absolutely fundamental to confirm good understanding of SM processes before moving on to New Physics searches. The ATLAS program includes measurements of:

- inclusive W and Z production cross-section;
- W charge asymmetry;
- differential cross-section of electroweak bosons production, with respect to transverse momentum and pseudorapidity;
- W-boson mass and decay width.

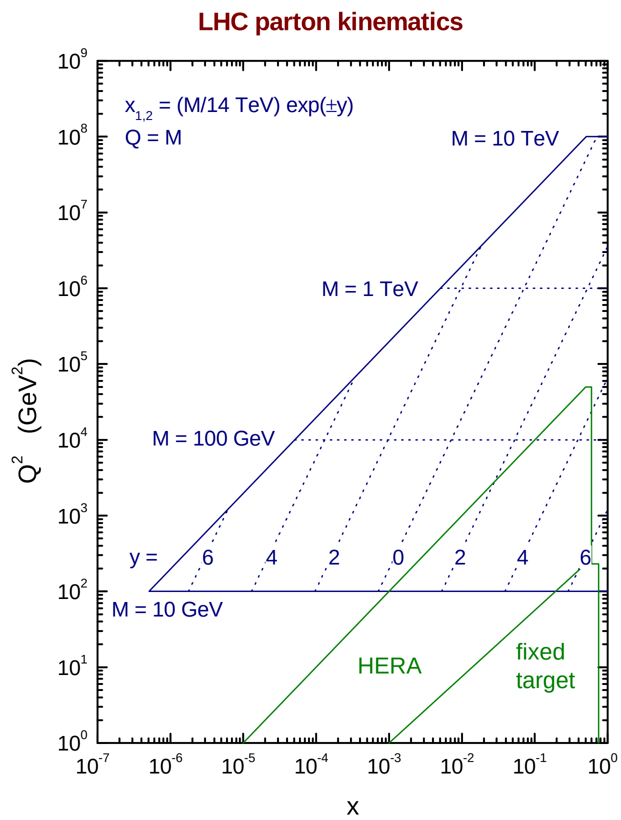

Figure 1.5: Representation of (x, Q^2) coverage of Large Hadron Collider experiments (ATLAS and CMS). The coverage of HERA and fixed-target detectors is shown for comparison. [7]

The W/Z cross-section measurement has been performed by the ATLAS Collaboration already, with low statistics of data, being the first possible and fundamental measurement in electroweak sector with the ATLAS detector [17]. The charge asymmetry measurement was about to be published by the Collaboration at the time of writing and there was an ongoing work on differential cross-section studies.

First published measurements have been performed with electron and muon channels only. The τ channel requires much more integrated luminosity, as the process of signal extraction is much harder and less efficient, due to the difficulties in suppressing the QCD background. As stated in Chapter 3, for a similar number of observed signal events, as in the electron channel, the required integrated luminosity is 30 times larger. Therefore, the ATLAS Collaboration has not yet (by the time of writing) published cross-section estimations based on $W \to \tau\nu$ process, only an observation has been conducted and documented in [18].

The analyses of the two aforementioned channels differ significantly, due to diverse properties of the final states. In the τ channel the lepton is not observed directly, but only after a τ hadronic decay. This implies the existence of another neutrino in the event, resulting in smoother E_T^{Miss} spectrum, with average value larger than in electron channel. This allows for more restrictive E_T^{Miss} -based selection, which is crucial for background discrimination. The QCD dijet background is much more dominant for $W \to \tau\nu$, because hadronically decaying τ leptons produce genuine jets of π mesons. An efficient signal online and offline selection is therefore much more difficult here, as the signal signature is much less distinctive, than in electron channel. It is therefore impossible to achieve signal selection efficiency at the same level, as in electron channel whilst keeping the background rate sufficiently low. Therefore in this thesis no data-based measurements nor observations of $W \to \tau\nu$ channel are presented, as it was beyond the available timescale to obtain the results in τ-channel with data.

Chapter 2

Measurement of $W \to e\nu$ cross-section with first 315 nb^{-1} of ATLAS data

2.1 Introduction

The process of W boson production is one of the first electroweak physics processes possible to be observed and measured at the LHC, as they are expected to be produced abundantly, even at 7 TeV center-of-mass energy. Further measurements with far larger integrated luminosity and dataset size will increase the possibility of detailed studies of W production properties at high energy scale. Such results will be important as they will provide new information on parton distribution functions (PDFs), and on perturbative QCD in general. This is due to the fact, that the inclusive W production cross-section is sensitive to higher-order QCD corrections. Theoretical calculations have been performed down to next-to-next-to-leading order (NNLO) terms [6].

Due to experimental constraints, first W bosons in ATLAS have been observed in $W \to e\nu$ and $W \to \mu\nu$ decays. The $W \to \tau\nu$, although produced at the same rates (due to lepton universality) requires more integrated luminosity to extract signal from QCD background (see Chapter 3). This Chapter covers the details of first observation and cross-section measurement of W in the electron channel with 315 nb^{-1} of integrated luminosity. It is organised as follows. Section 2.2 lists the Data and Monte Carlo samples used in this analysis, Section 2.3 describes briefly the process of reconstruction and identification of electron candidates and of transverse missing energy (E_T^{Miss}), whereas in Section 2.4 a selection flow of $W \to e\nu$ candidates is discussed. In Section 2.5 calculation of acceptance and efficiency for signal selection is described and in Section 2.6 the systematic uncertainties of selection efficiencies are assessed. Section 2.7 presents the extraction of the number of background events from the final sample and Section 2.8 shows the results of final selection and calculation of $W \to e\nu$ cross-section.

Results described in this Chapter present author's own work (unless cited differently) and are in some details different than those published by the ATLAS Collaboration in [17].

It has to be noted, that the published result ([17]) is the first $W \to e\nu$ cross-section measurement at such high energies. Being one of the first ATLAS physics analyses with collision data, it is kept rather conservative in terms of uncertainty estimations, and therefore may not seem as complicated, as further, planned studies in this sector, i.e. differential cross-section measurements. At this stage of data-taking it was not justified to try to further reduce systematic uncertainties with more refined methods of signal extraction, as the statistical uncertainty would dominate the measurement. It is however expected, that for studies with larger dataset (i.e. the full 2010 set of around 36 pb^{-1}) the systematic uncertainty will be much lower, due to much better understanding of detector properties and reconstruction performance, obtained with fully data-driven methods, which were not applicable here because of small statistics available. More refined methods of analysis will be then applied with performance figures measured directly from data. Also, it is expected, that the uncertainty on luminosity determination will become significantly smaller.

2.2 Data and Monte Carlo samples

For the current analysis a data sample collected between March and August 2010 has been used. Estimated integrated luminosity of the sample is 315 nb^{-1} with uncertainty of 11% [29]. Events for electron channel analysis were selected using calorimeter-based Level-1 trigger, `L1_EM10` . No higher-level triggers were used in this selection. The trigger algorithm bases on electromagnetic deposits in LAr calorimeter within $|\eta| < 2.5$ and looks for a cluster of calorimeter towers with energy above approximately 10 GeV. A total of 6.5×10^6 events are selected for further analysis.

In order to make comparisons with theoretical predictions, as well as to calculate the background rates and cross-section, a number of Monte Carlo samples were produced:

- $W \to e\nu$ signal sample;
- $W \to \tau\nu$ - this process may contribute to electron channel mostly via $\tau \to e\nu$ decay and is considered as a background;
- $Z \to ee$ - if one of the electrons is not reconstructed (i.e. outside of detector acceptance or lost due to reconstruction inefficiency) this process may generate a significant missing transverse energy accompanying a single reconstructed electon;
- $Z \to \tau\tau$ may also yield a small contribution to the $W \to e\nu$ final state;
- production of the *top*-quark pairs forms an additional background to W analysis;
- jet production in QCD processes is a very significant part of background processes. It contains electrons coming from semi-leptonic quark decays, conversions, and misidentified hadrons. Its huge cross-section (see Table 2.1) makes this set of background processes the most difficult to cope with in the current analysis.

Table 2.1 lists the Monte Carlo samples used. All these samples were generated at 7 TeV center-of-mass energy and simulated with the `GEANT4`[30] ATLAS detector simulation[31]. Further steps of reconstruction and event selection are the same as for the data sample. Table 2.1 presents also the cross-sections to which the samples were normalized. Except the QCD dijets, all the samples were normalized to cross-sections, calculated including higher-order corrections, and the cross-section for dijet production is given in leading order (LO). A large expected uncertainty (of the order of 200%) of the predicted cross-section and selection acceptance requires, that the overall normalization of QCD background will have to be performed with data-driven methods. To account for expected pileup in data, the Monte Carlo samples were produced with two primary interactions on average, and then reweighted to match the primary vertex multiplicity observed in data.

Process	Generator	Order	Cross-section
$W \to e\nu$	`PYTHIA`[32]	NNLO	10.46 ± 0.52 nb
$W \to \tau\nu$	`PYTHIA`	NNLO	10.46 ± 0.52 nb
$W \to \tau\nu \ \to \ell\nu\nu\nu$	`PYTHIA`	NNLO	3.68 ± 0.18 nb
$Z \to \tau\tau$	`PYTHIA`	NNLO	0.99 ± 0.05 nb
$t\bar{t}$	`MC@NLO`[33], `POWHEG`	NLO+NNLL	0.16 ± 0.01 nb
Dijet, $\hat{p}_T > 15$ GeV	`PYTHIA`	LO	97707 nb

Table 2.1: Details on the Monte Carlo samples used. All cross-sections are at next-to-next-to-leading order, except the QCD dijets (see text). The production of dijets contained a requirement of the transverse momentum of partons involved in hard-scattering, to be $\hat{p}_T > 15$ GeV. The Z and W cross-sections include the branching fraction to the specified lepton.

2.3 Electron and missing transverse energy reconstruction

2.3.1 Electrons

The electron reconstruction and identification procedure, that has been used in this work is the standard ATLAS procedure, described in [34]. Electron candidates are seeded with an electromagnetic cluster with transverse energy above 2.5 GeV in the second layer of electromagnetic calorimeter. Then the algorithm looks for a reconstructed track, that, after extrapolation, matches the seed cluster. The search is performed within a window of $\Delta\eta \times \Delta\phi = 0.05 \times 0.1$. The closest matching track to the cluster's barycenter, with $p_T > 0.5$ GeV is then considered to be the electron track. Final candidates have calorimeter clusters of the size of $\Delta\eta\times\Delta\phi = 0.075\times0.175$ in the barrel part and $\Delta\eta\times\Delta\phi = 0.125\times0.125$ in endcaps. Transverse energy of such candidates is the energy of electromagnetic cluster.

After reconstruction, the candidates are examined by the identification algorithms. Identification criteria have been optimised through the phase-space divided into 11 bins in η and 10 bins in E_T. Three reference set of cuts have been prepared, based on the expected rejection factors of the QCD background. However, with increasing rejection power the efficiency of electron identification decreases.

- *Loose* identification criteria provide high efficiency and uniformity of electron identification, but have poor QCD rejection power. This set of cuts exploits the shower shape variables from the second layer of calorimeter (lateral shower containment and shower width) and also the leakage of energy into hadronic calorimeter.

- *Medium* selection cuts make use of first-layer energy deposits and track quality variables in addition to requirements defined for the *loose* selection. The shower width in the first layer, as well as the ratio of energy difference between two largest deposits to their sum is taken into account. Track-quality criteria are based on the number of hits in Pixels and SCT and the transverse impact parameter of a track. Moreover - a $\Delta\eta$ track-cluster matching is performed. Such set of criteria provide much better background rejection.

- *Tight* identification adds further cuts on track-based variables strongly increasing the rejection of fake electrons from QCD as well as conversions. There are cuts placed on the ratio of cluster energy and track momentum, the number of hits in TRT, the ratio of the number TRT high threshold hits to the total number of TRT hits. At least one hit in the pixel detector first layer is required to remove electrons from conversions.

More details on electron identification criteria can be found in Appendix C.

The performance of medium and tight identification will be determined using $Z \to ee$ process from data, using tag and probe method. However, currently due to the lack of statistics, numbers extracted from Monte Carlo ($W \to e\nu$ and $Z \to ee$) samples are used. The efficiency of medium identification is found to be 94.3% within kinematic and geometrical acceptance (transverse energy above 20 GeV and $|\eta| < 2.47$ with the exclusion of barrel-endcap transition region $1.37 < |\eta| < 1.52$). The number is given with respect to reconstruction efficiency, which is estimated to be 85.8%. Similarly, for the tight cuts the efficiency is found to be 74.9%. Rejection factor for fake electrons has been found using the dijet Monte Carlo sample and is, on average, respectively, 5700 and 77000.

During the course of data taking it became clear, that some regions of the LAr calorimeter are affected by significant hardware problems and, in addition, number of such regions may change in time. Hence, an offline tool was developed by members of the E/gamma Working Group. It finds and removes electrons that fall in the affected calorimeter regions. This cut is known as the *dead OTx removal*. Problems in the mentioned regions may come from various sources, including major high voltage problems, bad cells (producing no signal or a very high constant noise) or dead optical readout lines. The dead OTx removal causes a drop in electron reconstruction efficiency, which has already been accounted for in the numbers discussed in the previous paragraph.

2.3.2 Missing transverse energy

The missing transverse energy, E_T^{Miss} , is calculated basing on information from calorimeter cells from inside topological clusters. Such clusters are built around a seed cell, which has an energy deposit $E > 4\sigma$ where σ is the Gaussian width of cell energy spectrum collected in randomly-triggered events and quantifies the cell noise level. In next steps the neighbouring cells with energy $E > 2\sigma$ are added, and in the final step, all surrounding cells are added to the sum [36]. In this analysis the transverse missing energy is calculated at electromagnetic scale (under assumption, that all processes here are of an electromagnetic nature). A correction weights are applied if the cluster is classified as hadronic. Another corrections are applied afterwards. The out-of-cluster corrections are used to account for low-energetic tails of hadronic showers that are lost during clusterization process. The losses of energy in dead material are also corrected for in this procedure [37].

The x and y components of the E_T^{Miss} , the $E_{x,y}^{Miss}$, are calculated using corresponding components of energies of cells i, the $E_{x,y}^i$, contained in the aforementioned topological clusters:

$$E_{x,y}^{Miss} = -\sum_i E_{x,y}^i. \tag{2.1}$$

The transverse missing energy is then obtained with the following formula:

$$E_T^{Miss} = \sqrt{(E_x^{Miss})^2 + (E_y^{Miss})^2} \tag{2.2}$$

2.4 $W \to e\nu$ event selection

The event selection procedure that has been applied in the current work consists of several steps. At first, good collision events are selected. Apart from trigger requirement, already described in Section 2.2, additional requirements are applied. An event should have at least one reconstructed primary vertex, with at least 3 associated tracks. In addition, a so-called *MET-cleaning* (sometimes referred to as *jet-cleaning*) is performed. It removes a small fraction of events (0.01% in Minimum-Bias, 0.004% in $W \to e\nu$ and 0.01% in dijets), that fall into one of the three categories listed below:

- Mis-reconstructed jets may appear due to huge noise-bursts in the hadronic endcap calorimeter (`HEC`). Such fake jets have usually a high energy deposit in `HEC` in very few cells (i.e. number of cells containing 90% of jet energy is not larger than 5). Energy fraction of a jet deposited in `HEC` is above 80%.

- Another type of fake jets may appear due to noise bursts in electromagnetic calorimeter. They have a very high energy fraction deposited in EM part, above 95%, and the pulse shape of such noise-bursts is far from what is expected as a reference. A quality variable describing the fraction of jet energy coming from noisy cells is denoted f_{QLar} and the event is removed if $f_{QLar} > 0.8$.

- Energy depositions in LAr calorimeter that are not timed-in with the actual event may come from various sources, including cosmic rays. These effects may bias E_T^{Miss} measurements and hence, they are removed. A criterion is set to $|t_{jet}| > 50$ ns.

As mentioned in Section 2.2, the available Monte Carlo programs for QCD dijets generation used the cross-section calculated at leading order (LO), which means that there is a huge uncertainty of that value. Therefore, at loose selection level, a normalization factor was obtained, by comparing the electron E_T distributions between data and Monte Carlo, see Fig. 2.1. The factor was found to be 0.4167 and is used only for normalization of plots, for cross-section studies it will be extracted with data-driven methods. The next

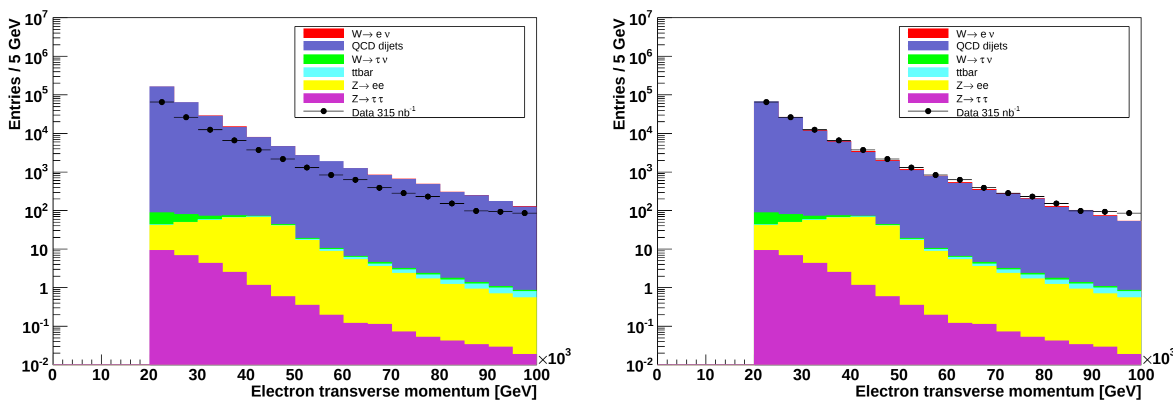

Figure 2.1: Left: Transverse energy of electron candidates after pre-selection, without QCD scaling factor applied. Right: Transverse energy of electron candidates after pre-selection, with QCD background scaled down by 0.4167 (see text).

step of the event selection is a so-called pre-selection of a loose electron sample. Electron candidates have to be reconstructed by either *egamma*-only algorithm (the basic ATLAS electron-photon reconstruction package) or by both *egamma* and *softe* algorithms (the latter is optimised to find soft electrons, i.e. low-energy ones). Such candidates must not fall into a barrel-endcap transition region in electromagnetic calorimeter, so the region of $1.37 < |\eta| < 1.52$ is excluded. Also, the candidates must be contained within the inner detector acceptance, $|\eta| < 2.47$. Dead OTx removal is applied at this stage (see Sec. 2.3). Finally, only candidates with loose identification requirements fulfilled are accepted. This sample will be used to find the QCD cross-section normalization factor, as at this selection step, it is dominated by QCD events. Figure 2.2 shows the distributions of electron candidate transverse momentum (left) and missing transverse energy (right).

Final selection step will provide a sample of $W \to e\nu$ candidates. An electron fulfilling tight identification requirements needs to be present in the event. Additionally, a transverse

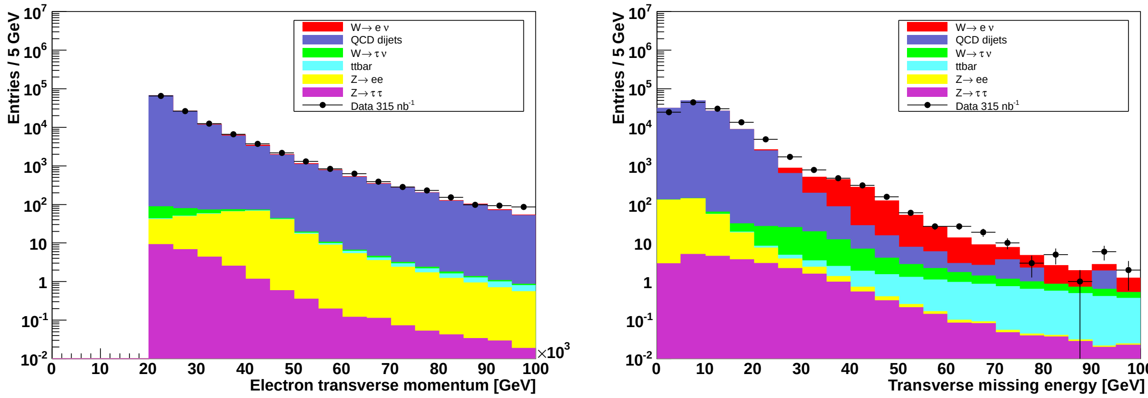

Figure 2.2: Left: Transverse momentum of electron candidates after pre-selection. Right: Missing transverse energy after pre-selection. In both plots data is shown with points with errors and Monte Carlo samples are plotted as filled histograms.

missing energy should be at least 25 GeV, and a transverse mass of electron-E_T^{Miss} pair needs to be above 40 GeV. The transverse mass is defined as follows:

$$m_T = \sqrt{2p_T^e p_T^\nu (1 - cos(\phi^e - \phi^\nu))}. \tag{2.3}$$

In the formula above the $\phi^{e,\nu}$ denotes the azimuthal angle of electron or neutrino, whereas $p_T^{e,\nu}$ stands for electron (neutrino) transverse momentum. Neutrino variables are obtained from transverse missing energy measurement.

Additionally, events with second electron passing medium identification cuts are removed, as they come from $Z \to ee$ process. Figure 2.3 shows the distributions of transverse missing energy (left) and transverse mass of $W \to e\nu$ candidates (right) after tight selection, but before E_T^{Miss} and m_T cuts. Figure 2.4 shows the distribution of transverse mass of a $W \to e\nu$ candidate with all cuts except the m_T itself. Figure 2.5 shows transverse energy distribution for electron candidates (left) and transverse momentum of the W boson (right) after final selection. QCD correction factor (see Sec. **??**) is applied in all plots listed above.

A total of 1061 events were selected from data following the procedure described above. Table 2.2 summarizes numbers of events remaining after each major selection step.

Selection	Events remaining
Trigger	6.5×10^6
Pre-selection	1.2×10^5
Tight electron identification	3857
$E_T^{Miss} > 25$ GeV	1107
$m_T > 40$ GeV	1061

Table 2.2: Numbers of events remaining after certain selection steps.

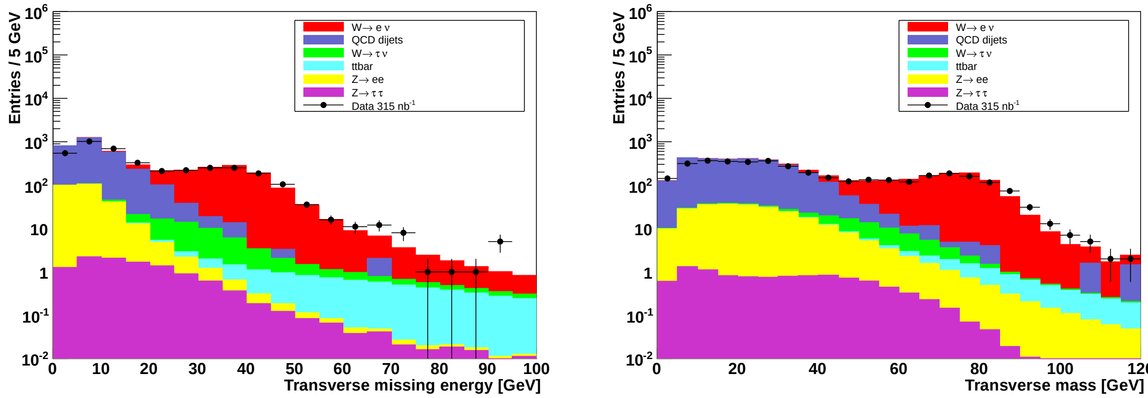

Figure 2.3: Left: Missing transverse energy of $W \to e\nu$ candidate events after tight electron selection. Right: Transverse mass of electron-E_T^{Miss} system after tight electron selection, without E_T^{Miss} requirement.

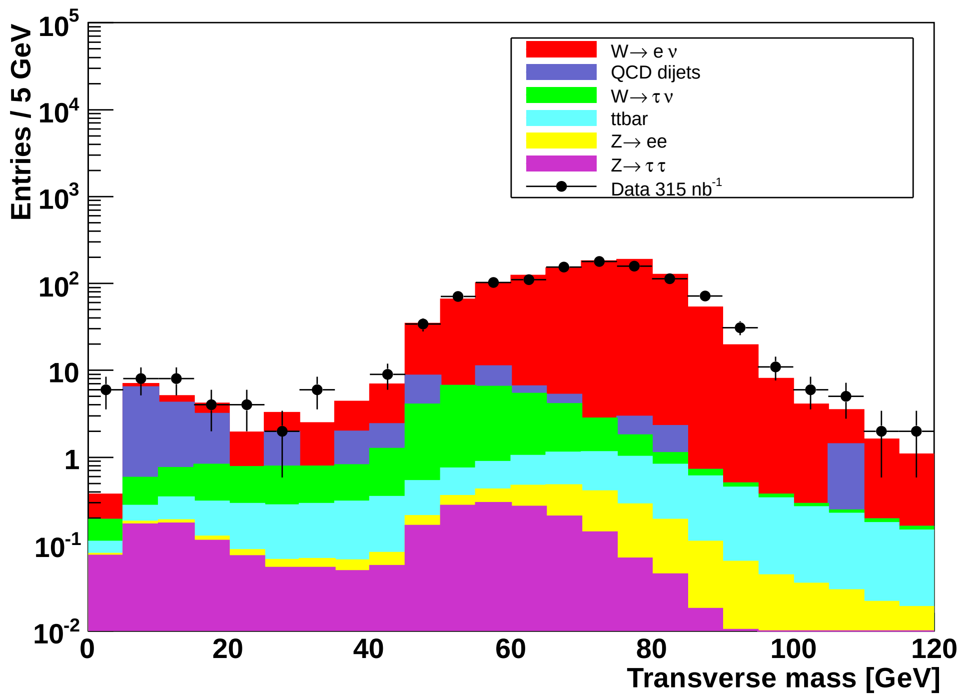

Figure 2.4: Missing transverse energy of $W \to e\nu$ candidate events after tight electron and $E_T^{Miss} > 25$ GeV selection.

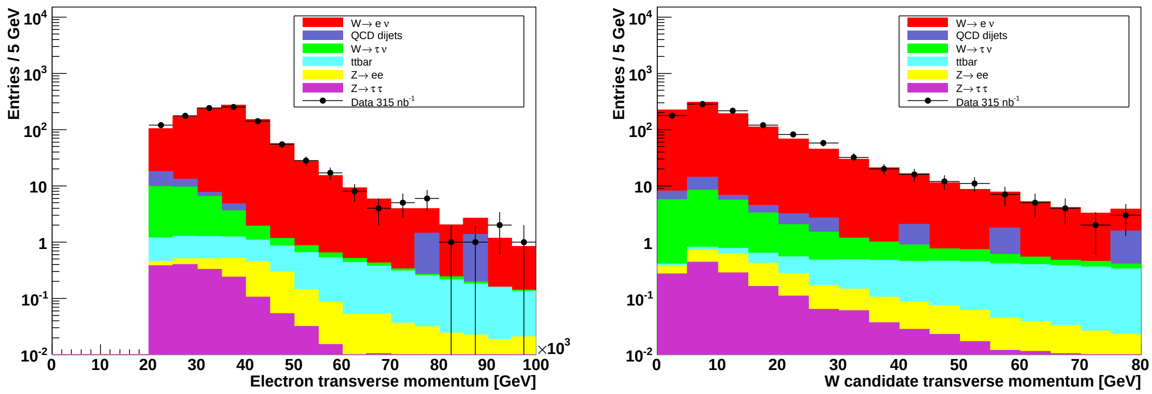

Figure 2.5: Left: Transverse energy of electron candidates after final selection. Right: Transverse momentum of W-boson candidate after final selection.

2.5 Signal acceptance and efficiency

The cross-section measurement, as described in Section 2.8, requires a knowledge of signal acceptance α and selection efficiency ϵ.

- Acceptance α can only be calculated on Monte Carlo samples. It represents a ratio of events passing geometrical and kinematical cuts at generator level to the total number of generated events. These cuts are applied on true electron transverse momentum, its pseudorapidity, the transverse momentum of a neutrino and transverse mass of the $e - \nu$ system.

- Selection efficiency ϵ contains all detector-related inefficiencies and the effect of QED final-state-radiation (FSR). For analysis presented here it is also based on Monte Carlo calculations. It can be factorized as follows:

$$\epsilon = \epsilon_{event} \times \epsilon_{reco} \times \epsilon_{id} \times \epsilon_{trigger}. \tag{2.4}$$

  In the equation above, four factors appear, that can be described as follows:

  - ϵ_{event} is the efficiency of collision event selection (requirements such as primary vertex cut or MET-cleaning).
  - ϵ_{reco} denotes the correction factor related to reconstruction and contains the following effects:
    * geometrical and kinematical cuts applied at reconstructed quantities (not like in α calculation, where the cuts are applied on true quantities);
    * reconstruction inefficiencies, namely - the probability that the electromagnetic cluster passes dead OTx removal and is loosely matched to a track, provided it comes from a true electron;
    * QED final state radiation photons;
    * all bin-migrations and combinatorics.

This factor can, in principle, be higher than 1, as cutting on generator-level variables may remove more events, than cutting on reconstructed quantities. This is particularly true for E_T^{Miss} cut.

- ϵ_{id} is the efficiency of identification criteria calculated with respect to reconstructed objects (i.e. the denominator is the number of reconstructed candidates matched to true electrons in MC and the numerator is the number of candidates not only reconstructed and matched to MC but also passing the considered identification criteria).
- ϵ_{trig} is the efficiency of trigger calculated with respect to all candidates passing final selection cuts.

All the quantities described above are currently estimated using Monte Carlo samples. Further analyses will certainly aim for more data-driven determinations of the efficiency factors. All these factors can be replaced by data-driven estimations one-by-one, when the sufficient statistics becomes available.

Final acceptance and efficiency corrections are given in Table 2.3. The errors represent systematic uncertainties, which are discussed in Section 2.6.

	W		
α	0.462	$\pm$	0.014
ϵ	0.671	$\pm$	0.040

Table 2.3: Summary of the values of geometrical acceptance and event selection efficiency. Systematic uncertainties are discussed in Section 2.6.

2.6 Systematic uncertainties

The systematic uncertainties of selection efficiencies, as decomposed in Section 2.5 are assessed here. Various sources of uncertainty are presented and their impact on the total efficiency is estimated.

2.6.1 Distorted material

The upstream material uncertainty influences electron reconstruction and identification efficiencies. An assessment of this contribution is done with dedicated Monte Carlo samples simulated with well-defined detector geometry distortions. Realistic estimates of such were guided by the single hadronic track efficiency measurements performed on 2009 and 2010 datasets of Minimum Bias data events [38]. The following samples have been used:

- Additional material of 0.1 X_0 at calorimeter barrel cryostat and 0.05 X_0 between presampler and first calorimeter layer
- In the Inner Detector: 5% (respectively 10%) increase of material with exclusion of sensitive detectors. Minimum Bias measurements suggest that the reasonable estimate of extra material inside ID is 5%. However, due to larger uncertainties, and the presence of difficult to model service patch panels in the region of $2 < |\eta| < 2.5$, the estimate of 10% will be used in this region.

- A relative increase of 20% of pixel services material.

It has been found, that the impact of additional 20% increase of material amount in SCT services region, as well as 0.15 X_0 at the end of SCT and TRT endcaps is negligible. Table 2.4 summarizes all the results of this estimation.

	$\Delta\epsilon^{reco}/\epsilon^{reco}$	$\Delta\epsilon^{medium}/\epsilon^{medium}$	$\Delta\epsilon^{tight}/\epsilon^{tight}$
Nominal + calo	-0.5%	-0.5%	-0.4%
Nominal + 5% ID	-0.5%	-0.2%	-0.9%
Nominal + 10% ID	-1.0%	-0.4%	-1.8%
Nominal + 20% pixel services	-0.2%	$< 0.1\%$	-0.2%
Total with 5% ID	-1.2%	-0.7%	-1.5%
Total with 10% ID	-1.7%	-0.9%	-2.4%
Weighted total	-1.3%	-0.7%	-1.7%

Table 2.4: Summary of relative changes in electron reconstruction, medium and tight identification efficiencies due to distorted material effects.

Total uncertainty from distorted material is calculated by adding all the contributions with 5% ID material increase for $|\eta| < 2$ and with 10% for $2 < |\eta| < 2.5$ as mentioned above. A weighted average of those numbers is then used as a final estimation of systematic uncertainty from this contribution. Its impact on reconstruction efficiency uncertainty is 1.3%. Medium identification efficiency is affected by 0.7% whereas tight one - by 1.7%. The uncertainties on reconstruction and identification efficiencies are correlated and will be added linearly.

2.6.2 Shifting of discriminating variable distributions

Some discrepancies have been noticed between data and Monte Carlo electron identification efficiencies. A study involving shifting the distributions from Monte Carlo to match observed shapes in data has been performed. An illustration of this procedure can be found in Fig. 2.6. Clearly, it is not the most perfect method for precise estimation of the impact of identification variable modelling on systematic uncertainty (see i.e the TRT high threshold hit distributions), but it provides a simple way to get a rough estimate of the numbers. It has been later checked with data-driven methods [25], that this estimation is consistent with results obtained from more robust methods.

In the medium identification step only a very small variation of electron identification efficiency has been observed. An overall estimate of systematic uncertainty of this step is 1%.

At tight level, more cuts are applied, namely the E/p ratio, B-layer hits (if electron does not cross a dead B-layer module) and a fraction of TRT high threshold hits. Map of dead B-layer channels is implemented in the Monte Carlo and therefore no significant contribution from this cut is observed and the quoted number has to be considered a very conservative estimation, obtained by comparing number of events passing tight selection with and without this particular requirement. Summary of contributions from these cuts is presented in Table 2.5. These contributions are treated as uncorrelated, as the selection is performed on different variables, and will be added in quadrature. The total systematic uncertainty of electron identification efficiency at *tight* level is estimated to be 1.9%.

	Medium cuts	E/p	B-layer hits	TRT HT
Variation	1%	0.3%	0.9%	1.2%

Table 2.5: Relative variations of number of selected signal events due to shifting of discriminating variables used in tight identification. Numbers shown here are obtained after tight electron and E_T^{Miss} selection.

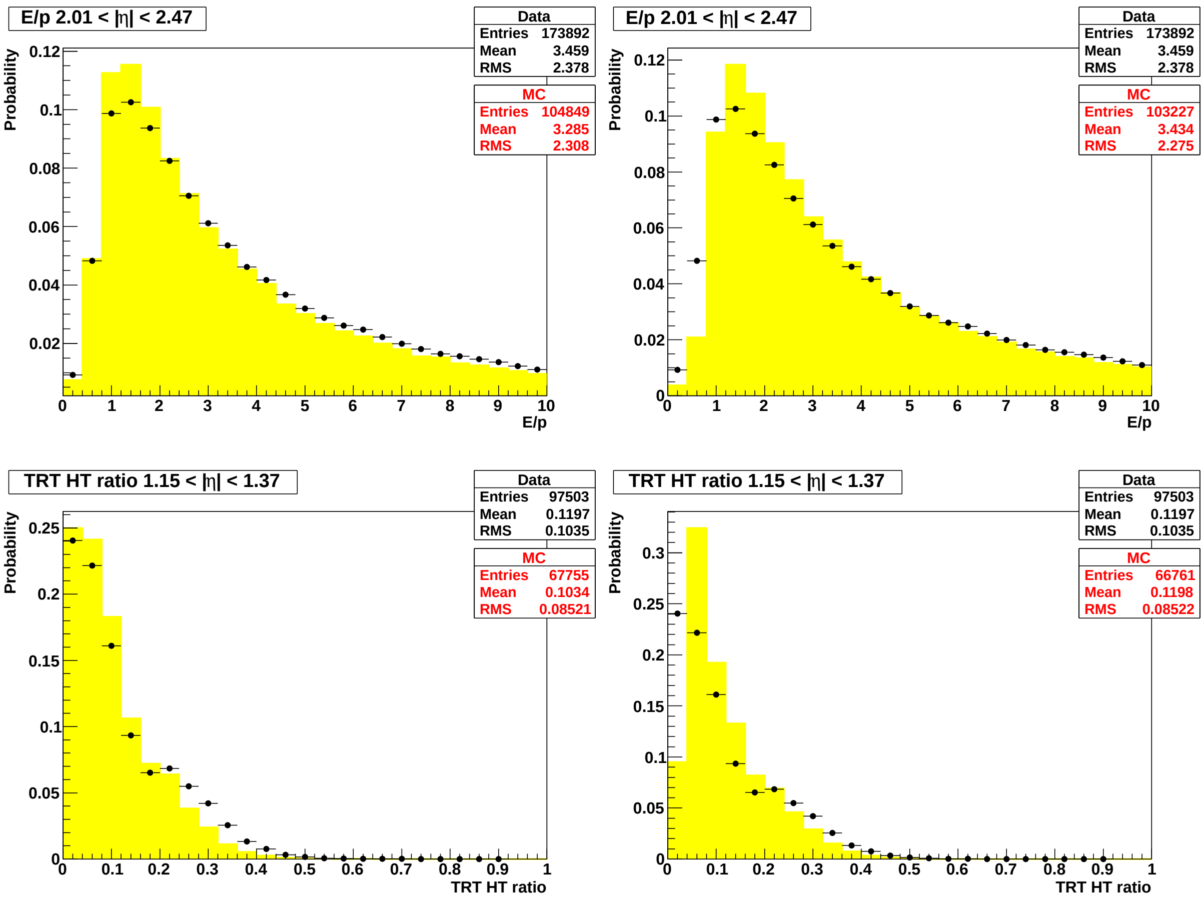

Figure 2.6: An example of shifting of Monte Carlo distributions of discriminating variables (histograms) to match data distributions (points). Left column shows distributions before applying the shift and the right column presents shifted ones. In the top row the ratio of electron cluster energy to track momentum is shown, whereas bottom row presents the fraction of TRT high threshold hits. Clearly, the shifting technique is not perfect in this case.

2.6.3 Pile-up effect on electron identification

Dedicated Monte Carlo samples were produced to estimate the impact of pile-up on electron identification efficiency. A sample with average number of 2 primary vertices per bunch-crossing was produced. Number of collisions per bunch crossing was, however, much lower in data, so a reweighting procedure was applied on simulated samples to match the data. Figure 2.7 shows the fraction of events in data and Monte Carlo as a function of number of primary vertices with at least 3 associated tracks.

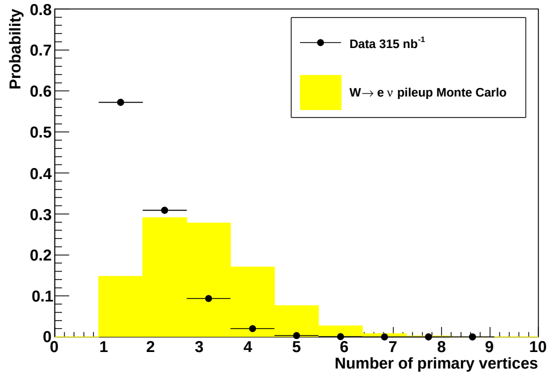

Figure 2.7: Fraction of events in data and various Monte Carlo samples divided into bins by number of primary vertices with at least three tracks.

It has been made after applying trigger selection (and all earlier steps, as described in Section 2.4). Number of primary vertices does not depend on Monte Carlo sample (i.e. signal or background sample).

The relative impact on W-event reconstruction efficiency is found to be almost insignificant, around 0.1%. Tight identification efficiency is affected more, by 0.3% - see Table 2.6.

	Relative difference in efficiency
Reconstruction	0.1%
Medium identification	$< 0.1\%$
Tight identification	0.3%

Table 2.6: Impact of pileup on electron selection efficiency

2.6.4 OTx cut

Dead OTx regions have been simulated in the available Monte Carlo samples. However, a discrepancy between data and simulated events was expected, as not all the affected regions were modelled in the Monte Carlo, as new dead OTx regions were appearing during the data taking. The dead OTx cut is applied at preselection level, both on Monte Carlo and data samples. Difference between acceptances of this cut between Monte Carlo QCD background and data sample is taken as an estimate of systematic uncertainty of this step. It has been found to be 0.8% for electrons from W decays.

2.6.5 Electron energy scale uncertainty

An electron energy scale uncertainty is found to be ±3% from the π^0 studies with 7 TeV collsion data [39]. It affects selection efficiency in several ways. Firstly, electron transverse energy, measured in electromagnetic calorimeter is affected. To estimate this effect, electron transverse energy is varied by $\delta E = \pm 3\%$, as shown in the following equation:

$$E_T(e) \to (1 + \delta E)E_T(e). \tag{2.5}$$

Also, the measurement of transverse missing energy is sensitive to electromagnetic energy scale. Its components are varied as follows:

$$E_x^{Miss} \to E_x^{Miss} - p_x(e)\delta E, \tag{2.6}$$
$$E_y^{Miss} \to E_y^{Miss} - p_y(e)\delta E. \tag{2.7}$$

Moreover, two identification variables used in electron candidate selection, namely hadronic leakage and E/p, are also affected. This effect is assessed using the following transformation:

$$E_{had}/p_T \to E_{had}/(p_T(1 + \delta E)), \tag{2.8}$$
$$E/p \to (1 + \delta E)E/p. \tag{2.9}$$

Table 2.7 summarizes the effect of ±3% and ±1.5% energy scale variation on selection (reconstruction and identification) efficiency. In a conservative approach, a maximum effect is regarded as the systematic uncertainty resulting from energy scale measurement. An overall effect on electron selection efficiency is found to be 1.6%. Adding up the effect on E_T^{Miss} selection linearly as correlated, and considering the maximal variation from default number, a final relative uncertainty of 3.4% is obtained.

	$\delta E + 3\%$	$\delta E + 1.5\%$	$\delta E - 3\%$	$\delta E - 1.5\%$
electron reconstruction	+1.4%	+0.7%	-1.6%	-0.8%
electron identification	-0.4%	-0.2%	0.3%	0.1%
E_T^{Miss} cut	+1.6%	+0.8%	-1.8%	-0.9%
overall	3.1%	1.5%	3.4%	1.7%

Table 2.7: Relative changes in $W \to e\nu$ numbers after energy scale variations with respect to nominal energy scale.

2.6.6 Missing transverse energy

The measurement of transverse missing energy is also affected by sources other than electromagnetic energy scale discussed above, such as energy scale of a clustering algorithm used in E_T^{Miss} reconstruction, impact of pile-up and problematic calorimeter regions . A total uncertainty resulting from those effects has been found to be ±2% [40].

2.6.7 Trigger efficiency

The trigger efficiency is estimated to be 99.8% with an uncertainty of ±0.2% [23].

2.6.8 Other effects

The impact of other effects, such as LAr gain corruption and mismatch between data and Monte Carlo modelling of soft photons has been estimated to be 1.1% [25].

2.6.9 Summary of systematic uncertainties on selection efficiency

A list of all assessed systematic uncertainties for the electron selection (reconstruction and identification) efficiency is given in Table 2.8. In each column, all contributions are treated as uncorrelated and added in quadrature, however a correlation between the final $\Delta\epsilon^{reco}/\epsilon^{reco}$ and $\Delta\epsilon^{tight}/\epsilon^{tight}$ is clear, as the same error sources are involved, so the final numbers from last row of Table 2.8 are added linearly. Total systematic uncertainty of electron selection efficiency is therefore 5.1%.

The final uncertainty of full event selection efficiency is affected by electron selection, energy scale, E_T^{Miss} , trigger and other effects listed before. To avoid double-counting of energy-scale contribution, this term is subtracted from electron selection efficiency uncertainty. Proper treatment of correlations between the influence of energy scale uncertainty on electron and E_T^{Miss} selection efficiencies is presented in Section 2.6.5, resulting in a total impact of electron energy scale on full selection efficiency uncertainty of 3.4%. This is then treated as separate term in final estimation of systematic error. All the listed contributions are treated as uncorrelated. This results in a total systematic uncertainty of event selection efficiency of 6.0%.

	$\Delta\epsilon^{reco}/\epsilon^{reco}$	$\Delta\epsilon^{tight}/\epsilon^{tight}$
Material effects	1.3%	1.7%
Identification variables	-	1.9%
Energy scale	1.6%	0.4%
OTx	0.8%	-
Pile-up	0.1%	0.3%
Other effects	-	1.1
Overall	2.2%	2.9%

Table 2.8: Contributions to systematic uncertainty of electron selection efficiency. Impact of dead material was discussed in Section 2.6.1, contribution from identification variables modelling can be found in Section 2.6.2, whereas the energy scale influence was presented in Section 2.6.5. A total systematic uncertainty of 5.1% on electron selection efficiency has been estimated (see text)

2.6.10 Systematic uncertainty on geometrical acceptance determination

The uncertainty on geometrical acceptance results from limited knowledge of Parton Distribution Functions of a proton and the modelling of W production at the LHC. Three different components are combined to obtain the value of systematic error. The contribution from within one PDF set was obtained with CTEQ 6.6 PDF error eigenvector sets at 90% confidence level limit [41] with combination with MC@NLO [33] acceptance calculation. In addition, a more significant contribution was found between MRST LO* [7], CTEQ 6.6 and HERAPDF 1.0 [42] sets. Differences between PYTHIA [32] and MC@NLO

W production modelling were taken into account as another acceptance uncertainty contribution. An overall uncertainty on geometrical acceptance was found to be ±3% [17].

2.7 Background estimation

As mentioned already in Section 2.2, various possible background sources are considered in this analysis. They can be divided into two main classes: the non-QCD electroweak processes, that involve $Z \to ee$, $Z \to \tau\tau$, $W \to \tau\nu$ and $t\bar{t}$ and QCD dijets. Different approaches are needed to estimate contributions from those two background classes.

2.7.1 Electroweak processes

In this class of events a high-p_T electron is produced from a real W or Z boson. In case of $W \to \tau\nu$, electrons from τ decays are considered. Estimates of numbers of electroweak background events in the final sample are based entirely on Monte Carlo predictions and are obtained by scaling selection acceptance for each process by its cross-section and integrated luminosity. Systematic uncertainty of such procedure includes theoretical cross-section uncertainty of 5.0% for W and Z processes (fully correlated) and 6.0% for $t\bar{t}$. Moreover, 3.0% of acceptance uncertainty is considered as well as 6.7% of selection efficiency, both treated as correlated among all backgrounds. Predicted number of non-QCD background events in the final sample is therefore 36.6±0.2(stat)±3.5(sys)±4.0(lum). A summary is shown in Table 2.9.

Sample	Expected number of events						
$W \to \tau\nu$	25.7	±	0.2 (stat)	±	2.4 (sys)	±	2.8 (lum)
$t\bar{t}$	7.6	±	0.0 (stat)	±	0.7 (sys)	±	0.8 (lum)
$Z \to ee$	1.8	±	0.0 (stat)	±	0.2 (sys)	±	0.2 (lum)
$Z \to \tau\tau$	1.5	±	0.0 (stat)	±	0.2 (sys)	±	0.2 (lum)
Total	36.6	±	0.2 (stat)	±	3.5 (sys)	±	4.0 (lum)

Table 2.9: Background expectations from electroweak processes.

2.7.2 QCD background

The contribution from QCD dijet production to the final sample cannot be estimated in the same way, as for the electroweak processes. The cross-section for this class of processes is determined only at LO and has therefore large systematic uncertainties. A partially data-driven technique has been therefore applied to extract the number of QCD events after final selection. A binned maximum likelihood fit of E_T^{Miss} as discriminating variable was performed. As an input, templates for signal and background samples are needed. The template for QCD background shape was obtained from data, using control sample, selected similarly to $W \to e\nu$ sample but with some cuts from tight identification being reversed and, in addition, electron candidates were required to fail an optional isolation cut. The isolation variable used here is defined as a fraction of transverse energy deposited in a cone of $\Delta R < 0.3$ around electron cluster relative to the transverse energy of the cluster. The value of the cut varies depending on η and E_T of electron candidate, between

$E_T^{\text{cone }0.3}/E_T < 0.062$ and $E_T^{\text{cone }0.3}/E_T < 0.304$. Shape for $W \rightarrow e\nu$ signal is obtained from Monte Carlo with full treatment of pile-up events. Results of the fit are shown in figure 2.8.

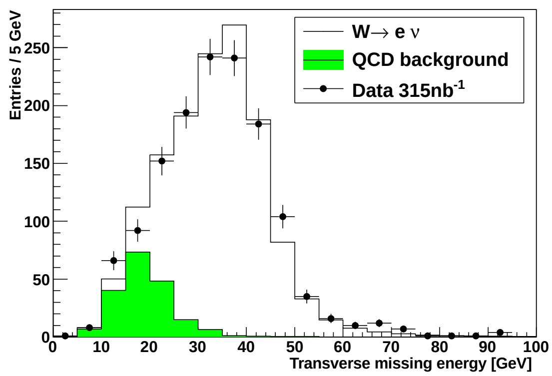

Figure 2.8: Result of E_T^{Miss} template fits in number of QCD background events estimation.

Number of QCD events is estimated to be $N_{QCD} = 27.0 \pm 3.0$(stat). Statistical uncertainty contains contributions from the number of data events and from templates.
Systematic uncertainty of this estimation is obtained by checking three possible contributions. Stability of the result is firstly checked versus the composition of QCD template. This is achieved by requiring the reversed cuts to be passed instead of failed, one by one. The maximum observed variation here is ± 1 event. Secondly, the reversed isolation cut is also varied globally within a range between minimal and maximal cut values over all phase-space ($E_T^{\text{cone }0.3}/E_T > 0.062$ and $E_T^{\text{cone }0.3}/E_T > 0.304$). This reduces the amount of signal events in the background template and also does not allow for too much events with semi-leptonic b-quark decays, that contain genuine E_T^{Miss} . Difference between two extremes is taken to be a systematic uncertainty contribution of the order of ± 8 events. Thirdly, fit range is changed to put a bias on either signal or background dominated regions. For the region of $0 < E_T^{Miss} < 25$ GeV the result varies by ± 1 event, whereas for 15 GeV $< E_T^{Miss} < 120$ GeV the change is ± 2 events.

The total systematic error on this estimation is taken to be ± 11 events which is 40% of relative uncertainty. This is consistent with a Monte Carlo based estimate of number of QCD events using the scaling factor (see Sec. **??**) which is 28$\pm$7(stat).

2.7.3 Summary of background contributions

The total amount of background events described above for 315 nb^{-1} of data after final selection is 63.6$\pm$3.2(stat)$\pm$14.5(syst)$\pm$3.5(lum). Systematic uncertainty consists of all contributions listed above, including 40% on QCD events, 5.0% - 6.0% from electroweak processes normalization, 3.0% of acceptance uncertainty and 6.0% uncertainty of signal selection efficiency. All these numbers are summarised in Table 2.10.

Sample	Expected number of events						
$W \to \tau\nu$	25.7	±	0.2 (stat)	±	2.4 (sys)	±	2.8 (lum)
$t\bar{t}$	7.6	±	0.0 (stat)	±	0.7 (sys)	±	0.8 (lum)
$Z \to ee$	1.8	±	0.0 (stat)	±	0.2 (sys)	±	0.2 (lum)
$Z \to \tau\tau$	1.5	±	0.0 (stat)	±	0.2 (sys)	±	0.2 (lum)
QCD dijets	27.0	±	3.0 (stat)	±	11.0 (sys)	±	0.0 (lum)
Total	63.6	±	3.2 (stat)	±	14.5 (sys)	±	3.5 (lum)

Table 2.10: Background expectations from electroweak and QCD processes.

2.8 Cross-section calculation

The total cross-section for W boson production times the branching fraction of $W \to e\nu$ is expressed by the following formula.

$$\sigma_W^{tot} \times BR(W \to e\nu) = \frac{N_W^{sig}}{\alpha \epsilon L_{int}}. \tag{2.10}$$

In the formula above the following terms are present:

- N_W^{sig} stands for the number of observed signal events in the final selected sample.
- α denotes the geometrical acceptance for W event selection procedure. It is understood as the ratio of events passing kinematical selection applied at generator-level quantities, to the total number of produced events.
- ϵ describes the selection efficiency on candidates within selection acceptance and is calculated as the ratio of events passing final selection on reconstructed variables to the number of events passing acceptance cuts as above.
- L_{int} denotes the total integrated luminosity for the $W \to e\nu$ channel.

Computation details of both central values and uncertainties of all the items listed above was already described in previous Sections of this Chapter. According to the formula above, a final result on $W \to e\nu$ cross-section is the following:

$$\sigma_W^{tot} \times BR(W \to e\nu) = 10.21 \pm 0.33 \text{ (stat) } \pm 0.70 \text{ (syst) } \pm 1.13 \text{ (lum) [nb]} \tag{2.11}$$

Based on the complete analysis, in which the author has taken active part, the ATLAS Collaboration has published a result in [17], which is quoted below:

$$\sigma_W^{tot} \times BR(W \to e\nu) = 10.51 \pm 0.34 \text{ (stat) } \pm 0.81 \text{ (syst) } \pm 1.16 \text{ (lum) [nb]} \tag{2.12}$$

These numbers are in good agreement. Discrepancies in the central values result from minor differences in event cut-flow, which results in different number of events passing full selection chain (the author has obtained 1061 events, whereas in the analysis published by ATLAS this number was 1069). Similarily, the numbers for signal selection efficiency also differ slightly.

2.9 Summary

The theoretical cross-section times branching fraction for the $W \to e\nu$ channel, calculated at NNLO [6] is the following:

$$\sigma^{NNLO}_{W \to e\nu} = 10.46 \pm 0.52 \text{ nb} \tag{2.13}$$

The measured value, published by the ATLAS Collaboration [17] of the cross-section is in a very good agreement with theoretical prediction. Figure 2.9 shows the comparison between the result obtained by ATLAS as a combination of electron and muon[1] channel analysis, and previously available experimental results, namely those from UA1 and UA2 [2] experimets at $\sqrt{s} = 0.63$ TeV at Sp$\bar{p}$S collider, and by Tevatron experiments, CDF[4] and D0[5] at $\sqrt{s} = 1.8$ TeV and $\sqrt{s} = 1.96$ TeV. In addition, a PHENIX[43] measurement from the RHIC accelerator at $\sqrt{s} = 0.5$ TeV is also shown.

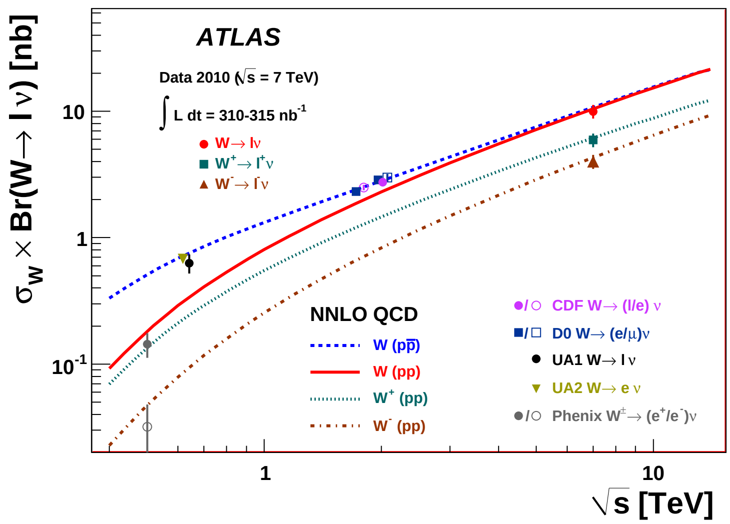

Figure 2.9: Experimental results on $\sigma_W \times BR(W \to \ell\nu)$ compared with NNLO theoretical predictions (see text) from [17].

[1] The cross-section obtained for the muon channel is the following:

$$\sigma^{tot}_{W} \times BR(W \to \mu\nu) = 9.58 \pm 0.30 \text{ (stat) } \pm 0.50 \text{ (syst) } \pm 1.05 \text{ (lum) } \text{ [nb]}. \tag{2.14}$$

It was published in [17]

Chapter 3

Studies on $W \rightarrow \tau\nu$ observability potential with ATLAS detector

3.1 Introduction

In the early period of LHC operation the amount of collected data will allow for a detailed observation of Standard Model (SM) processes. Their role is crucial in the LHC physics program, as it is needed to understand them in terms of unprecedented energy scale of LHC collisions. In particular, cross-sections for $W \to \tau\nu$ and $W \to \tau\nu$ are needed to be measured as these processes form a significant background for the New Physics (NP), such as Supersymmetry (SUSY). Additionally, the performance of τ reconstruction and identification algorithms needs to be well understood for further searches. The $W \to \tau\nu$ process is the first source of isolated medium-p_T τ leptons.

Previous measurements of the $W \to \tau\nu$ process have been performed at Tevatron in $p\bar{p}$ collisions, with $\sqrt{s} = 1.8$ TeV (Run I). The CDF[44] and D0[45] have measured the cross-section for $p\bar{p} \to W \times BR(W \to \tau\nu)$ and the ratio of branching factors $BR(W \to \tau\nu)/BR(W \to e\nu)$, with integrated luminosity of 4.05 pb^{-1} and 18.04 pb^{-1} respectively. The CDF collaboration has also presented the results with Run II data ($\sqrt{s} = 1.96$ TeV) with the sample of 72 pb^{-1}[46].

Such measurement is planned to be repeated at the LHC with first data and low instantenous luminosity. Trigger rates at higher luminosities will exceed the available bandwidth, as the sample of events with hadronically decaying τ leptons is dominated by QCD background events, which are produced with very high cross-section (see Section 3.5). This observation will also be far more difficult than at Tevatron, as the QCD production cross-section is expected to be nearly 100 times larger at 14 TeV than it is at 2 TeV. The signal production cross-section grows only by a factor of 10 in this energy region.

The signal process, $W \to \tau\nu$ at 14 TeV is produced with $\sigma \times BR = 1.7 \times 10^4$ pb at leading order. The sample is dominated by low-p_T W bosons which decay into soft τ leptons with $10 < p_T < 40$ GeV and missing transverse energy (due to escaping neutrino) typically $20 < E_T^{Miss} < 70$ GeV. The background processes, listed in detail in Sec. 3.4 are dominated by QCD di-jet events with cross-section of the order of 10^{10} pb (with hard scattering $p_T^{hard} > 8$ GeV), about 6 orders of magnitude over the signal cross-section. There is however a large systematic uncertainty, which is related to the reliability of the available Monte Carlo predictions for the QCD production at high energies. This uncertainty will influence the amount of background events, but also the trigger rate and thresholds.

In this Chapter we describe the procedure of selecting events, which would allow us to perform observations of hadronically decaying τ leptons and to measure the $W \to \tau\nu$ signal events at the LHC. This selection was performed with the assumption of 14 TeV center-of-mass energy in the collisions. As this selection was intended to be performed in the so-called "first data", we assume 100 pb^{-1} of integrated luminosity with instantenous luminosity of $10^{31} - 10^{32} cm^{-2}s^{-1}$. The current Chapter is organized as follows: Section 3.2 describes the simulation, digitization and reconstruction process, Monte Carlo samples are described in Section 3.4. Section 3.3 lists objects used for this analysis. Trigger performance for these studies is discussed in Section 3.5. A full offline selection of tau events is described in Section 3.7, whereas Section 3.8 is concerned with studies of electron stream.

3.2 Generation, simulation and reconstruction

The Monte Carlo samples used in this analysis were produced with `PYTHIA`[32] Monte Carlo generator, only the $t\bar{t}$ sample was obtained with the `MC@NLO`[33] generator. The `TAUOLA` generator is used to generate the decays of τ lepton and `PHOTOS`[47] was applied to obtain simulated photon radiation. All the samples were generated with $\sqrt{s} = 14$ TeV.

In the generated events, all particles considered as stable before interacting with material of the detector, are stored and afterwards passed through `GEANT4`[30] ATLAS detector simulation. Subsequently, a digitization process is performed on the simulation results converting `GEANT4` output into a detector response signals, adding detector noise and background processes, like beam-gas, beam-halo and cavern background. Also, if required, pile-up is simulated at this step. A Level 1 (hardware-based) trigger decision is simulated directly after this stage. During Monte Carlo sample production no events are discarded due to trigger decisions, however the process of decision-taking is simulated and the result stored for the use in the analysis [31].

3.3 Objects used for analysis

In this analysis a set of default objects, available within ATLAS framework, was used. Full list of these objects is presented below. Full description of those objects can be found in [10].

3.3.1 Tau leptons

This analysis was performed based on tau leptons reconstructed by the track-based reconstruction algorithm, called *tau1p3p*. Such reconstruction is understood as the reconstruction of hadronically decaying τ leptons, as it is very difficult do distinguish leptonic τ decays from primary electrons and muons. A track-based reconstruction is seeded with a leading track of good quality and transverse momentum above 9 GeV. Up to six additional tracks are allowed in the core region ($\Delta R < 0.2$), however region of higher (above three) track multiplicity is considered in this analysis to be signal-free after final selection and may be useful for data-driven QCD-background estimations. Only a minimal energy deposit is allowed in the isolation region around the core cone ($0.2 < \Delta R < 0.4$). In case of many-prong candidates, charge of ± 1 or 0 is required. Energy of such τ candidate is determined using the energy-flow algorithm. Identification of reconstructed track-based τ candidates is performed by calculating both track and calorimeter quantities and the final decision is taken either by cut-based or by more sophisticated decision methods, like neural networks or boosted decision trees [50].

It has to be noted that there exists another τ-reconstruction algorithm, seeded by jets reconstructed from topological clusters [36]. These jets are reconstructed (at the time of this analysis) with a cone-algorithm, in which the cone size was set to be $\Delta R = \sqrt{\Delta\eta^2 + \Delta\phi^2} = 0.4$. Such jet is required to have transverse energy above 10 GeV and to be contained within the acceptance of Inner Detector, $|\eta| < 2.5$. In the next steps tracks are associated with the calorimetric seed if they are contained within a narrower cone of $\Delta R < 0.3$ and fulfil minimum quality requirements. The energy of such τ candidate is calculated from clustered cells, being iteratively summed up with cell weights obtained from H1-style calibration [51]. This algorithm was not used in 14 TeV analysis, but τ-

candidates reconstructed by both track and calorimeter-based algorithms are exploited in 10 TeV $W \to \tau\nu$ studies, described in Section 3.10.

3.3.2 Electrons

Electron objects are reconstructed by standard *egamma* algorithms, with the *isEM* identification flags set to either *loose*, *medium* or *tight*[1] [48] (see also Section 2.3 and Appendix C). Events with *loose* electrons not matched to a τ objects are removed from the final sample, as they, most likely, come from $W \to e\nu$ decays. *Tight* electrons are used in the electron stream analysis, see Sec. 3.8.

3.3.3 Muons

Smilarily to *loose* electrons, events with any reconstructed muon, not overlapping with a reconstructed τ-jet are removed, as these events are dominated by $W \to \mu\nu$ and $t\bar{t}$ background.

3.3.4 Jets

Jet objects are reconstructed with the cone algorithm with $\Delta R = 0.4$ with H1-style calibration, executed on topological clusters [52]. Jet objects are used in the final tau-stream selection, to suppress events with fake-E_T^{Miss} topologies and increase signal to background ratio.

3.3.5 Missing transverse energy

Missing transverse energy is calculated using standard refined procedure[53]. This object is crucial for QCD-background suppression, as it accounts for unobserved neutrinos, present in signal process, but not expected in QCD dijets.

3.4 Monte Carlo samples

Various processes are taken into account for this work, as there are many possible background sources for $W \to \tau\nu$ process. Most of them are easily suppressed at various selection stages, nevertheless their possible contributions need to be estimated and dealt with. Details on the signal and background processes under consideration is given below. Table 3.1 lists all datasets with their production cross-sections.

- **The $W \to \tau\nu$ signal sample**
  The signal sample exploits the generated $q\bar{q} \to W \to \tau\nu$ hard process. It is dominated by low-p_T W bosons decaying into soft τ's and relatively low missing transverse energy. Mean values of the transverse momenta of the system recoiling against the W boson, the visible products of τ lepton decay and the true transverse missing energy are 16.6 GeV, 18.4 GeV and 22.6 GeV respectively (computed at LO).

[1] The electron identification cuts presented in this chapter are based on similar procedures and the same set of variables, as described in Chapter 2 and Appendix C. The cut values however have been separately optimised for 14 TeV collision energy and vary between the presented analyses.

- **The $W \to e\nu$ background sample & control channel**
  This process may mimic the signal process in two ways. The electron can be identified as single-prong τ lepton, or a fake τ may be reconstructed from QCD Initial State Radiation (ISR). To exclude such events we will require a flag from an electron-veto algorithm for τ's and remove the events with isolated electrons. The remaining fraction of events (with lost electrons) will contribute if QCD ISR is reconstructed as fake τ, but its track multiplicity spectrum will be similar in shape to that of QCD dijets.

- **The $W \to \mu\nu$ background sample**
  Similarly to the process above, we can have either a muon reconstructed as single-prong τ or fake τ from QCD ISR. The first case is easily suppressed by requiring hadronic cluster from τ decay. Additionally, events with isolated muons are excluded. Similarly to the case of electrons, the fraction of events with lost muons will contribute to the fake τ's with track multiplicity spectrum similar to that of QCD dijets.

- **The $Z \to ee$ background sample**
  This process may mimic the signal process if one of the electrons is reconstructed as single-prong τ and the other is lost. Similarly to the $W \to e\nu$ case, this can be suppressed using electron-veto on single-prong τ candidates and removing events with identified isolated electrons.

- **The $Z \to \tau\tau$ sample**
  This sample does contain true τ leptons. However, its cross-section is roughly 10 times smaller than the cross-section for signal. It may still contribute, if one of the τ's is completely lost, i.e. not reconstructed as τ, nor electron or muon.

- **The $t\bar{t}$ background sample**
  The $t\bar{t}$ process (with top quarks decaying predominantly into a W boson and b quark), with much smaller cross-section, will contribute, if one of the W bosons decays into τ and the other into pair of quarks or into leptons, that are lost. In other cases it is removed by vetoing events with isolated leptons.

- **QCD background sample**
  This is the dominant background process, with cross-section exceeding the signal cross-section by six orders of magnitude. They are reconstructed as signal events in cases, where one of the jets is wrongly reconstructed as τ lepton. The methods of suppressing the QCD background do actually determine the event cut-flow of this analysis. The overall normalization of this sample has to be attributed by large systematic uncertainty, as we use only the LO predictions from `PYTHIA`.

The samples listed above were produced centrally and belong to official ATLAS Monte Carlo datasets from the Computer System Challenge production from the years 2006 - 2008 [47].

Due to enormous cross-section and high rejection rates when applying selection procedure, it turned out, that the simulated QCD sample was too small. The only possible solution was to perform private production with so-called fast simulation (`ATLFAST I`). The simulation program was processed at Tier2 site (Cyfronet). We have used those events to estimate the amount of QCD background passing the selection cuts.

Tables 3.1 and 3.2 show the details on the used Monte Carlo samples. The $W \to \tau\nu \to e\nu\nu$ background was not included in the analysis. The branching fraction $\tau \to e$ is only 17% and the p_T spectrum of electrons from tau decays is softer than the one from $W \to e\nu$. This reduces the amount of events possibly passing the selection cuts, so this contribution does not change the results significantly. It was later estimate to contribute by about 1.1% of the signal sample after final selection.

Process	Dataset ID	Events	Cross-section
$W \to \tau\nu$ (filtered for $\tau \to had\ \nu$)	005107	50,000	$1.73 \cdot 10^4$ pb
$W \to e\nu$	005104	150,000	$1.73 \cdot 10^4$ pb
$W \to \mu\nu$	005105	175,000	$1.72 \cdot 10^4$ pb
$Z \to \tau\tau$	005179	50,000	$1.70 \cdot 10^3$ pb
$Z \to ee$	005144	50,000	$1.67 \cdot 10^3$ pb
$t\bar{t}$	005200	175,000	$8.33 \cdot 10^2$ pb
QCD J0 ($p_T^{hard} = 8 - 17$ GeV)	005009	$2 \cdot 10^6$	$1.7 \cdot 10^{10}$ pb
J1 ($p_T^{hard} = 17 - 35$ GeV)	005010	$4 \cdot 10^5$	$1.4 \cdot 10^9$ pb
J2 ($p_T^{hard} = 35 - 70$ GeV)	005011	$2 \cdot 10^6$	$9.3 \cdot 10^7$ pb
J3 ($p_T^{hard} = 70 - 140$ GeV)	005012	$2 \cdot 10^6$	$5.9 \cdot 10^6$ pb

Table 3.1: Details on the full simulation Monte Carlo samples used. All cross-sections are at leading order except $t\bar{t}$ (at NLO/NLL). The Z and W cross-sections include the branching fraction to the specified lepton.

QCD process	Comments	Available statistics
$p_T^{hard} = 10 - 70$ GeV	12 bins with 5 GeV interval	$12 \times 5.6 \cdot 10^6$ events
$p_T^{hard} = 70 - 200$ GeV	6 bins with 10-20 GeV interval	$6 \times 2.0 \cdot 10^6$ events
$p_T^{hard} > 200$ GeV		$1 \times 2.0 \cdot 10^6$ events

Table 3.2: Details on the fast simulation Monte Carlo samples (`ATLFAST I`) used.

3.5 Trigger performance

Hadronic τ trigger at Level 1 is based on the information from hadronic calorimeters. It is seeded with calorimeter towers, of the size of around $\Delta\eta \times \Delta\phi = 0.1 \times 0.1$ within $|\eta| < 2.5$ due to Inner Detector and region of high-granularity calorimeter acceptance. Candidates accepted by L1 are subsequently passed to HLT for further confirmation with software algorithms. At L2 a fast procedure performs refinement of the sample, and only the hadronic τ candidates with given quality and energy are further processed at EF with more robust, offline-based reconstruction and selection procedures.

Due to specific event topology, as well as the bandwidth limitations for trigger rates, a E_T^{Miss} -based trigger signatures had also been used. At Level 1, the E_T^{Miss} is not calculated directly, due to time constraints, but rather the calorimeter-based E_x^{Miss} and E_y^{Miss} quantities are compared with a threshold Table and a fast (yet inaccurate) decision is made. It is therefore not desired to use the L1 E_T^{Miss} thresholds in the analysis, and only the lowest possible threshold is applied at trigger selection. At HLT the transverse missing energy calculation is performed and the results are more reliable.

Dedicated trigger has been developed and optimised to select $W \to \tau\nu$ signal events. It was based on the combination of τ-lepton and E_T^{Miss} triggers. Their names, as listed in Table 3.3, in the form of `tauXXi_xeYY` denote threshold values for τ transverse momentum (`XX`) and E_T^{Miss} (`YY`) in GeV. The `i` denotes isolation criteria being applied at trigger level. The optimal trigger for this analysis, namely the `tau20i_EFxe30`, was configured to apply the transverse missing energy threshold of 30 GeV only at the Event Filter level (and 15 GeV at lower levels), as it is considered more reliable with respect to offline selection in further steps.

The expected trigger rates for the aforementioned menu together with other menus proposed for this analysis are presented in Table 3.3. With the optimisation available at the time, when this analysis was completed, it was not possible to keep the exclusive rate of `tau20i_EFxe30` below 10 Hz (which was considered to be the available bandwidth for this analysis). However this option has been implemented and was available for data taking. It is expected that the background rate may be lower with the improved trigger setup, as the performance of transverse missing energy reconstruction at both L1 and EF is improving.

Trigger	Expected rates (Hz)
`tau20i_xe30`	8.2
`tau25i_xe30`	5.7
`tau45i` (prescale 4)	7.1
`tau20i_EFxe30`	50.0

Table 3.3: Estimated trigger rates using QCD datasets specified in Table 3.1 for an optimisation as available in usual ATLAS specifications by the time of writing.

The estimations of trigger rates have been performed for other trigger configurations, as shown in Table 3.3. The number of signal events accepted by alternative triggers is lower than for the `tau20i_EFxe30` configuration. The `tau45i` with prescale factor 4 is the least efficient from the listed menus and in addition does suppress the events with low-p_T τ's due to 45 GeV p_T threshold. The `tau20i_xe30` (requiring 30 GeV E_T^{Miss} thresholds at each level) gives a reasonable statistics of signal events and lies within the acceptable bandwidth, so should be considered as a possible backup solution. Details on the estimated number of selected events with 100 pb^{-1} are presented in Table 3.4.

Several plots are presented below to show the impact of trigger selection on the event samples we use for this analysis. Figure 3.1 shows the influence of trigger selection on the signal sample. Left plot shows the spectrum of transverse visible energy of a tau candidate (no identification cuts applied) with the offline $E_T^{Miss} > 30$ cut applied. A huge reduction of signal events in the interesting region is observed with `tau45i` trigger menu due to both high p_T threshold and prescale factor. Right plot shows the track multiplicity spectrum after the same selection. A possible bias related to different selection criteria is within 10%.

Trigger + offline $E_T^{Miss} > 30$ GeV	$W \to \tau\nu$	($E_T^{\tau-had} < 30$ GeV)	QCD
`tau20i_xe30`	37610	(12950)	$1.6 \cdot 10^7$
`tau25i_xe30`	31500	(8970)	$1.3 \cdot 10^7$
`tau45i` (prescale 4)	4570	(280)	$1.2 \cdot 10^7$
`tau20i_EFxe30`	60900	(18500)	$2.4 \cdot 10^7$

Table 3.4: Estimated number of signal events, after trigger, offline $E_T^{Miss} > 30$ GeV selection and cut-based τ identification for 100 pb^{-1} using the track-based algorithm. Shown in brackets are numbers for events with a τ candidate with $E_T < 30$ GeV. The last column presents the numbers obtained for QCD background.

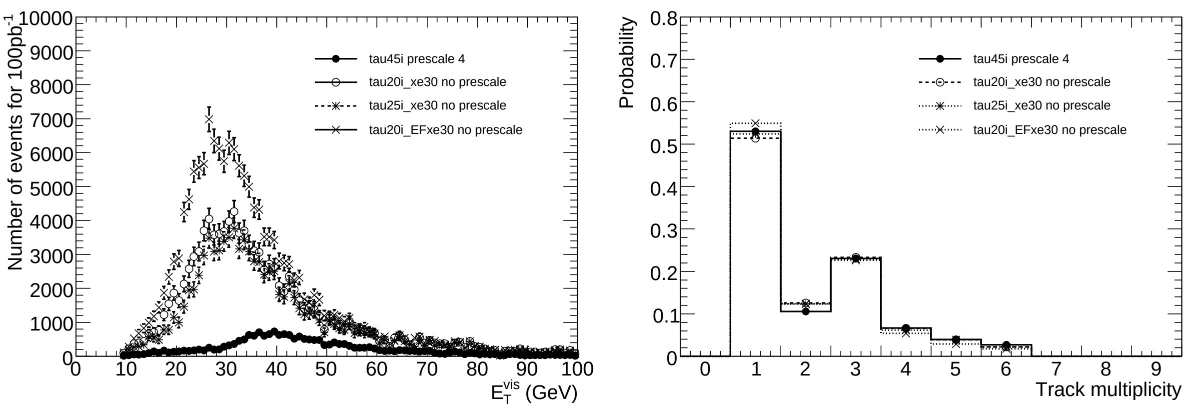

Figure 3.1: Signal event characteristics after trigger selection. Left: The transverse momentum spectra for τ-jet candidates, for an integrated luminosity of 100 pb^{-1}, selected by the triggers `tau20i_xe30`, `tau25i_xe30`, `tau20i_EFxe30` and `tau45i`, and an offline $E_T^{Miss} > 30$ GeV selection. Results were obtained with the track-based algorithm. It is assumed that the `tau45i` trigger is prescaled by a factor 4. Right: The track multiplicity distribution for signal events after the same selection.

Figure 3.2 shows the track multiplicity distributions for all considered processes after trigger selection, left plot shows the signal and all non-QCD backgrounds, whereas in the right plot one can find the track multiplicity distribution for QCD dijets. The non-QCD spectrum is dominated by $W \to e\nu$ process mostly in case of tau reconstructed with one associated track (single-prong bin). The spectrum of QCD background is different, with more events with higher multiplicities. The spectra are presented separately, as the fraction of non-QCD events in the sample after trigger selection is only 0.1%.

As the baseline for this analysis, the trigger menu `tau20i_EFxe30` was chosen, as the most efficient one.

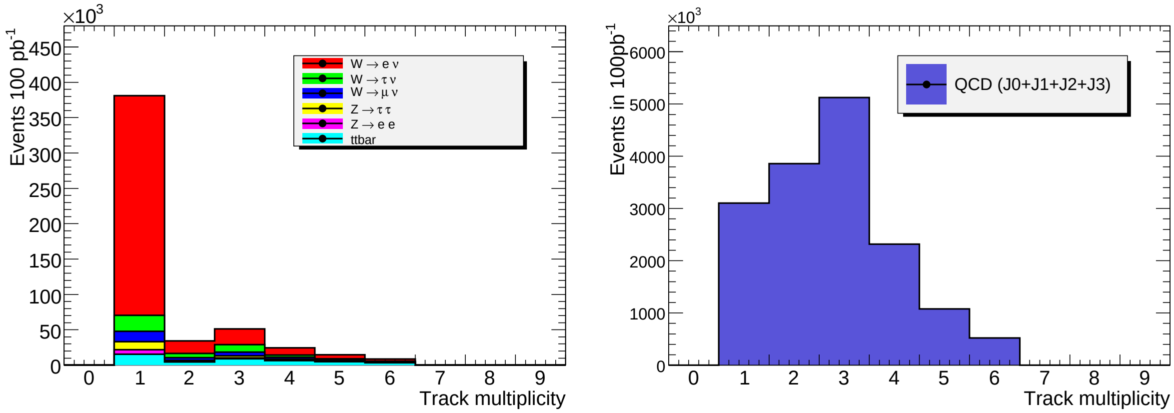

Figure 3.2: The track multiplicity distribution for nonQCD events (left) and QCD events (right) for events accepted by the `tau20i_EFxe30` trigger.

3.6 Offline streams preselection

The event preselection in the τ and electron streams at first requires the offline E_T^{Miss} to be above 30 GeV. This requirement is necessary, as the offline E_T^{Miss} is obtained with the more reliable techniques in comparison to trigger L1 or EF. The correlation plots between the three levels of E_T^{Miss} estimation are shown in Fig. 3.3.

The poor correlation causes further reduction of the selected sample with the offline E_T^{Miss} cut. It reduces the QCD sample by 50% but also a signal sample by 30%. At this point one can divide the events into two exclusive streams - the electron stream and τ stream. Those streams are then studied separately.

- The electron stream preselection requires one *tight* electron (according to the definition in [48]). It selects 2/3 of the triggered $W \to e\nu$ events, around 10% of QCD dijet events available after triggering, and a small addition (around 1% of triggered events) of $W \to \tau\nu$. The rest of the processes do not contribute significantly. This sample can therefore be used to study electron efficiencies and also for modelling the background from QCD ISR events for $W \to \tau\nu$ events, provided the QCD can be further suppressed.
- Tau stream accepts the remaining part of the events. Still, the $W \to e\nu$ contribution to this stream is very significant, and so are the QCD rates, which exceed the amount of selected signal events by a factor of 400. Details on the numbers of accepted events can be found in Tables 3.5 and 3.6).

3.7 Tau stream

The selection of $W \to \tau\nu$ events will be a difficult task, due to a large excess of QCD events above the signal rate after trigger selection. We will first present a procedure of

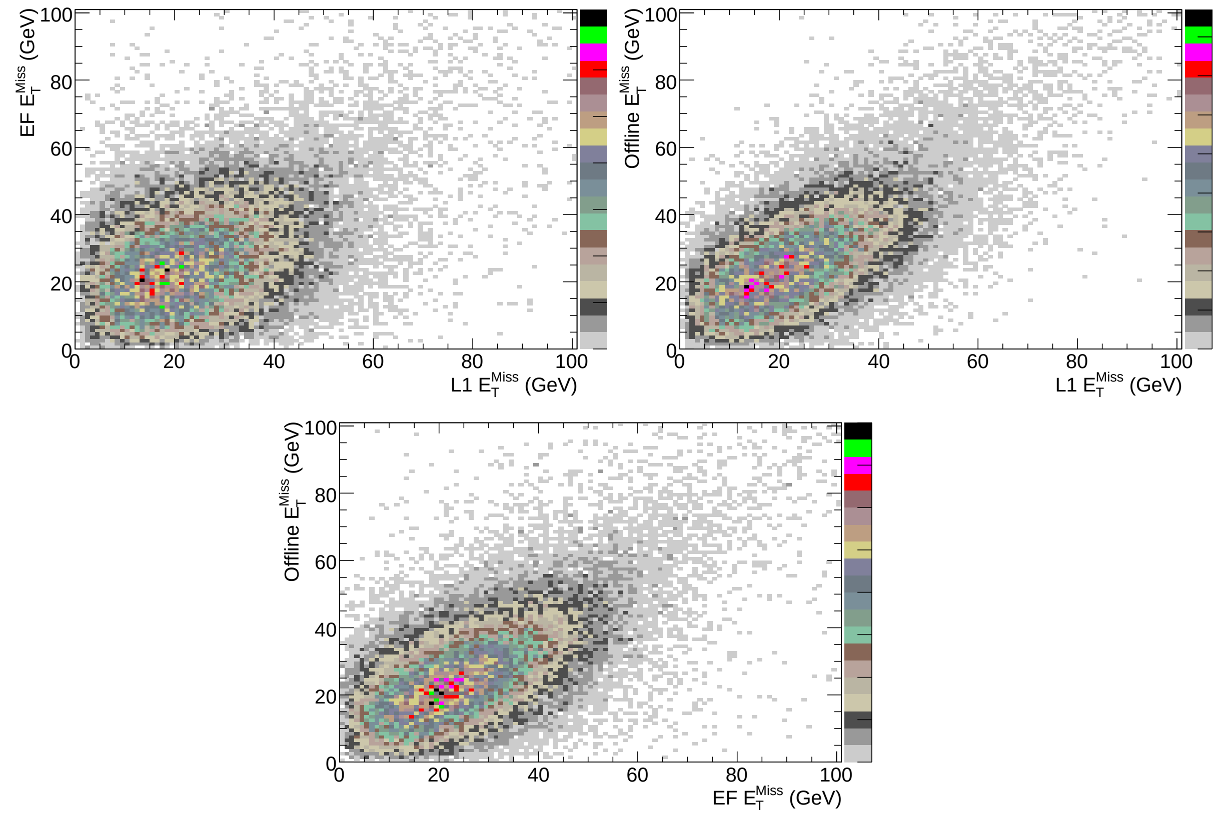

Figure 3.3: The correlations between Level 1, Event Filter and offline E_T^{Miss} calculations for QCD samples.

extracting the signal process from the non-QCD background, and afterwards we will tighten the selection criteria to reduce the amount of QCD background and obtain a reasonable statistics of $W \to \tau\nu$ events.

3.7.1 Event selection versus non-QCD background

The procedure of suppressing the non-QCD background processes is the following:

- each event is required to have a single track-based (see [50]) reconstructed τ candidate with the transverse momentum ranging from 20 GeV to 60 GeV;
- a *loose* cut-based identification requirements were applied on the τ candidate, with the addition of rejecting the candidates flagged by dedicated electron/muon veto algorithms [50];
- events with *loose* (according to default isEM flag [48]) electron with $p_T > 10$ GeV or any muon (combined reconstruction [49]) were reconstructed outside of the τ cone, at the distance of $\Delta R > 0.4$ from the direction of the τ candidate;
- a further tightening of the selection was performed, requiring the τ candidate to

Events in 100 pb^{-1}	$W \to \tau\nu$	$W \to e\nu$	QCD
Trigger `tau20i_EFxe30`	88800	614000	$4.8 \cdot 10^8$
Offline $E_T^{Miss} > 30$ GeV	60900	453000	$2.5 \cdot 10^7$
⇒ Electron stream	400	321000	$9.3 \cdot 10^5$
⇒ Tau stream	60500	132000	$2.4 \cdot 10^7$

Table 3.5: Pre-selection flow for $W \to \tau\nu$, $W \to e\nu$ and QCD events. The number of events in 100 pb^{-1} of data after each selection step is given. The missing $W \to \tau\nu \to e\nu\nu$ sample would add a small contribution to the $W \to e\nu$ background.

Events in 100 pb^{-1}	$W \to \mu\nu$	$Z \to \tau\tau$	$Z \to ee$	$t\bar{t}$
Trigger `tau20i_EFxe30`	32300	15400	27700	19500
Offline $E_T^{Miss} > 30$ GeV	22800	6090	750	16700
⇒ Electron stream	180	920	590	7220
⇒ Tau stream	22620	5170	164	9480

Table 3.6: Pre-selection flow for $W \to \mu\nu$, $Z \to \tau\tau$, $Z \to ee$ and $t\bar{t}$ events. The number of events in 100 pb^{-1} of data after each selection step is given.

pass *medium* selection criteria based on the unweighted Neural Network discriminant (efficNN > 0.3)[50].

Detailed results of the impact of the given selection cuts are shown in Tables 3.7, 3.8 and 3.9. We list specifically number of events with single-prong τ candidates and also show the amount of leptons passing the selection criteria matched to true leptons to measure the purity of selected sample.

Events in 100 pb^{-1}	$W \to \tau\nu$	(true τ)	$W \to e\nu$	(true e)
⇒ Tau stream	60500		132000	
Loose τ-id, $E_T = 20 - 60$ GeV	30000	(26500)	7630	(2690)
1-prong	17900	(16800)	3315	(2550)
Veto events with *loose* lepton	28000	(25100)	3840	(2560)
1-prong	16800	(15800)	2680	(2420)
Medium τ-id (*efficNN* > 0.3)	20200	(19000)	2600	(2190)
1-prong	12650	(12000)	2210	(2090)

Table 3.7: Selection flow for $W \to \tau\nu$ and $W \to e\nu$ events. Number of events surviving the corresponding selection criterion in 100 pb^{-1} of data is shown. Numbers in brackets correspond to truth-matched candidates. The missing $W \to \tau\nu \to e\nu\nu$ sample would add a small contribution to the $W \to e\nu$ background.

As can be seen, the purity of the $W \to \tau\nu$ sample after all mentioned selection cuts is very high, at the level of 94%. About 62% of τ leptons in this sample are single-prong

τ's. The $W \rightarrow e\nu$ events, initially dominating the Tau stream, are easily suppressed with the cuts listed above. As can be seen from Table 3.7, majority of these events passing the selection cuts contribute as single-prong fake τ candidates with electron misidentified as τ. The background from the $W \rightarrow e\nu$ sample is estimated to be 13% of the signal. Recently, the electron veto algorithm has been improved and reoptimised. Only 0.6% of electrons are identified as τ's but there is a loss of τ events of about 10% [54], [55].

Events in 100 pb^{-1}	$W \rightarrow \mu\nu$	(true μ)	$Z \rightarrow \tau\tau$	(true τ)
$\Rightarrow$ Tau stream	22620		5170	
Loose τ-id, $E_T = 20 - 60$ GeV	7000	(970)	2370	(1870)
1-prong	2210	(930)	1510	(1370)
Veto events with *loose* lepton	560	(45)	1560	(1290)
1-prong	160	(45)	1030	(950)
Medium τ-id (*efficNN* > 0.3)	195	(45)	1140	(1050)
1-prong	95	(45)	840	(800)

Table 3.8: Selection flow for $W \rightarrow \mu\nu$ and $Z \rightarrow \tau\tau$ events. Number of events surviving the corresponding selection criterion in 100 pb^{-1} of data is shown. Numbers in brackets correspond to truth-matched candidates.

The $W \rightarrow \mu\nu$ event rate is suppressed with the selection of Tau Stream (down to only 20% of the $W \rightarrow e\nu$ rate), and is further reduced by the next steps of selection. Majority of those events contain the QCD ISR misidentified as τ and a muon. With the cut for rejecting reconstructed muons outside the τ cone a rejection factor of 10 is obtained. After tight τ identification only about 1% of muon contamination is present in the sample.

The $Z \rightarrow \tau\tau$ background process has a 10 times smaller production cross-section in comparison to the signal process and therefore, after the Tau stream selection it is well below the level of the dominant $W \rightarrow e\nu$ background (being approximately 4% the contribution from $W \rightarrow e\nu$). After *medium* τ identification and removal of events with additional muons only a small fraction of those events is present. About 92% of them contain an identified τ matched to true object.

Events in 100 pb^{-1}	$t\bar{t}$	(true τ)	$Z \rightarrow ee$	(true e)
$\Rightarrow$ Tau stream	9480		164	
Loose τ-id, $E_T = 20 - 60$ GeV	2940	(865)	15	(2)
1-prong	985	(590)	4	(2)
Veto events with *loose* lepton	860	(400)	5	(2)
1-prong	370	(280)	2	(2)
Medium τ-id (*efficNN* > 0.3)	430	(300)	4	(2)
1-prong	255	(210)	2	(2)

Table 3.9: Selection flow for $t\bar{t}$ and $Z \rightarrow ee$ events. Number of events surviving the corresponding selection criterion in 100 pb^{-1} of data is shown. Numbers in brackets correspond to truth-matched candidates.

Selection	$W \to \tau\nu$	$W \to e\nu$	Other non QCD bgds.
Trigger `tau20i_EFxe30`	88800	614000	300000
Offline E_T^{Miss} > 30 GeV	60900	453000	53100
⇒ Tau stream	60500	132000	38900
Medium $\tau - id$ + lepton removal	20250	2600	1800
1-prong only	12650	2210	1210

Table 3.10: Expected number of events in 100 pb^{-1} of data for signal and background after subsequent steps of the selection. The missing $W \to \tau\nu \to e\nu\nu$ sample would add a small contribution to the $W \to e\nu$ background.

The remaining contributions, of $Z \to ee$ and $t\bar{t}$ events contain only a small fraction of events present in the resulting sample due to low cross-section and very good suppression via the removal of events with additional leptons.
Table 3.10 summarizes the number of events from each sample after subsequent cuts.

Figure 3.4 presents the plots of track multiplicities after various stages of selection. The top-left plot shows the spectrum after trigger selection. Top-right plot presents this spectrum after tau stream selection, the bottom plots show the track multiplicities after *loose* (left) and *medium* (right) τ identification. The same scheme is used in Figures 3.5, 3.6 and 3.7 showing the distributions of η, p_T and E_T^{Miss} after each cut, respectively.

The distribution of the $efficNN$ discriminant is shown in Fig. 3.8 (without the last cut for obvious reasons). Distribution of events into three classes - single-prong with no π^0 subclusters (type 1), single-prong with π^0 subclusters (type 2), and multiprong (type 3) is presented in Fig. 3.9 after trigger and offline selection (*loose* on the left, *medium* on the right hand side).

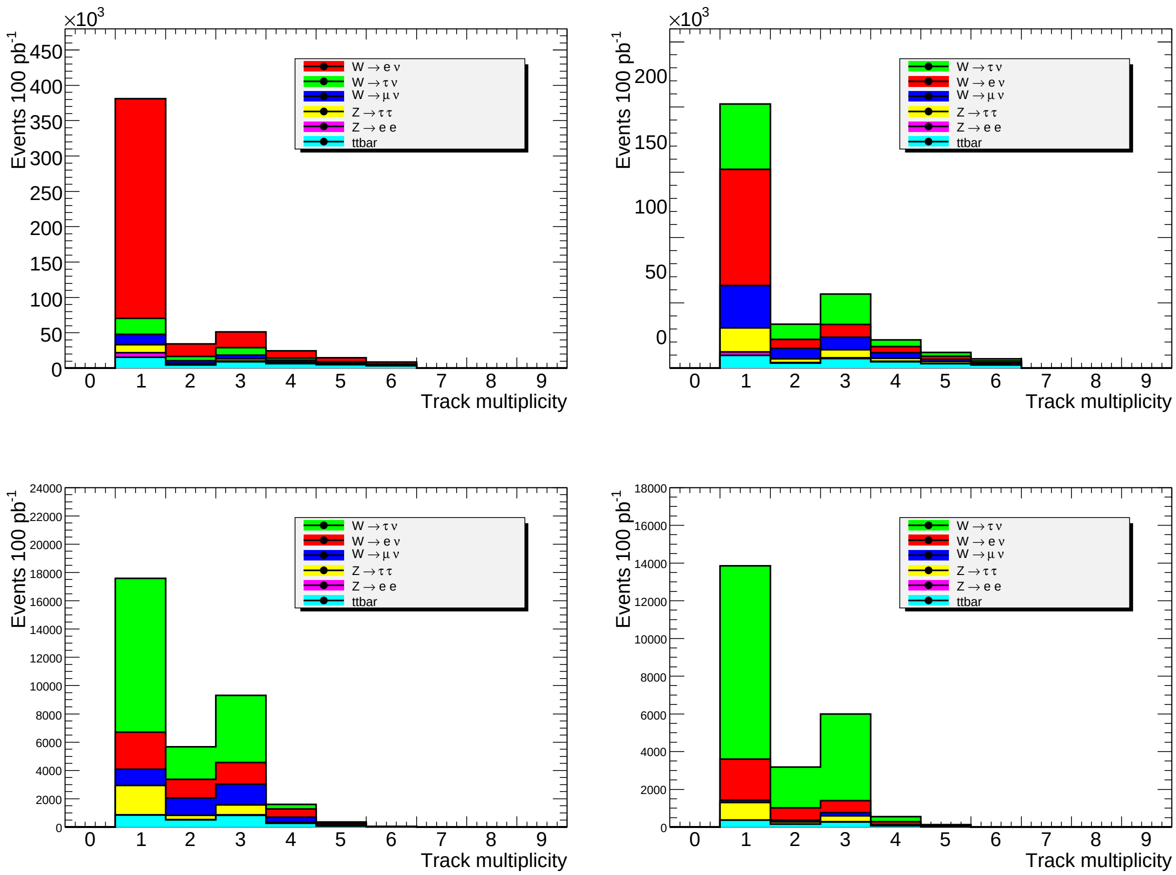

Figure 3.4: The track multiplicity spectra for signal and non-QCD background after `tau20i_EFxe30` trigger (top-left), preselecting into *Tau stream* (top-right), after *loose* τ-id selection (bottom-left) and after *medium* τ-id selection and lepton removal in the rest of the event (bottom-right). *Loose* τ-id includes also selecting τ candidates with $E_T = 20 - 60$ GeV.

3.7.2 The QCD background

As mentioned before, it turned out, that the estimations of QCD event rates after tighter selection criteria cannot be done with the full simulation samples due to low statistics available and high rejection rates of our selection cuts. A cut-flow and breakdown of the number of expected QCD events is shown in Table 3.11. After the preselection into Tau stream the statistical uncertainty of the QCD estimations becomes 25% and it is clear that there is no point in further analysing this fully simulated sample.

An attempt was made to factorize the efficiencies of trigger and offline (τ and E_T^{Miss}) selection. Each of these components does however induce a strong bias on the topology of selected events, so such factorisation is not reliable. The only remaining option was to perform further cutflow and monitor QCD suppression with the fast simulated samples. Where adequate, efficiencies measured on the full simulation samples were applied. More details on the selection procedure is given below.

Events in 100 pb^{-1}	All QCD	p_T^{hard} = 8-17 GeV	p_T^{hard} = 17-35 GeV	p_T^{hard} = 35-70 GeV	p_T^{hard} = 70-140 GeV
Simulation (filter)	1.9e+12	1.8e+12	7.2e+10	9.6e+09	5.9e+08
Trigger `tau20i_EFxe30`	5.0e+08	2.1e+08	1.5e+08	1.2e+08	3.0e+07
Offline $E_T^{Miss} > 30$ GeV	2.5e+07	1.6e+07	4.9e+06	2.9e+06	1.4e+06
⇒ Tau stream	2.4e+07	1.5e+07	4.9e+06	2.9e+06	1.3e+06
statistical error		±25%	±25%	±15%	±5%

Table 3.11: Selection flow for QCD events from fully simulated samples. The number of events expected in 100 pb^{-1} after each selection step are given.

- **Trigger efficiency**
  The trigger decision is not simulated with the `ATLFAST I` fast detector simulation. Due to strong bias on the selected event topology, the factorization of trigger efficiency was not possible. A conservative approach was chosen. We apply only the offline selection criteria to the QCD samples from fast simulation. As it was shown before (see i.e. Table 3.5), it would be reasonable to expect a significant reduction in the number of background events after applying trigger selection criteria because of quite poor correlation between offline and trigger E_T^{Miss} measurement.

- **Tau identification**
  In the fast simulation samples the rejection at reconstruction stage is found to be well matching the rejection obtained with full simulation [57]. Only the τ identification part has to be measured from the full simulation and applied to `ATLFAST I` samples. It was done for each p_T^{hard} bin separately, and then applied as a weight to events from fast simulation from the corresponding p_T^{hard} bin. The measured efficiencies are presented in Table 3.12 for various tightnesses of the selection. The *medium* selection is chosen for this analysis. The range of p_T^{hard} studied with the full simulation (70–140 GeV) were used for all fast simulation QCD samples with $p_T^{hard} > 70$ GeV. For

Identification	*Loose*	*Medium*	*Tight*	*Very tight*
Signal $W \to \tau\nu$ (true τ)	$69.6 \pm 0.5\%$	$59.7 \pm 0.4\%$	$39.6 \pm 0.3\%$	$21.6 \pm 0.2\%$
Sample 005009 (fake τ)	$30.6 \pm 9.7\%$	$9.1 \pm 1.0\%$	$4.6 \pm 0.3\%$	$2.1 \pm 0.1\%$
Sample 005010 (fake τ)	$35.5 \pm 13.0\%$	$13.1 \pm 1.9\%$	$7.3 \pm 0.6\%$	$3.4 \pm 0.1\%$
Sample 005011 (fake τ)	$24.0 \pm 5.7\%$	$5.2 \pm 0.3\%$	$2.5 \pm 0.1\%$	$1.1 \pm 0.01\%$
Sample 005012 (fake τ)	$11.6 \pm 1.4\%$	$1.6 \pm 0.04\%$	$0.7 \pm 0.01\%$	$0.3 \pm 0.001\%$

Table 3.12: The performance of τ-id (only identification part) as measured on the fully simulated samples, without any trigger requirement.

completness, Table 3.13 shows the efficiencies measured on fully simulated samples already after `tau20i` trigger selection. As expected, these efficiencies are 2 - 3 times higher for background events (as the trigger-selected events should be more likely to pass offline cuts) and about 1.1 times higher for signal sample.

Identification	*Loose*	*Medium*	*Tight*	*Very tight*
Signal $W \rightarrow \tau\nu$ (true τ)	$72.7 \pm 0.7\%$	$65.5 \pm 0.6\%$	$44.1 \pm 0.4\%$	$24.2 \pm 0.2\%$
Sample 005009 (fake τ)	$43.0 \pm 20\%$	$16.5 \pm 3.9\%$	$7.9 \pm 0.9\%$	$3.8 \pm 0.2\%$
Sample 005010 (fake τ)	$55.8 \pm 32\%$	$28.8 \pm 8.9\%$	$17.1 \pm 3.2\%$	$8.7 \pm 0.8\%$
Sample 005011 (fake τ)	$43.0 \pm 19\%$	$15.1 \pm 2.4\%$	$8.0 \pm 0.7\%$	$3.5 \pm 0.1\%$
Sample 005012 (fake τ)	$23.0 \pm 5.6\%$	$5.3 \pm 0.4\%$	$2.5 \pm 0.1\%$	$1.1 \pm 0.02\%$

Table 3.13: The performance of τ-id (only identification part) as measured on the fully simulated samples selected by the `tau20i` trigger.

- **Transverse missing energy**
  The reconstruction of E_T^{Miss} in fast simulation has recently been proved to match the gaussian part of the distribution of fully simulated samples[57]. However, the non-gaussian tails cannot be well reproduced, due to a huge contribution from fake E_T^{Miss} which is not simulated with the `ATLFAST I`. This leads to significant discrepancies in the estimation of selected number of events from fast and full simulation samples, as the E_T^{Miss} cut is a crucial part of the presented event selection.
  Figure 3.10 shows the discrepancy of E_T^{Miss} between fast and full simulations. No selection is applied. Clearly, the discrepancy is high, for instance almost 10 times more events are expected to have $E_T^{Miss} > 40$ GeV in the full simulation sample than in the `ATLFAST I` sample. Note, that only 1% of them have true E_T^{Miss} from neutrinos or muons escaping the acceptance region. It would be therefore desireable to reduce the fake E_T^{Miss} contribution and bring the fast and full simulation distributions closer to each other. The following topologies will be removed, as they are known for their significant contribution to fake E_T^{Miss} events:

  - remove events with either τ or a jet identified in the calorimeter crack region ($1.3 < |\eta| < 1.7$);
  - remove events with the transverse direction of E_T^{Miss} close to the direction of τ or jet, namely require, that $|\Delta\phi(E_T^{Miss}, jet)| > 0.5$ and $|\Delta\phi(E_T^{Miss}, \tau)| > 0.5$.

  The effect of those cuts can be observed in fig 3.11. These plots show the ratio of E_T^{Miss} spectra from full and fast simulations for signal (left) and background (right). Input curves, together with a curve for each cut separately and both cuts applied together are presented.

  Clearly, the aforementioned cuts do reduce the discrepancies, and for the signal sample they bring the ratio to 1.0. Still, in the background sample the ratio remains between 4 and 5 within the 40 GeV $< E_T^{Miss} <$ 60 GeV region. More discussion of the fake E_T^{Miss} reduction is presented in Appendix A.

- **Selection flow**
  All the selection criteria listed before have been applied to the high statistics `ATLFAST I` QCD sample. Events with E_T^{Miss} above 30 GeV threshold and no isolated electron are preselected into the Tau stream. A reconstructed τ candidate was required to have transverse momentum between 20 and 60 GeV. Depending on the p_T^{hard} of the

generated event the efficiency measured in full simulation samples was applied. Afterwards, the fake E_T^{Miss} removal procedure was used. The results of this selection on the fast simulated samples is shown in Table 3.14. It does not contain any correction factor for the discrepancies between the fast and the full simulation E_T^{Miss} slopes.

Events in 100 pb^{-1}	All QCD	10-20 GeV	20-35 GeV	35-70 GeV	> 70 GeV
Simulation (filter)	1.9e+12	1.8e+12	7.2e+10	9.6e+09	6.5e+08
Offline E_T^{Miss} > 30 GeV	2.1e+08	5.6e+07	1.0e+08	4.4e+07	5.8e+06
⇒ Tau stream	2.1e+08	5.6e+07	1.0e+08	4.4e+07	5.8e+06
Medium τ-id	1.1e+06	6.7e+04	6.5e+05	2.9e+05	2.4e+04
1-prong	1.6e+05	1.2e+04	1.0e+05	4.4e+04	3.3e+03
Veto fake-E_T^{Miss} topology	7.7e+05	3.4e+04	5.2e+05	2.1e+05	5.4e+03
1-prong	1.3e+05	9.6e+03	8.7e+04	3.1e+04	7.5e+02

Table 3.14: Selection flow for QCD events from fast simulated sample. Numbers are given only for candidates in the signal region, *i.e.* with a track multiplicity equal to one, two or three. Correction factors are not included.

3.7.3 Final selection cuts and the reduction of QCD background

After applying the selection criteria from the previous Section the expected signal to background ratio is around 2.5% (see Tables 3.10 and 3.14). A further suppression is therefore required. It is obtained by requiring a specific event topology with at least one additional jet. The events with E_T^{Miss} above 40 GeV are characterized by a W boson with hard recoil and therefore a significant fraction of those events have an additional jet. Such topology does also make the fake E_T^{Miss} removal more effective. These requirements and their impact on the number of selected signal and background events are shown in Table 3.15, where the last column presents the signal to background ratio after each cut. No correction factor is applied.

As seen in Fig. 3.11 a correction factor on the QCD events is needed, due to discrepancies in E_T^{Miss} spectra between the full (more reliable) and the fast simulation. For the final numbers a factor of 3 is assumed. It is estimated, assuming the 4 - 5 increase factor from the discrepancies in E_T^{Miss} spectra and a factor 2 loss due to poor trigger-offline E_T^{Miss} correlation. After acknowledging this factor the final results are shown in Table 3.16. At the E_T^{Miss} threshold of 50 GeV the signal to background ratio is expected to be 1:3 with 3240 signal events in the resulting sample. An increase of the threshold to 60 GeV of E_T^{Miss} brings the signal to background ratio to 3:1, however it reduces the number of selected signal events down to 1550.

Expected track multiplicity distributions after final selection is shown in Fig. 3.12. The plots in top row are presented for the 50 GeV E_T^{Miss} threshold, whereas the bottom row shows plots with 60 GeV E_T^{Miss} requirement. A correction factor of 3 was applied to the QCD spectra and plots with corrected spectra are shown in the right column of Figure 3.12.

Further optimisation of this selection will be performed using control samples, with the natural candidate of $W \to e\nu$ process events from the same trigger stream. The topology

Selection	$W \to \tau\nu$	QCD dijet	Ratio
Identified τ + E_T^{Miss} > 30 GeV	20250	$1.0 \cdot 10^6$	0.02
E_T^{Miss} > 40 GeV	10200	$1.1 \cdot 10^5$	0.10
Veto fake-E_T^{Miss} topology	9200	$7.0 \cdot 10^4$	0.15
Require jet $p_T > 15$ GeV	6770	$3.0 \cdot 10^4$	0.2
E_T^{Miss} > 50 GeV	4250	$1.8 \cdot 10^4$	0.2
Veto fake-E_T^{Miss} topology	3620	$6.1 \cdot 10^3$	0.6
Require jet $p_T > 15$ GeV	3240	$3.2 \cdot 10^3$	1.0
E_T^{Miss} > 60 GeV	2000	$5.8 \cdot 10^3$	0.3
Veto fake-E_T^{Miss} topology	1580	$4.0 \cdot 10^2$	3.9
Require jet $p_T > 15$ GeV	1550	$1.7 \cdot 10^2$	9.1

Table 3.15: Expected number of signal and background events for an integrated luminosity of 100 pb^{-1}. The QCD background was estimated combining fast and full simulation (see Section 3.7.2), without applying the E_T^{Miss} correction factor. The expected number of events for track multiplicities from one to three, *i.e.* contributing to the signal region only, are shown.

Selection	$W \to \tau\nu$	$W \to e\nu$	$W \to \mu\nu$	QCD dijet	$t\bar{t}$, $Z \to ee, \tau\tau$
Trigger `tau20i_EFxe30`	$8.8 \cdot 10^4$	$6.1 \cdot 10^5$	$3.2 \cdot 10^4$	$5.0 \cdot 10^8$	$6.4 \cdot 10^4$
Identified τ + E_T^{Miss} > 30 GeV	20250	2600	200	$3.0 \cdot 10^6$	1575
E_T^{Miss} > 50 GeV	4250	530	90	$5.0 \cdot 10^4$	550
Veto fake-E_T^{Miss} topology	3620	500	80	$1.8 \cdot 10^4$	150
Additional jet $p_T > 15$ GeV	3240	450	60	9600	80
Increase to E_T^{Miss} > 60 GeV	1550	150	25	500	30

Table 3.16: Expected number of signal and background events for an integrated luminosity of 100 pb^{-1}. The QCD background was estimated combining fast and full simulation, a factor 3 was applied to predictions from the fast simulation (cumulative corrections for trigger and E_T^{Miss} spectrum, see Section 3.7.2). The expected number of events with the track multiplicity of the identified τ in the range one to three (*i.e.* contributing to the signal region only) are given. The missing $W \to \tau\nu \to e\nu\nu$ sample would add a small contribution to the $W \to e\nu$ background.

of those events is similar to that of $W \to \tau\nu$ and it can be used to model the W-boson recoil directly from data. The data-driven tuning of E_T^{Miss} selection is however needed in studies with collision data, as the uncertainties from the Monte Carlo modelling can be huge and difficult to estimate. It is aimed to control the QCD background by events with track multiplicity above 3, as this region is almost signal- and non-QCD-free.

After performing the offline selection, which for the signal process is well understood, we can estimate the trigger efficiency relative to offline selection at various stages. We have processed the full selection chain with and without trigger requirement, and Table 3.17 shows the results with respect to offline selection steps.

Efficiency vs offline selection	`tau20i`	`tau20i_EFxe30`	`tau20i_xe30`
Reco-τ with $p_T > 20$ GeV + $E_T^{Miss} > 30$ GeV	65%	43%	27%
Medium τ-id + veto ele/muo	79%	49%	30%
$E_T^{Miss} > 40$ GeV	79%	62%	47%
$E_T^{Miss} > 50$ GeV	81%	70%	61%
Veto fake-E_T^{Miss} topology	81%	71%	63%
Additional jet with $p_T > 15$ GeV	81%	71%	63%

Table 3.17: Trigger efficiency vs offline selection for signal events.

The τ-only `tau20i` trigger efficiency after final selection step is estimated to be 81% with the optimisation available at the time of this analysis. Additional requirement of E_T^{Miss} at EF level results in 10% loss of signal statistics. Adding the E_T^{Miss} threshold at L1 induces another 8% loss of $W \to \tau\nu$ events.

3.8 Electron stream

Events preselected into the Electron stream will provide a quite clean $W \to e\nu$ sample with the topology similar to $W \to \tau\nu$ events being accepted by the `tau20i_EFxe30` trigger menu. With this sample we can study:

- $W \to e\nu$ background for $W \to \tau\nu$;
- systematics on the QCD initial state radiation and the W recoil in $W \to \tau\nu$.

This channel can also be used to measure the $\sigma(pp \to W) \times BR(W \to e\nu)$. Together with the measurement from Tau stream, it can be then used to extract the $BR(W \to \tau\nu\ )/BR(W \to e\nu)$. In measurement of this ratio several contributions to systematic uncertainties will cancel out. Result of such measurement can be treated as the measurement of electroweak coupling of electron and τ to charged current and a test of lepton universality.

3.8.1 Non-QCD background

Similarly to the Tau stream analysis we will first try to discriminate against the non-QCD background. QCD background suppression will be described in the next Section. The requirements for this selection are listed below.

- The reconstructed isolated electron should have $p_T\ >\ 20$ GeV.
- We reject the evens with additional electron with $p_T\ >\ 10$ GeV or with any muon, both at the distance of $\Delta R\ >\ 0.4$ from the direction of electron. *Loose* identification (isEM) was used for electrons, combined muon reconstruction for muons.
- Fake E_T^{Miss} removal procedure was applied.
- An increase in the E_T^{Miss} threshold was required.

- Similarly to the Tau stream analysis, an additional 15 GeV jet was required to be present in the event.

The selection flow for signal and non-QCD background events is presented in Tables 3.18 and 3.19. As already explained, the $W \to \tau\nu \to e\nu\nu$ was not included but its contribution is small.

Events in 100 pb^{-1}	$W \to \tau\nu$	$W \to e\nu$
⇒ Electron stream	400	321000
Tight electron $p_T > 20$ GeV	90	300000
Veto events with *loose* lepton	90	288000
Veto fake-E_T^{Miss} topology	70	268000
$E_T^{Miss} > 40$ GeV	35	117000
$E_T^{Miss} > 50$ GeV	10	32100
Additional jet with $p_T > 15$ GeV	10	27400
Exactly 1 or 2 jets with $p_T > 15$ GeV	—	22620
$E_T^{Miss} > 60$ GeV	—	10900
Additional jet with $p_T > 15$ GeV	—	10500
Exactly 1 or 2 jets with $p_T > 15$ GeV	—	7960

Table 3.18: Selection flow for $W \to \tau\nu$ and $W \to e\nu$ events. The numbers of events expected in 100 pb^{-1} after each selection step are given. The missing $W \to \tau\nu \to e\nu\nu$ sample would add a small contribution to the $W \to e\nu$ signal.

The resulting purity of the electron sample is high. Plots in Figure 3.13 show the transverse momentum (left) and pseudorapidity (right) distributions for events preselected into electron stream. The non-QCD contributions are also shown. Tables 3.18 and 3.19 show, that these contributions will be strongly suppressed in the course of the analysis. Dominant non-QCD background comes from the $t\bar{t}$ process and is suppressed by the requirement of low jet multiplicity (exactly 1 or 2 jets above 15 GeV). This cut is 80% efficient on the signal and rejects almost all of the $t\bar{t}$ events. This, however, may be affected by unknown systematic uncertainties from the MC generator and also due to expected pile-up. A more precise data-driven tuning will be required.

3.8.2 QCD background for the electron stream

The preselection of events into Electron stream reduces greatly the number of QCD events. Statistical error on the number of accepted QCD events is 100% with full simulation samples, so, similarly to the Tau case, a fast simulation sample was used for further studies. A strategy similar to that of Tau sample was also applied, as follows:

- The performance of the *tight* electron identification is measured on the full simulated QCD sample and then applied to the `ATLFAST I` sample. Numbers obtained from this step are shown in Table 3.20 and Fig. 3.14, where the 8 GeV column should be thought of as the efficiency of Electron stream preselection, whereas the 17 GeV

Events in 100 pb^{-1}	$W \to \mu\nu$	$Z \to \tau\tau$	$Z \to ee$	$t\bar{t}$
⇒ Electron stream	180	920	590	7220
Tight electron $p_T > 20$ GeV	60	470	560	4200
Veto events with *loose* lepton	—	340	150	2065
Veto fake-E_T^{Miss} topology	—	150	30	950
$E_T^{Miss} > 40$ GeV	—	70	5	840
$E_T^{Miss} > 50$ GeV	—	20	—	700
Additional jet with $p_T > 15$ GeV	—	20	—	700
Exactly 1 or 2 jets with $p_T > 15$ GeV	—	20	—	45
$E_T^{Miss} > 60$ GeV	—	10	—	570
Additional jet with $p_T > 15$ GeV	—	10	—	570
Exactly 1 or 2 jets with $p_T > 15$ GeV	—	10	—	40

Table 3.19: Selection flow for $W \to \mu\nu$, $Z \to \tau\tau$, $Z \to ee$ and $t\bar{t}$ events. The number of events expected in 100 pb^{-1} after each selection step are given.

column determines the efficiency of the further offline analysis. Efficiencies measured in the last bin of p_T^{hard} are applied to all events from the fast simulation with $p_T^{hard} > 70$ GeV.

- Rejection of additional *medium* electrons in the fast simulation sample is done on truth level, additional fake electrons are not removed.
- Similarly to the Tau stream, a correction factor of 3 is applied to account for discrepancies in E_T^{Miss} spectra.

Tight electron efficiency	True electron	Fake electron $p_T > 8$ GeV	Fake electron $p_T > 17$ GeV
Sample 005009	10%	0.05%	0.005%
Sample 005010	10%	0.1%	0.01%
Sample 005011	25%	0.1%	0.01%
Sample 005012	25%	0.2%	0.02%

Table 3.20: The efficiencies of the *Tight* electron selection used for estimating the contribution from true isolated electrons and jets reconstructed in the fast simulation. These factors were applied to isolated electrons and jets from fast simulation.

Final selection flow for the total QCD background is presented in Table 3.21.

3.8.3 Final selection on the electron stream

The summary of the selection flow for signal an background samples in the electron stream is summarized in Table 3.22.

For the estimations on the QCD background a combination of fast and full simulations is applied. A correction factor of 3 is already acknowledged in the Table. With transverse

Events in 100 pb^{-1}	QCD all	QCD true ele	QCD fake ele
Simulation (filter)	$1.9 \cdot 10^{12}$		
Offline E_T^{Miss} > 30 GeV	$2.1 \cdot 10^{8}$		
⇒ Electron stream (*tight* electron)	$6.0 \cdot 10^{4}$	$4.6 \cdot 10^{4}$	$1.4 \cdot 10^{4}$
Tight electron p_T > 20 GeV	$1.4 \cdot 10^{4}$	$5.2 \cdot 10^{3}$	$9.2 \cdot 10^{3}$
Veto events with *loose* lepton	$1.3 \cdot 10^{4}$	$4.5 \cdot 10^{3}$	$8.8 \cdot 10^{3}$
Veto fake-E_T^{Miss} topology	$7.5 \cdot 10^{3}$	$8.2 \cdot 10^{2}$	$6.3 \cdot 10^{3}$
E_T^{Miss} > 40 GeV	$8.2 \cdot 10^{2}$	$9.6 \cdot 10^{1}$	$7.2 \cdot 10^{2}$
E_T^{Miss} > 50 GeV	$9.3 \cdot 10^{1}$	—	$9.3 \cdot 10^{1}$
Additional jet with p_T > 15 GeV	$6.0 \cdot 10^{1}$	—	$6.0 \cdot 10^{1}$
Exactly 1 or 2 jets with p_T > 15 GeV	—	—	—
E_T^{Miss} > 60 GeV	$1.8 \cdot 10^{1}$	—	$1.8 \cdot 10^{1}$
Additional jet with p_T > 15 GeV	$1.6 \cdot 10^{1}$	—	$1.6 \cdot 10^{1}$
Exactly 1 or 2 jets with p_T > 15 GeV	—	—	—

Table 3.21: The selection flow for QCD background estimated from the fast simulation. Effects from trigger and E_T^{Miss} differences between fast and full simulation are not included. The number of events expected in 100 pb^{-1} after each selection step are given.

missing energy at the level of 50 GeV already a signal to background ratio is estimated to be 30 with 32100 $W \to e\nu$ signal events selected. Increasing the threshold to 60 GeV reduces the number of signal events to 10900, with S:B ratio around 17. The dominant background is the $t\bar{t}$ process which is reduced by the requirement of low jet multiplicity, which is however a subject to large uncertainties from pileup and MC generators.

Table 3.23 presents the efficiencies of trigger measured versus the offline selected samples. The baseline trigger, `tau20i_EFxe30` is expected to be 92.8% efficient for this selection. Applying a L1 E_T^{Miss} threshold would reduce the efficiency down by 4%. The pure τ trigger, `tau20i` is 95.7% efficient for the full offline selection in the electron stream.

3.9 Summary

In this Chapter we have discussed the perspectives for the $W \to \tau\nu$ observation in first 100 pb^{-1} of ATLAS data with LHC operating at nominal energy of 14 TeV with instantenous luminosity of $10^{31} - 10^{32} cm^{-2}s^{-1}$. The signature for the process under consideration is a hadronically decaying τ lepton and a large transverse missing energy. A dominant background process, the QCD dijet events, are difficult to suppressed, as their cross-section exceeds the signal cross-section by six orders of magnitude. Other non-QCD processes also contribute as the background, with $W \to e\nu$ being the most abundant one. Limited statistics of the fully simulated QCD sample required to use fast detector simulation, the `ATLFAST I`. Other samples were produced with full simulation of the ATLAS detector.

The event selection based on these signatures included the trigger of $\tau + E_T^{Miss}$, a requirement on the transverse momentum of the τ lepton to be between 20 and 60 GeV (as soft τ's are expected from W decay) and offline E_T^{Miss} above 60 GeV. Events with other

Events in 100 pb^{-1}	$W \to e\nu$	$t\bar{t}$	QCD	Other non QCD
Trigger `tau20i_EFxe30`	$6.1 \cdot 10^5$	19500	$4.8 \cdot 10^8$	$4.1 \cdot 10^5$
Tight electron $p_T > 20$ GeV	$3.1 \cdot 10^5$	4200	$4.2 \cdot 10^4$	1230
Veto events with *loose* lepton	$3.0 \cdot 10^5$	2065	$3.9 \cdot 10^4$	610
Veto fake-E_T^{Miss} topology	$2.7 \cdot 10^5$	950	$2.2 \cdot 10^4$	260
$E_T^{Miss} > 40$ GeV	$1.2 \cdot 10^5$	840	2460	110
$E_T^{Miss} > 50$ GeV	32100	700	270	30
Additional jet with $p_T > 15$ GeV	27380	700	180	20
Exactly 1 or 2 jets with $p_T > 15$ GeV	22610	45	180	20
Increase to $E_T^{Miss} > 60$ GeV	10900	570	50	10
Additional jet with $p_T > 15$ GeV	10500	570	35	20
Exactly 1 or 2 jets with $p_T > 15$ GeV	7965	40	35	20

Table 3.22: Expected number of signal and background events in the *Electron stream* for an integrated luminosity of 100 pb^{-1}. The QCD background was estimated from fast simulation, with a scaling factor of 3 to account for trigger acceptance and the difference between full and fast E_T^{Miss} simulations, as done for the *Tau stream* analysis. The missing $W \to \tau\nu \to e\nu\nu$ sample would add a small contribution to the $W \to e\nu$ signal.

Efficiency vs offline selection	`tau20i`	`tau20i_EFxe30`	`tau20i_xe30`
Tight electron with $p_T > 20$ GeV + $E_T^{Miss} > 30$ GeV	97.0%	89.0%	72.7%
Veto ele/muo	96.1%	89.5%	73.1%
$E_T^{Miss} > 40$ GeV	96.2%	90.0%	73.5%
$E_T^{Miss} > 50$ GeV	95.8%	92.6%	83.5%
Veto fake-E_T^{Miss} topology	95.0%	92.2%	88.3%
Additional jet with $p_T > 15$ GeV	95.7%	92.8%	89.0%

Table 3.23: Trigger efficiency with respect to offline selection for $W \to e\nu$ events.

identified leptons were rejected. We have also removed events with fake E_T^{Miss} topology i.e. events with jets pointing to crack region in calorimeter and events with the E_T^{Miss} aligned with the direction of jet. An additional requirement of an extra jest with $p_T > 15$ GeV was applied. As a result, we got 1550 signal events accompanied by around 700 of events from background processes. A characteristic shape of the track multiplicity spectra is expected, with peaks at 1 and 3 tracks.

The expected observability potential is not as encouraging, as the Run II Tevatron results [46]. However, at the energies of the LHC the initial signal to background ratio is ten times worse than at the Tevatron. Also the QCD activity at LHC will be higher, so calorimetric measurements are expected to be more difficult.

A similar selection was applied to extract events from the $W \to e\nu$ process, exchanging the requirement of an identified τ lepton to a *tight* electron. This will provide a good control sample for the $W \to \tau\nu$ analysis and will help to obtain the ratio of branching fractions of the W boson to τ and e and a test of lepton universality.

This analysis was conducted with the assumption of LHC center-of-mass energy $\sqrt{s} =$ 14 TeV. Later, a decision was made, that the collision energy would be lower, $\sqrt{s} = 10$ TeV. Author has also taken part in the preparation for analysis with 10 TeV centre-of-mass energy, and its basic points will be described in Section 3.10. The author has not taken part in 2010 data-based $W \to \tau\nu$ observation at $\sqrt{s} = 7$ TeV, but the procedure exploited there is based on the analysis strategy described in this Chapter.

3.10 $W \to \tau\nu$ observability with $\sqrt{s} = 10$ TeV

The results presented in the previous Sections have been obtained with the assumption of $\sqrt{s} = 14$ TeV of LHC collision energy. After completion of this work an update was made with the assumption of $\sqrt{s} = 10$ TeV center-of-mass energy. The author has taken active part in this analysis, which is documented in [20].

3.10.1 Main differences vs 14 TeV studies

The list below presents main differences between the analyses performed with 10 TeV and 14 TeV center-of-mass energy. Methodology of the work is the same, however some selection cuts differ.

- The predicted cross-section for signal production is lower and for $\sqrt{s} = 10$ TeV it is 7.7 nb, in comparison to 17.3 nb for $\sqrt{s} = 14$ TeV. Also the QCD dijet rate is lower, 1.2×10^7 nb in comparison to 1.8×10^7 nb. This results in reduced trigger rates, so lower thresholds are considered. Final trigger configuration for 10 TeV studies of this channel has been choosen as `tau16i_loose_EFxe25`, which means that looser identification criteria on τ lepton are applied (no actual change of τ transverse momentum is applied, only a change of trigger name was made) and the E_T^{Miss} threshold has changed from 30 GeV to 25 GeV at Event Filter level. L1 and L2 thresholds remain unchanged. Cross-sections for other background processes are also lower.

- Transverse missing energy requirement was loosened to $E_T^{Miss} > 40$ GeV. This is due to much softer spectrum of $W \to \tau\nu$ missing transverse energy in comparison with 14 TeV case. The E_T^{Miss} spectrum does not change for QCD events, so loosening of this cut makes the selection more difficult.

- By the time of performing the analysis, the merging of τ reconstruction algorithms was performed [58]. In this analysis the candidates reconstructed by both, track and cluster-seeded algorithms are considered.

- In order to prepare for early data analyses the τ identification cuts have been changed from neural network selection to so-called *Tight Safe Cuts*. This identification procedure is based only on discriminating variables considered *safe*, where no significant discrepancies between simulation and real data are expected. Rejection power of this discriminant is worse, but provides potentially lower systematic uncertainty on the selection efficiency.

- The veto of events with fake-E_T^{Miss} topology has evolved. A cut of $|\Delta\phi(\tau, E_T^{Miss})| > 2.5$ was applied. No presence or absence of additional jet was required, as the studies have proven that it does not help in reducing the background. However, the event was rejected, if any jet was reconstructed within the uninstrumented hadronic calorimeter region, $1.3 < |\eta| < 1.7$, as such events could case the presence of fake-E_T^{Miss}.

- QCD dijet events were simulated using `ATLFAST II` ATLAS fast simulation package, to provide sufficient statistics for this analysis. Corrections, derived from the comparison of the samples from fast and full simulations, are applied to scale the expected number of QCD events to more reliable level. The observed discrepancies are significant in E_T^{Miss} spectra, and, in addition, no trigger simulation is available with `ATLFAST II` at the time of writing.

- All other selection cuts have been applied, as in 14 TeV studies.

3.10.2 Results of the selection

The results of the selection on various data samples (signal and backgrounds) are shown in Tables 3.24 and 3.25, which can also be found in [20].

Cut	$W \to \tau\nu$	$W \to \tau(lep)\nu$	$W \to e\nu$	$W \to \mu\nu$	$t\bar{t}$
Total events	769000	364008	1035285	1035285	37360
Trigger	85304(313)	22576(122)	463939(235)	18678(63)	10943(13)
$E_T^{Miss} > 40$ GeV	25861(179)	6618(68)	147299(165)	103334(47)	7477(11)
τ identification	5617(85)	1735(35)	74444(122)	1223(16)	1657(6)
τ lepton flag	5341(82)	166(11)	2845(25)	1049(15)	450(3)
Lepton veto	3914(71)	35(5)	384(9)	75(4)	98(2)
Veto jet in crack region	3451(66)	29(5)	345(9)	67(4)	51(1)
$\Delta\phi(\tau, E_T^{Miss}) > 2.5$	2273(54)	22(4)	281(8)	52(3)	6(4)

Table 3.24: Cut-flow for signal, W and $t\bar{t}$ events normalized to 100 pb^{-1} [20].

Cut	$Z \to \tau\tau$	$Z \to ee$	$Z \to \mu\mu$	QCD	QCD (scaled)
Total events	112837	98381	98381	1.26×10^{12}	1.26×10^{12}
Trigger	9211(31)	3262(8)	1546(6)		
$E_T^{Miss} > 40$ GeV	2231(16)	21(1)	280(2)	$135(2) \times 10^5$	$95(5) \times 10^5$
τ identification	534(8)	3.4(3)	35(1)	$49(5) \times 10^3$	$24(5) \times 10^3$
τ lepton flag	378(7)	0.32(8)	28(1)	$43(4) \times 10^3$	$20(4) \times 10^3$
Lepton veto	183(5)	0.04(3)	1.9(2)	$20(3) \times 10^3$	$10(3) \times 10^3$
Veto jet in crack region	152(4)	0.04(3)	1.6(2)	$96(10) \times 10^2$	$34(5) \times 10^2$
$\Delta\phi(\tau, E_T^{Miss}) > 2.5$	82(3)	0.04(3)	1.1(2)	$15(4) \times 10^2$	$7(3) \times 10^2$

Table 3.25: Cut-flow for background Z and QCD events. The last column shows the expected number of events after fast simulation corrections (see text) [20].

The obtained signal to background ratio with this selection procedure is expected to be $S : B = 1.2$ without fast simulation corrections and $S : B = 2.0$ after applying these corrections. It has to be stated, that the expected number of QCD events has a large uncertainty on Monte Carlo cross-section. Final results are also presented in Fig. 3.15.

3.10.3 Summary

The extraction of signal events from enormous QCD background has proven to be more difficult with 10 TeV center-of-mass energy in LHC collisions. However, a signal-to-background ratio above 1.0 is expected. Nevertheless, with further lowering of LHC collision energy, a more robust procedure of selection was needed. It has, in fact, been further improved for $\sqrt{s} = 7$ TeV searches, allowing for first observation of $W \to \tau\nu$ at this energy [18]. The optimised analysis strategy is based on the procedure presented in earlier Sections of this Chapter, for 14 TeV and 10 TeV analyses, with the addition of cut optimisation, which significantly reduce QCD background contribution even further [18].

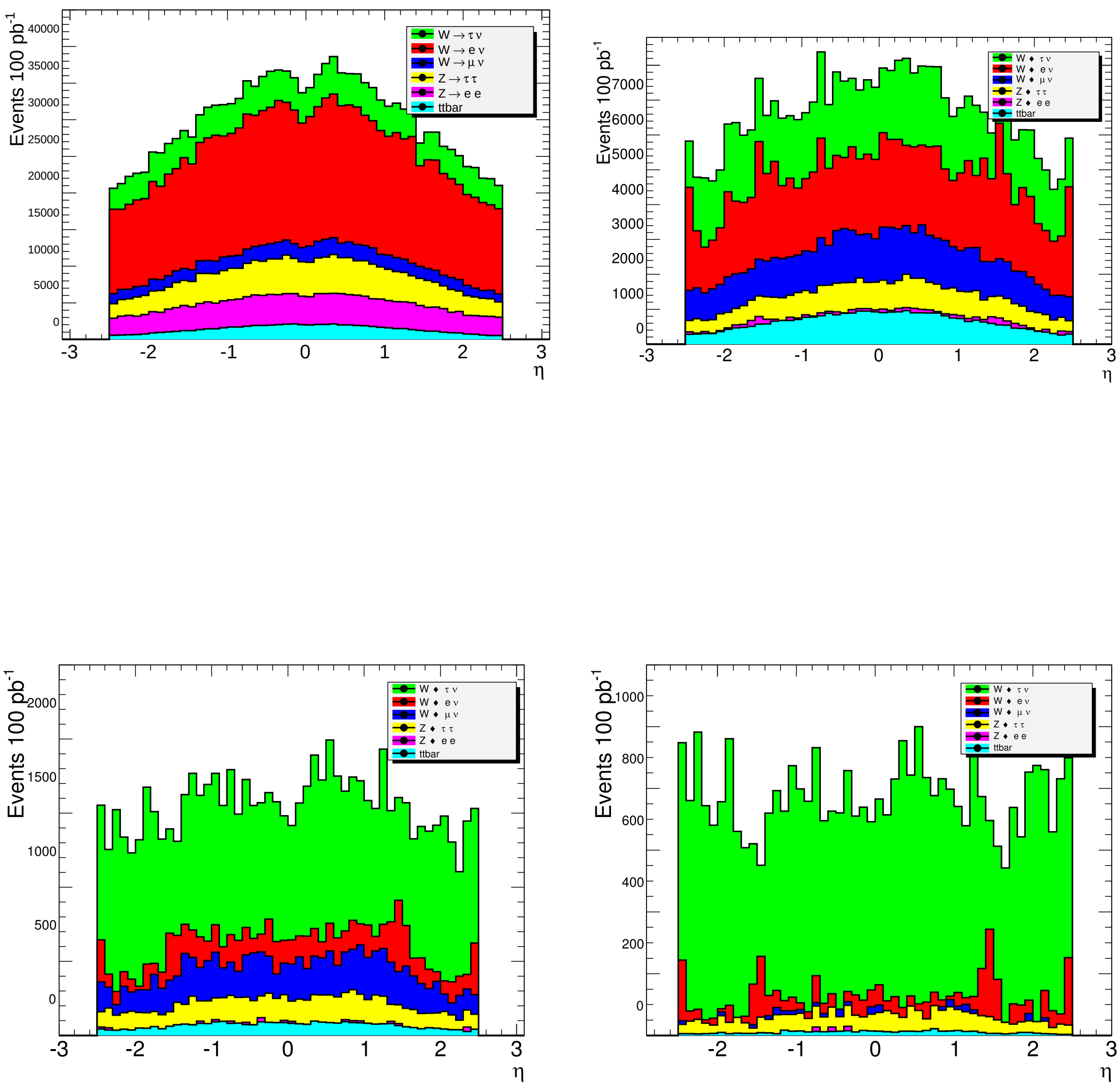

Figure 3.5: The pseudorapidity distribution for signal and non-QCD background after `tau20i_EFxe30` trigger (top-left), preselecting into *Tau stream* (top-right), after *loose* τ-id selection (bottom-left) and after *medium* τ-id selection and lepton removal in the rest of the event (bottom-right). *Loose* τ*-id* includes also selecting τ candidates with $E_T = 20 - 60$ GeV.

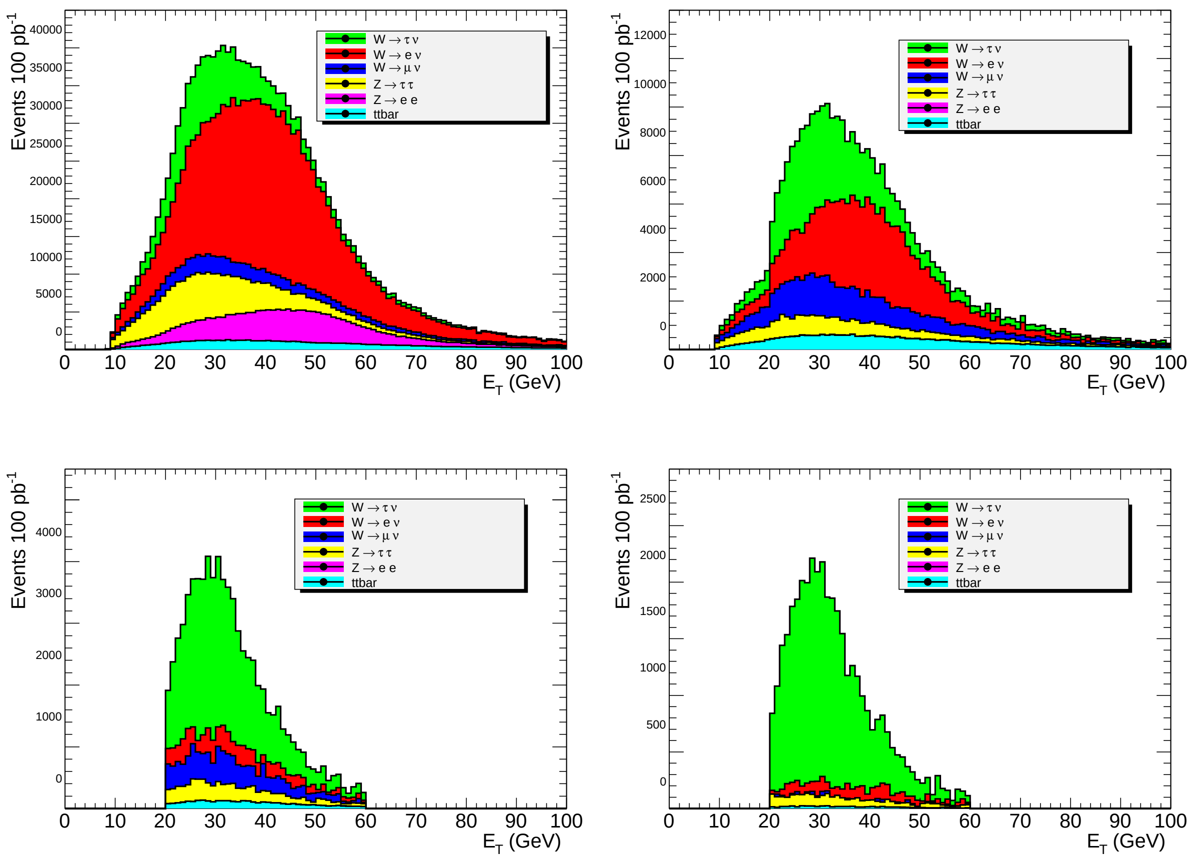

Figure 3.6: The transverse momenta distribution for signal and non-QCD background after `tau20i_EFxe30` trigger (top-left), preselecting into *Tau stream* (top-right), after *loose* τ-id selection (bottom-left) and after *medium* τ-id selection and lepton removal in the rest of the event (bottom-right). *Loose* τ*-id* includes also selecting τ candidates with $E_T = 20 - 60$ GeV.

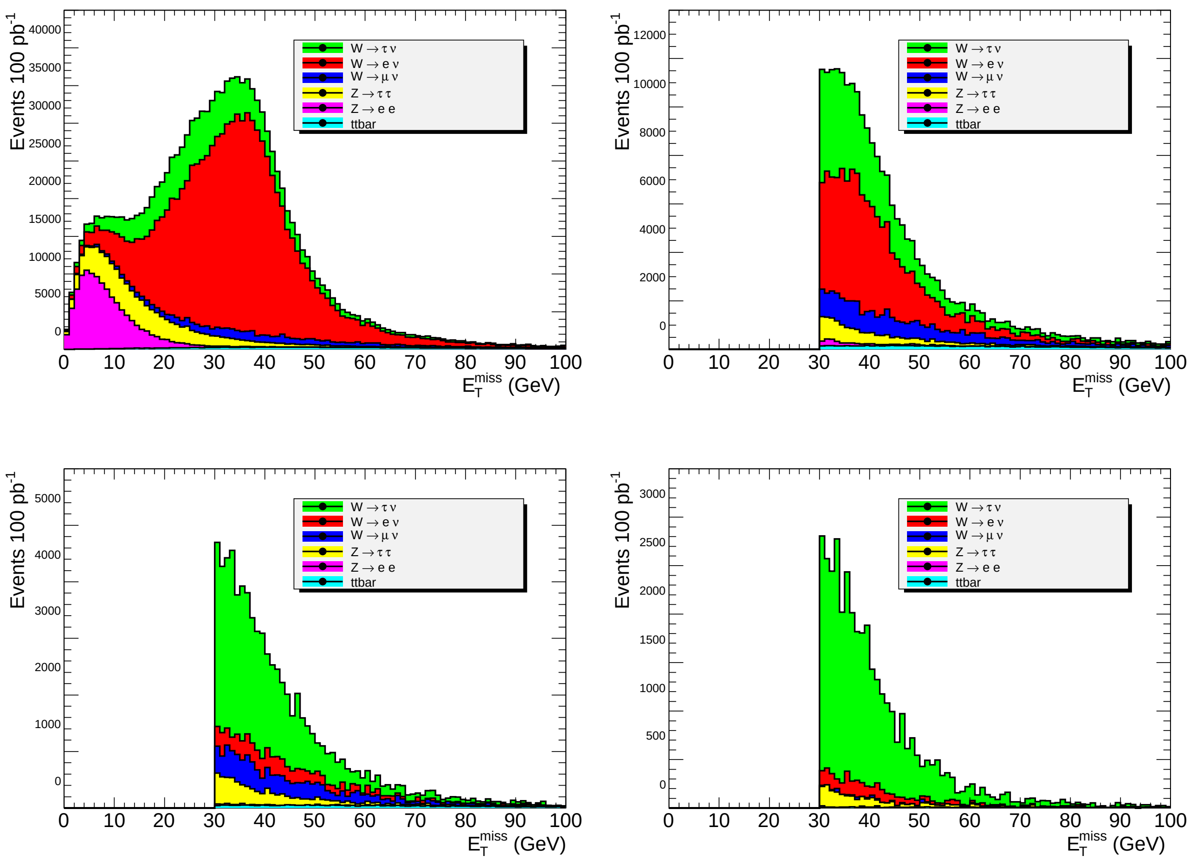

Figure 3.7: The missing transverse energy distribution for signal and non-QCD background after `tau20i_EFxe30` trigger (top-left), preselecting into *Tau stream* (top-right), after *loose* τ-id selection (bottom-left) and after *medium* τ-id selection and lepton removal in the rest of the event (bottom-right). *Loose τ-id* includes also selecting τ candidates with $E_T = 20 - 60$ GeV.

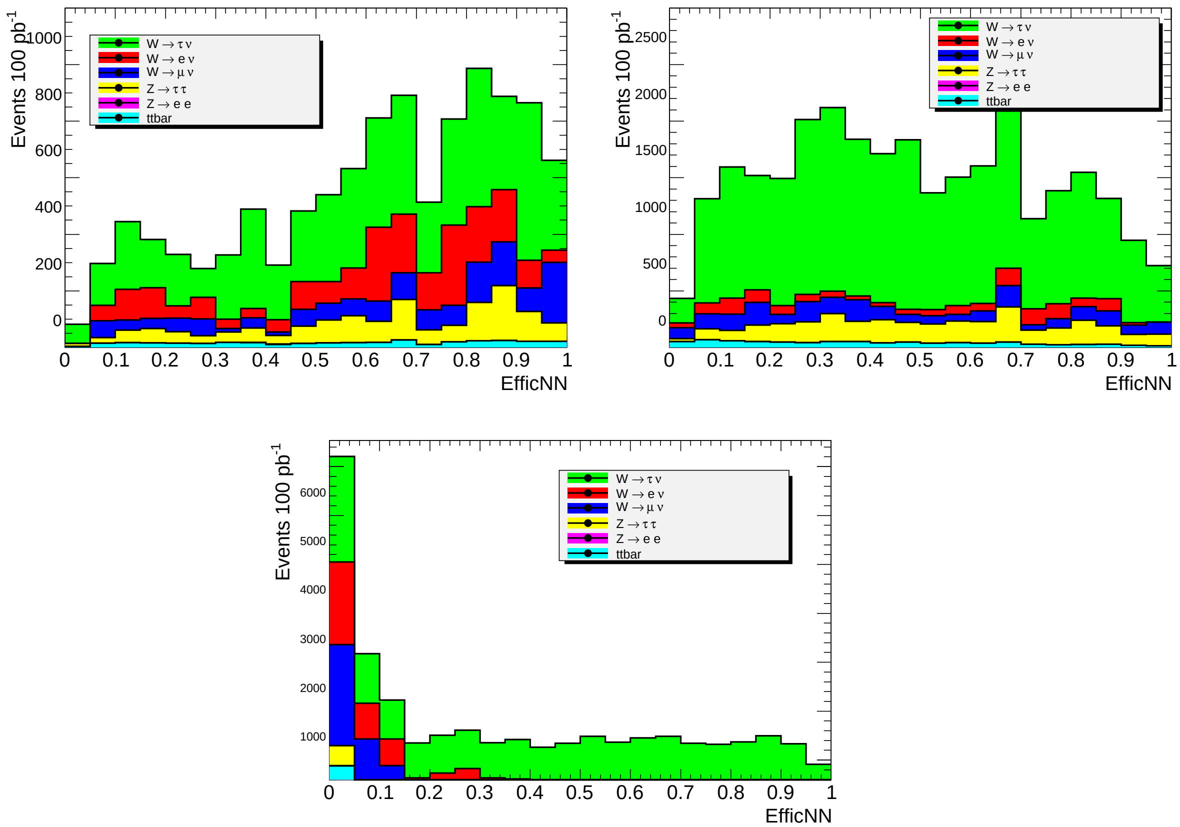

Figure 3.8: For events after *loose* τ identification, the unweighted Neural Network discriminant (*efficNN*) for: single-prong candidates without π^0 subclusters (Type=1, top-left) and with π^0 subclusters (Type = 2, top-right), and for multi-prong candidates (Type=3, bottom). The selection *efficNN*> 0.3 is used for *medium* τ identification.

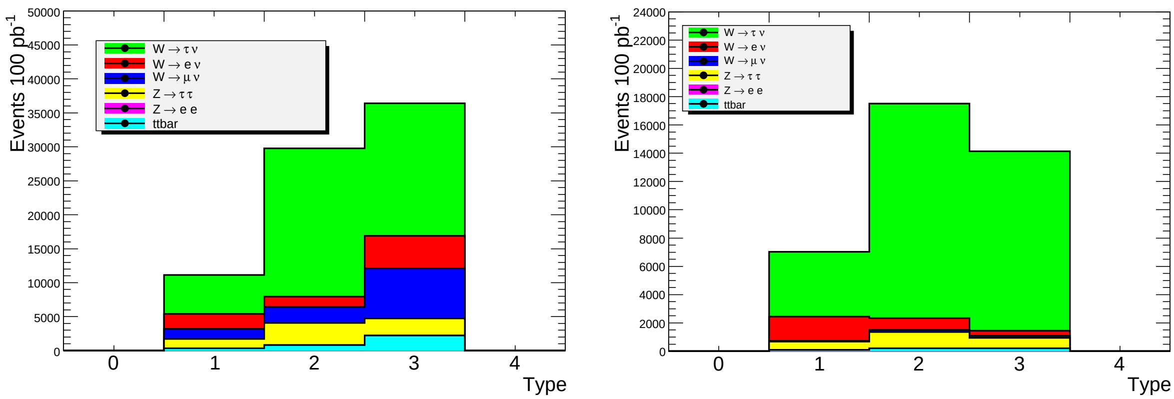

Figure 3.9: The signal and nonQCD background contribution to different types of τ candidates of Type=1, 2, 3, after *loose* τ identification (left) and *medium* τ identification (right), shown for events triggered with the `tau20i_EFxe30` trigger and further selected for the *Tau stream*, as described in the text.

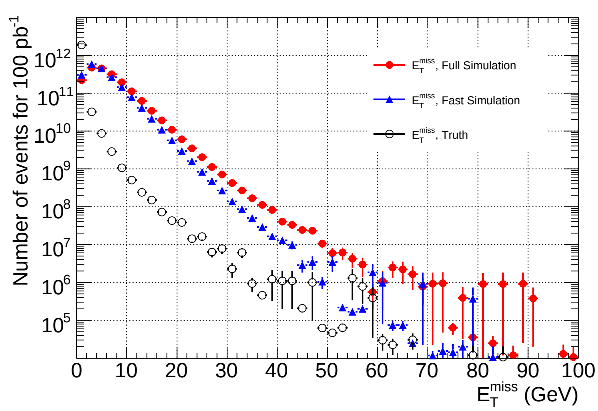

Figure 3.10: The QCD E_T^{Miss} spectrum as reconstructed from the full and fast simulations of the detector, as well as the true E_T^{Miss} spectrum. No selection was applied.

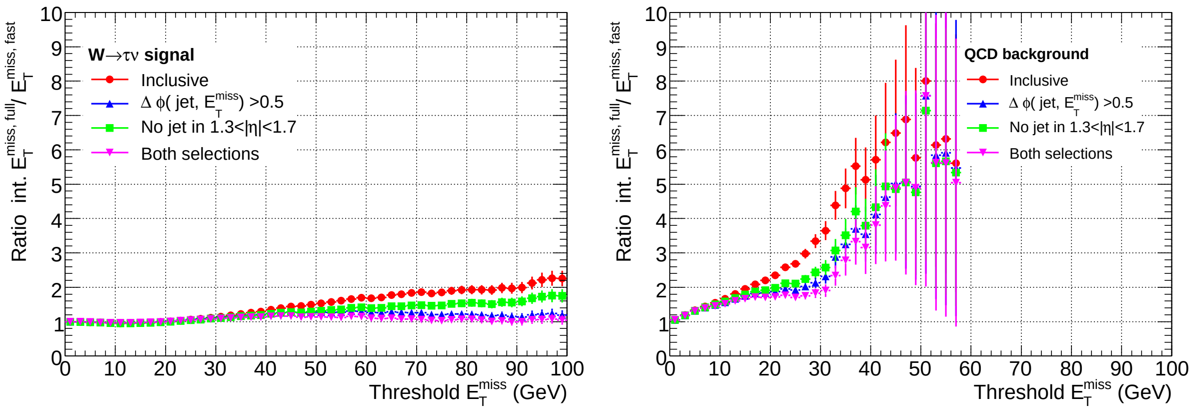

Figure 3.11: The ratio of the integrated cross-section as function of E_T^{Miss} threshold, from the full and fast simulation of the detector, for signal events (left) and for QCD background (right). The ratio is shown for inclusive cross-section and after excluding events with jets in the crack region or with E_T^{Miss} parallel to the jet direction (see text).

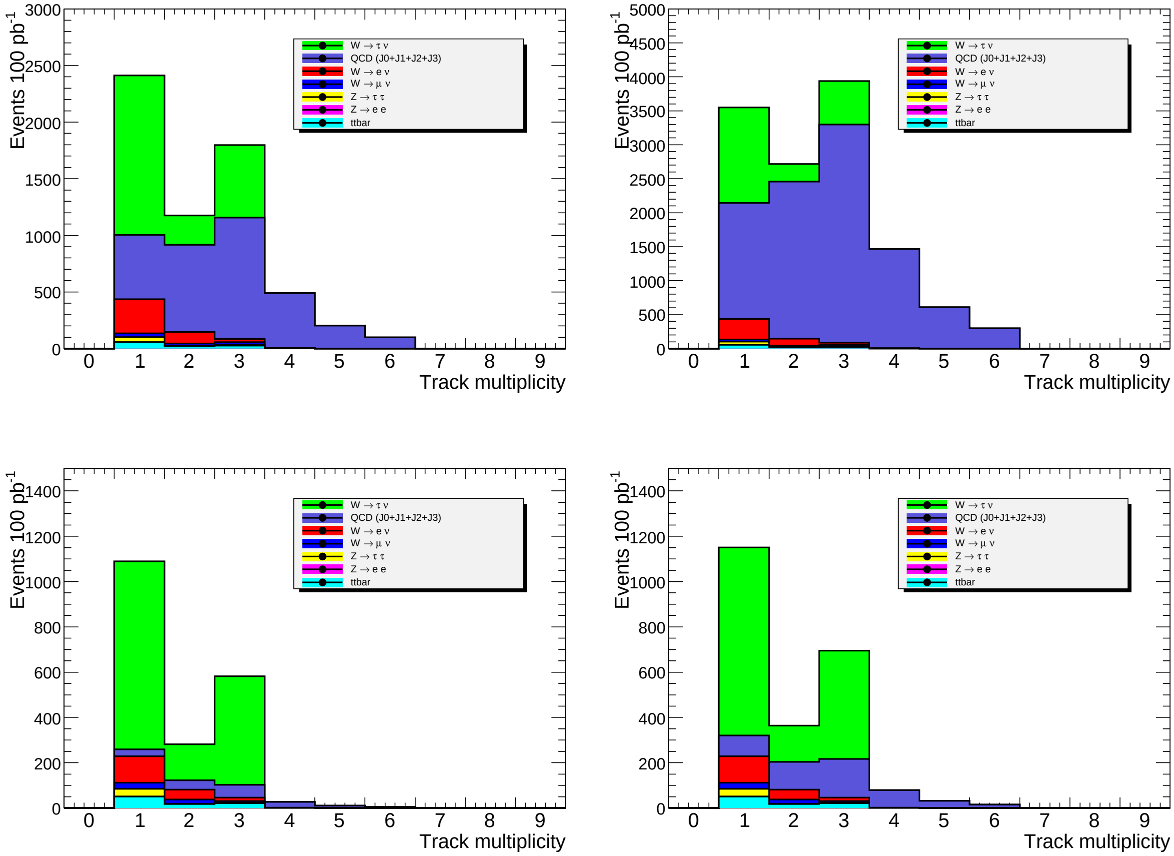

Figure 3.12: The track multiplicity spectra for signal and background events after the final selection described in Table 3.16, for $E_T^{Miss} > 50$ GeV (top) and $E_T^{Miss} > 60$ GeV (bottom). On the left side, for the QCD background, estimates from fast simulation are taken while on the right side results after rescaling the QCD background by a factor of 3 (representing cumulative corrections for trigger acceptance and slope of the offline E_T^{Miss} spectrum, see text) are shown.

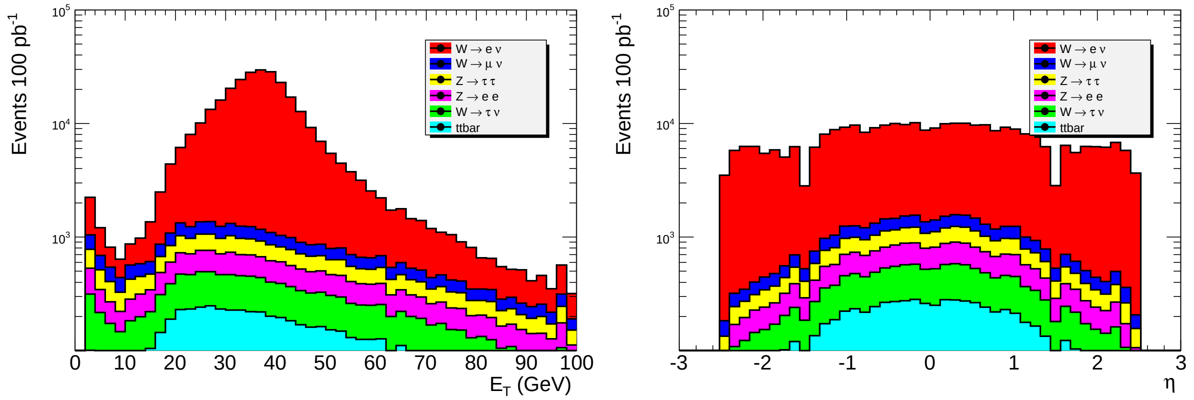

Figure 3.13: The transverse energy (left) and pseudorapidity (right) distributions for the *tight* electron in events flagged for the *Electron stream.*

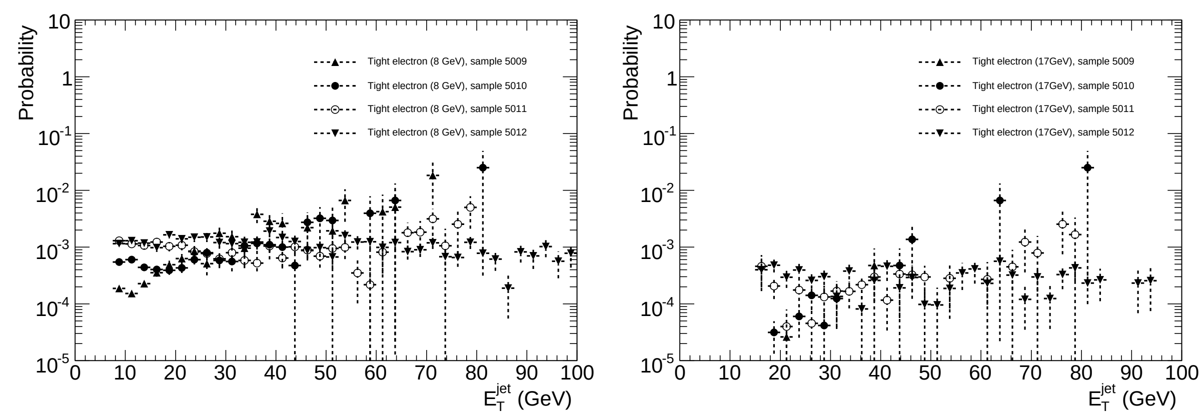

Figure 3.14: The efficiency to classify a jet as *Tight* electron as measured from the full simulation sample, as a function of the jet transverse energy, shown separately for different samples, for an electron threshold of $E_T > 8$ GeV (left) and $E_T > 17$ GeV (right).

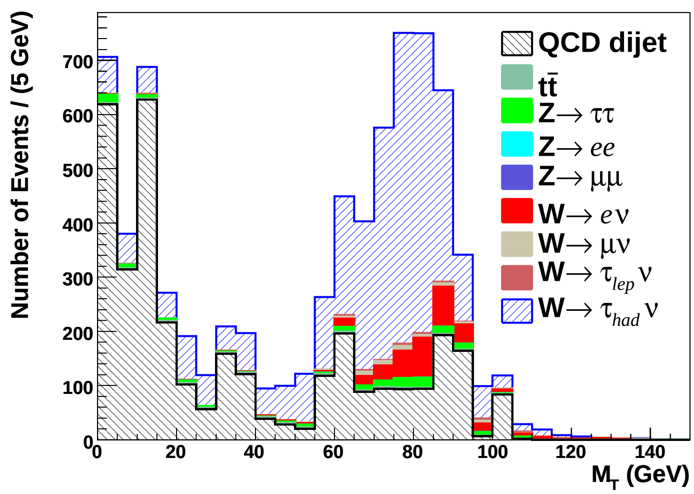

Figure 3.15: Transverse mass (m_T) distribution after full event selection, except the $\Delta\phi(\tau, E_T^{Miss}) > 2.5$ requirement. Distributions are normalized to integrated luminosity of 100 pb^{-1} [20].

Chapter 4

Summary

Two very fundamental analyses of Standard Model processes have been presented in this work, namely the measurement of $W \rightarrow e\nu$ cross-section and feasibility study of $W \rightarrow \tau\nu$ observation.

- The latter was prepared in early stage of doctoral studies' course and is based on simulated events only. At that time, the LHC running conditions, beam energies etc. were not known, i.e. 14 TeV and 10 TeV center-of-mass energies and 100 pb^{-1} of integrated luminosity was assumed.
- The former studies were performed with experimental data, based on 315 nb^{-1} collected in period between March and August 2010 at $\sqrt{s} = 7$ TeV. The data-based analysis was a part of the measurement published by ATLAS Collaboration.

4.1 $W \rightarrow e\nu$ cross-section measurement

A full analysis chain, leading to the measurement of the W-production cross-section times $W \rightarrow e\nu$ branching ratio, has been presented. This thesis presents results obtained by author himself, compatible with ATLAS published results, both in terms of central values and uncertainty estimations. The author has taken a very active part in preparation of the publication of ATLAS Collaboration results on $W \rightarrow e\nu$ cross-section in [17] in October 2010. This was the first measurement of W production cross-section at the LHC energies.

The result agrees well with theoretical predictions, its precision however does not provide new constraints on Parton Distribution Functions currently. The uncertainty is already dominated with systematics, however, a large decrease of systematic error is expected already with the full 2010 dataset of 45 pb^{-1}. This is due to employment of fully-data-driven techniques for energy-scale determination (Z-boson mass spectrum), lepton selection and trigger efficiency ($Z \rightarrow ee$ tag-and-probe methods) and better knowledge of the amount of dead material within the detector. An improvement in luminosity determination is also expected. Large statistics will also allow for differential cross-section estimation with respect to lepton transverse momentum and pseudorapidity.

4.2 $W \rightarrow \tau\nu$ observation feasibility

The analysis leading to signal extraction for $W \rightarrow \tau\nu$ process was performed with $\sqrt{s} = 14$ TeV Monte Carlo simulated samples in preparation for LHC start-up. Very tight cuts were needed to be applied, especially on the E_T^{Miss} value, do discriminate against huge QCD di-jet background, much more severe than in electron-channel analysis, due to jet-like nature of signal events (hadronic τ decays). It has been estimated, that, after the proposed selection, a clear excess of signal events above the background will be visible. The prepared selection was a baseline for further studies, with 10 TeV, in which the author has taken active part. Analysis strategies developed there led to the most recent data-based studies at 7 TeV and to the first observation of $W \rightarrow \tau\nu$ events, published as conference note of ATLAS Collaboration [18].

Bibliography

[1] G. Arnison et al. (UA1 Collaboration), *Experimental observation of isolated large transverse energy electrons with associated missing energy at* $\sqrt{s} = 540\ GeV$, Phys. Lett. **B122**, 103
M. Banner et al. (UA2 Collaboration, *Observation of single isolated electrons of high transverse momentum in events with missing transverse energy at the CERN* $p\bar{p}$ *Collider*, Phys. Lett. **B122**, 476
G. Arnison et al. (UA1 Collaboration), *Experimental observation of lepton pairs of invariant mass around* 95 GeV/c^2 *at the CERN SPS Collider*, Phys. Lett. **B126**, 398
P. Baganaia et al. (UA2 Collaboration), *Evidence for* $Z^0 \rightarrow e^+e^-$ *at the CERN* $p\bar{p}$ *Collider*, Phys. Lett. **B129**, 130

[2] C. Albajar et al. (UA1 Collaboration), *Intermediate Vector Boson Cross-sections at the CERN Super Proton Synchrotron Collider and the Number of Neutrino Types*, Phys. Lett. **B197** (1987) 271.
J. Alitti et al. (UA2 Collaboration), *A Measurement of the* W *and* Z *Production Cross-sections and a Determination of Gamma(W) at the CERN* $\bar{p}p$, Phys. Lett. **B276** (1992) 365

[3] ALEPH, DELPHI, L3 and OPAL Collaborations, *A Combination of Preliminary Electroweak Measurements and Constraints on the Standard Model*, arXiv:hep-ex/0112021v2

[4] A. Abulencia et al. (CDF Collaboration), *Measurement of inclusive* W *and* Z *cross sections in* $p\bar{p}$ *collisions at* $\sqrt{s} = 1.96\ TeV$, J. Phys. G: Nucl. Part. Phys. **34** (2007) 2457-2544

[5] B. Abbott et al. (D0 Collaboration), *Measurement of* W *and* Z *boson production cross sections*, Phys. Rev. **D60**:052003, 1999, arXiv:hep-ex/9901040v1

[6] K. Melnikov, F. Petriello, *Electroweak gauge boson production at hadron colliders through* $\mathcal{O}(\alpha_S^2)$

[7] A. Martin, R. Roberts, J. Stirling, R. Thorne, *Parton Distributions and the LHC: W and Z Production*, arXiv:hep-ph/9907231v1

[8] J. Lykken, *Beyond the Standard Model* in *2009 European School of High-energy Physics*, CERN-2010-002, arXiv:1012.4643

[9] O. Bruning et al. *LHC Design Report*, CERN-2004-003-V-1

[10] ATLAS Collaboration, *The ATLAS Experiment at the CERN Large Hadron Collider*, JINST **3**, S08003 (2008).

[11] S. Glashow, *Partial-symmetries of weak interactions*, Nucl. Phys. **22** (1961) 579-599
S. Weinberg, *A model of leptons*, Phys. Rev. Lett. **19** 1264 (1967)
A. Salam, *Gauge unification of fundamental forces*, Nobel lecture, 8 Dec 1979

[12] P. Higgs, *Broken symmetries and the masses of gauge bosons*, Phys. Rev. Lett. **13**, 508
F. Englert, R. Brout, *Broken symmetry and the mass of gauge vector mesons*, Phys. Rev. Lett. **13**, 321

[13] D. Perkins, *Introduction to High Energy Physics*, 4th edition (2009) F. Halzen, A. Martin, *Quarks and leptons. An Introductionary Course in Modern Particle Physics*, 1984

[14] K. Nakamura et al. (Particle Data Group), *Review of Particle Physics 2010* J. Phys. G 37, 075021 (2010)

[15] S. Frixione, M. Mangano, *How accurately can we measure the W cross section?*, JHEP05(2004)056

[16] ATLAS Collaboration, *Measurement of theW Boson Mass with Early Data*, in [59].

[17] The ATLAS Collaboration, *Measurement of the* $W \to \ell\nu$ *and* $Z/\gamma* \to \ell\ell$ *production cross sections in proton-proton collisions at* $\sqrt(s) = 7$ *TeV with the ATLAS detector*, CERN-PH-EP-2010-037, arXiv:1010.2130v1 [hep-ex]

[18] ATLAS Collaboration, *Observation of* $W \to \tau\nu$ *Decays with the ATLAS Experiment*, ATLAS-CONF-2010-097

[19] Y. Coadou, Pa. Malecki, E. Richter-Was, *Prospects for physics measurements with the* $W \to \tau\nu$ *process for 100* pb^{-1} *with the ATLAS detector*, ATL-PHYS-INT-2009-011 ; ATL-COM-PHYS-2008-112.

[20] G. Nunes Hanninger et al. (Pa. Malecki), *Prospects for Studying* $W \to \tau\nu$ *Decays with ATLAS Data Corresponding to an Integrated Luminosity of 100* pb^{-1}, ATL-COM-PHYS-2010-067

[21] A. Ahmad et al. (Pa. Malecki), *W to e nu and Z to ee Observations supporting note*, ATL-COM-PHYS-2010-297

[22] M. Aharrouche et al. (Pa. Malecki), *Wenu and Zee observations supporting note*, ATL-COM-PHYS-2010-472

[23] M. Aharrouche et al. (Pa. Malecki), *Supporting note for the measurement of the production cross-section of Wenu and Zee at sqrt(s) = 7 TeV with the ATLAS detector*, ATL-COM-PHYS-2010-539

[24] A. Belloni et al. (Pa. Malecki), *Measurement of W->lnu charge asymmetry in proton-proton collisions at sqrt(s)=7TeV with the ATLAS detector*, ATL-COM-PHYS-2010-696

[25] M. Aharrouche et al. (Pa. Malecki), *W->enu and Z->ee cross-section measurements in proton-proton collisions at sqrts=7 TeV with the ATLAS Detector : Support note to publication.*, ATL-COM-PHYS-2010-701

[26] Pa. Malecki, *First results from ATLAS experiment on production of W and Z bosons in proton-proton collisions at* $\sqrt{s} = 7$ *TeV*, To appear in APPB

[27] ATLAS Collaboration, *Expected Performance of the ATLAS Experiment, Detector, Trigger and Physics*, CERN-OPEN-2008-020 (2008), arXiv:0901.0512v4 [hep-ex].

[28] A. Kaczmarska, Pa. Malecki, T. Szymocha, *The ATLAS experiment simulations as the computing challenge for the ACK CYFRONET AGH*, Computing and Informatics, vol. 9 2008, 47-54

[29] The ATLAS Collaboration, *Luminosity Determination Using the ATLAS Detector*, ATLAS conference note: ATLAS-CONF-2010-060.

[30] The GEANT4 Collaboration, S. Agostinelli et al., *GEANT4: A simulation toolkit*, 964 Nucl. Instrum. Meth. **A506** (2003) 250.

[31] The ATLAS Collaboration, *The ATLAS Simulation Infrastructure*, `arXiv:1005.4568 [physics.ins-det]`.

[32] T. Sjostrand, S. Mrenna and P. Skands, *PYTHIA 6.4 physics and manual* JHEP05 (2006) 026. Versions used detailed in [47].

[33] S. Frixione, P. Nason and B.R. Webber, *Matching NLO QCD and parton showers in heavy flavour production*, JHEP 0308 (2003) 007. Versions used detailed in [47].

[34] The ATLAS Collaboration, *Electron and photon reconstruction and identification in ATLAS: expected performance at high energy and results at* $\sqrt{s} = 900$ GeV, ATLAS conference note: ATLAS-CONF-2010-005.

[35] The ATLAS Collaboration *Charged-particle multiplicities in pp interactions at* $\sqrt{s} = 900$ *GeV measured with the ATLAS detector at the LHC*, Phys. Lett **B688** (2010) 21-42.

[36] W. Lampl et al. *Calorimeter clustering algorithms : Description and performance.* ATL-LARG-PUB-2008-002.

[37] T. Barillari et al. *Local hadron calibration.* ATL-LARG-PUB-2009-001, 2009.

[38] ATLAS Collaboration *Charged particle multiplicities in pp interactions at* $\sqrt{s} = 900 GeV$ *measured with the ATLAS detector at the LHC*, Phys. Lett. **B688** (2010) 21-42.

[39] The ATLAS Collaboration, G. Aad et al., *Performance of the ATLAS electromagnetic calorimeter for* $\pi^0 \rightarrow \gamma\gamma$ *and* $\eta \rightarrow \gamma\gamma$ *events*, ATLAS conference note: ATLAS-CONF-2010-006.

[40] The ATLAS Collaboration, *Measurement of the W->lnu production cross-section and observation of Z -> ll production in proton-proton collisions at roots=7 TeV with the ATLAS detector*, ATLAS-CONF-2010-051;

The ATLAS Collaboration, *Performance of the Missing Transverse Energy Reconstruction and Calibration in Proton-Proton Collisions at a Center-of-Mass Energy of* $\sqrt{s} = 7$ *TeV with the ATLAS Detector*, ATLAS-CONF-2010-057

[41] P. M. Nadolsky et al., *Implications of CTEQ global analysis for collider observables*, Phys. Rev. **D78** (2008) 013004, arxiv:0802.0007 [hep-ph]

[42] H1, ZEUS Collaborations, *Combined Measurement and QCD Analysis of the Inclusive ep Scattering Cross Sections at HERA*, JHEP **01** (2010) 109, arxiv:0911.0884 [hep-ex]

[43] PHENIX Collaboration, A. Adare et al., *Cross Section and Parity Violating Spin Asymmetries of* $W^{\pm}$ *Boson Production in Polarized* $p+p$ *Collisions at* $\sqrt{(s)} = 500GeV$, `arxiv:1009.0505 [hep-ex]`.

[44] CDF Collaboration, *Measurement of the* $B(W \to \tau\nu\ )/B(W \to e\nu\ )$ *in* $p\bar{p}$ *collisions at* $\sqrt{s} = 7$ *TeV* Phys. Rev. Lett. 68 (1992) 3398

[45] D0 Collaboration, *Measurement of the* $W \to \tau\nu$ *Production Cross Section in* $p\bar{p}$ *Collisions at* $\sqrt{s} = 1.8$ *TeV*, Phys. Rev. Lett. 84 (2000) 5710

[46] A. Safonov (CDF Collaboration), *Physics with taus at CDF*, Nucl. Phys. Proc. Suppl. **144**, 323 (2005).

[47] ATLAS Collaboration, *Monte Carlo Generators for the ATLAS Computing System Commissioning*, in [59].

[48] ATLAS Collaboration, *Reconstruction and Identification of Electrons in ATLAS*, in [59].

[49] ATLAS Collaboration, *Reconstruction and Identification of Muons in ATLAS*, in [59].

[50] ATLAS Collaboration, *Reconstruction and Identification of Hadronic* τ *Decays in ATLAS* , in [59].

[51] B. Salvachua et al., *Comparison of MC based Jet Energy Scales applied after H1 calibration*, Tech. Rep. ATL-COM-PHYS-2009-162.

[52] ATLAS Collaboration, *Reconstruction and Identification of Jets in ATLAS* , in [59].

[53] ATLAS Collaboration, *Measurement of Missing Transverse Energy in ATLAS*, in [59].

[54] Z. Czyczula and M. Dam, *Electron veto in the tau identification package Tau1P3P*, ATLAS Physics Internal Note, ATL-PHYS-INT-2008-003.

[55] Z. Czyczula, *Cut based electron veto for track seeded taus*, presented at the ATLAS Tau Workshop, Dresden, 15 May 2008.

[56] ATLAS Collaboration, *ATLAS Tau Trigger: Performance and Menus for Early Running*, in [59].

[57] D. Cavalli et al., *Performance of the ATLAS fast simulation ATLFAST*, Atlas Physics Internal Note, ATL-PHYS-INT-2007-005.

[58] P. Bechtle et al. *Identification of hadronic tau decays with ATLAS detector* ATL-PHYS-INT-2008-003

[59] ATLAS Collaboration, *Expected Performance of the ATLAS Experiment, Detector, Trigger and Physics*, CERN-OPEN-2008-020 (2008).

[60] B. G. Petersen, M. Pohl "The cosmic ray induced muon spectrum measured with the L_3 detector" CERN-THESIS-2002-033

[61] MINOS Collaboration "Measurement of the Atmospheric Muon Charge Ratio at TeV Energies with MINOS" arXiv:0705.3815v4 [hep-ex]

[62] B. Heinemann et al., *A measurement of the cosmic muon charge ratio*, ATL-COM-PHYS-2010-135, unpublished

[63] V. Blobel, *An Unfolding Method for High Energy Physics Experiment*, arXiv:hep-ex/0208022v1

[64] G. D'Agostini, *Improved iterative Bayesian unfolding*, arXiv:1010.0632v1 [physics.data-an]

[65] `http://hepunx.rl.ac.uk/ adye/software/unfold/RooUnfold.html` - RooUnfold website.

Appendix A

Fake E_T^{Miss} studies

As mentioned earlier in Chapter 3, a huge discrepancy is found between the fast and full simulation samples in events with fake E_T^{Miss} , namely the QCD dijets. We will try to study the roots of this discrepancy in more detail here.

A preselection step requires E_T^{Miss} to be above 40 GeV in each event. This does reduce the available statistics greatly, as can be seen in Table A.1. Only 154 events remain after

Process	All QCD	8-17 GeV	17-35 GeV	35-70 GeV	70-140 GeV
Statistics		154	90	3282	5762
Events in 100 pb^{-1}	$1.63 \cdot 10^8$	$1.17 \cdot 10^8$	$3.23 \cdot 10^7$	$1.14 \cdot 10^7$	$3.05 \cdot 10^6$
Fraction of total		71%	20%	7%	2%

Table A.1: Content of the QCD samples with full simulation $E_T^{Miss} > 40$ GeV.

selection in the lowest p_T sample, which in turn is the most dominant. Several potential sources of the investigated discrepancies are checked.

The full and fast simulation samples contain truth information from the Monte Carlo generator, that allows us to compare the fast and full simulation on an event-by-event basis. Most events contain no true E_T^{Miss} .

One of the possible reasons of the E_T^{Miss} discrepancy under investigation is the problem with event generation, i.e. wrong hard scatter parameters. This hypothesis is based on the fact, that it is not expected to be likely, that events with $p_T^{hard} < 17$ GeV will have E_T^{Miss} at the level of 40 GeV or above. Figure A.1 shows the distributions of transverse momentum of most-energetic parton in all events (left column) and in events with $E_T^{Miss} > 40$ GeV (right column). In the latter sample the parton has slightly higher transverse momentum, but it is still close to the generated range. No obvious problem at generator level is therefore observed.

The gaussian part of the E_T^{Miss} event contribution is expected to be well reconstructed by `ATLFAST I`. This has been checked and confirmed, see Fig. A.2. The discrepancy is therefore a result of fake E_T^{Miss} contribution from fully simulated samples.

The mis-reconstructed muons were checked not to contribute significantly to the observed discrepancy.

As already shown in Section 3.7.2 and in Figure 3.11, removing events with jets pointing to the calorimeter crack region, $1.3 < |\eta| < 1.7$, does reduce the rate of fake E_T^{Miss} events,

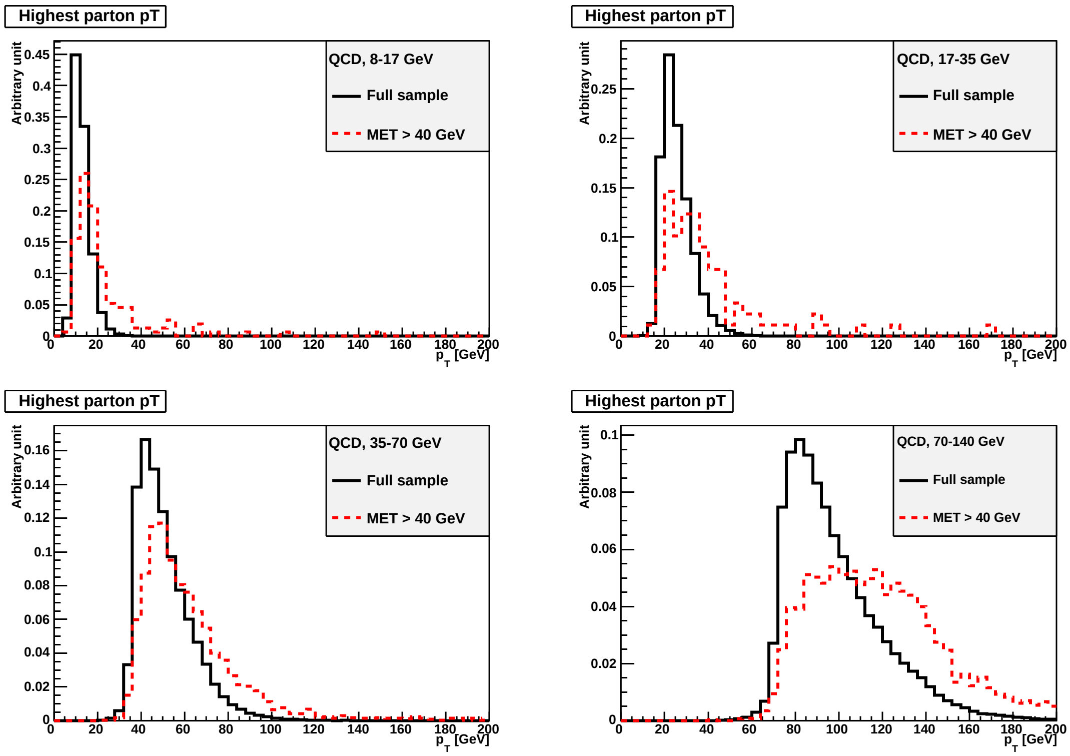

Figure A.1: p_T of the most energetic parton, in all events and in events with $E_T^{Miss} > 40$ GeV, for all QCD samples. Histograms are normalised to unit area.

as well as vetoing events with E_T^{Miss} pointing in the same direction as reconstructed jet. There is another correlation - average jet multiplicity is higher in events with fake E_T^{Miss} . However, as can be seen in Table A.2, this is not very discriminating cut after two previous cuts for fake E_T^{Miss} removal.

Another possible way of suppressing more fake E_T^{Miss} events is based on using tracks to confirm calorimeter clusters reconstructed as jets. This method is only applicable in the region of tracking acceptance, $|\eta| < 2.5$. We were looking for tracks in each jet, with $\chi^2/NDF < 3$ and $p_T > 500$ MeV within $\Delta R < 0.4$ from the centre of jet. Track with highest (leading) p_T associated with jet defines jet charge. It turns out, that there is a particular set of jets with no associated track. They do generate fake E_T^{Miss} , as can be seen in fig A.3.

This plot, similar to Fig. 3.11, includes the removal of no-track jets from the sample. This correction, combined with the other two ways of vetoing events with fake E_T^{Miss} reduces the ratio down to about 2 at 40 GeV of E_T^{Miss} . The ratio seems to be stable above that value. As shown in Table A.3, it has hardly any impact on the signal process and rejects 34% of J0 sample and some number of other dijets thus improving the signal to background ratio.

These no-track-jet events, that were rejected, were further studied in more detail in order to determine their origin. Their (fake) E_T^{Miss} from full simulation is harder than the one of other jets, while their E_T^{Miss} spectrum from `ATLFAST I` is softer, closer to true value of 0. This is shown in fig A.4.

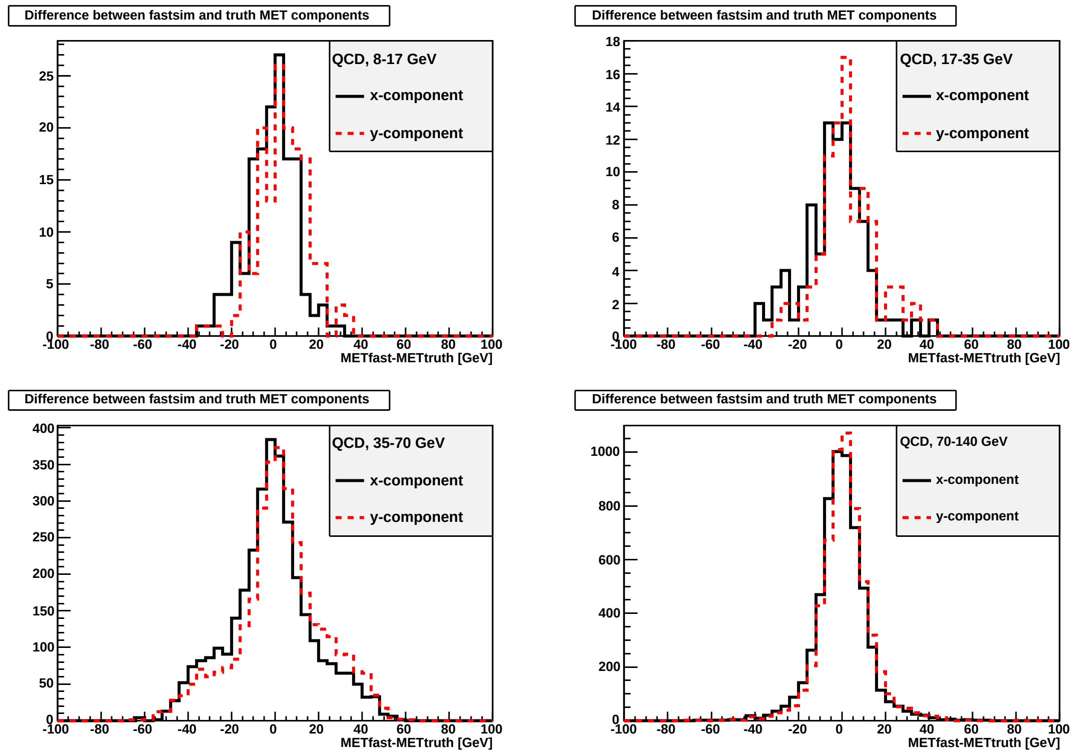

Figure A.2: Difference between Atlfast E_T^{Miss} and truth E_T^{Miss} x and y components in events with $E_T^{Miss} > 40$ GeV, for all QCD samples.

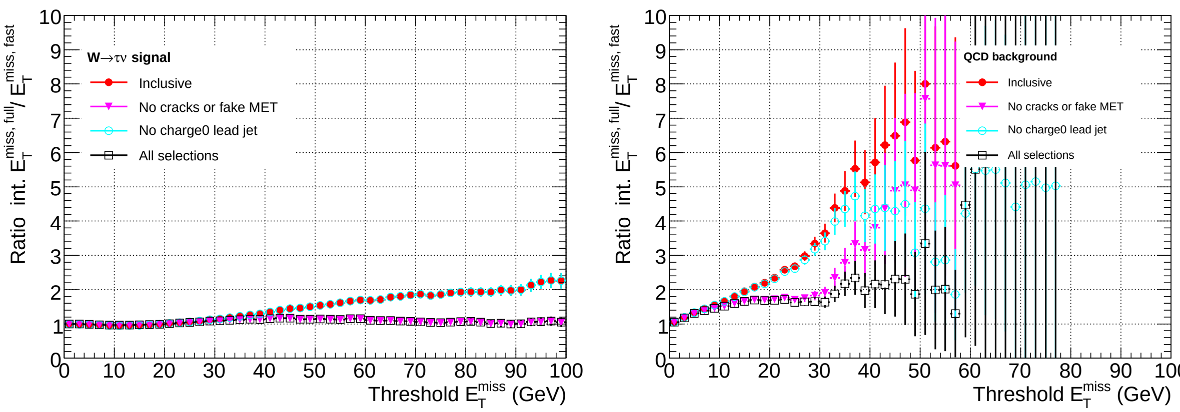

Figure A.3: The ratio of the integrated cross-section as a function of the E_T^{Miss} threshold, from the full and fast simulation of the detector, for signal events (left) and for QCD background (right). The ratio is shown for the inclusive cross-section, after excluding events with jets in the crack region or with E_T^{Miss} parallel to the jet direction, and after removing events with a leading jet not associated to any track (see text).

	$W \rightarrow \tau\nu$	8-17 GeV	17-35 GeV	35-70 GeV	70-140 GeV
	jet $p_T > 15$ GeV				
Multiplicity	2.5	5.4	4.9	3.6	4.4
Multiplicity after fake E_T^{Miss} removal	2.1	2.9	2.8	2.3	3.9
	jet $p_T > 20$ GeV				
Multiplicity	1.8	4.0	3.4	2.7	3.6
Multiplicity after fake E_T^{Miss} removal	1.5	1.9	2.0	1.8	3.2

Table A.2: Jet multiplicity in the $W \rightarrow \tau\nu$ events and QCD samples with full simulation $E_T^{Miss} > 40$ GeV, for jets with $p_T > 15$ GeV and $p_T > 20$ GeV. Multiplicities are also given after applying the fake E_T^{Miss} cuts (see text).

Statistics	$W \rightarrow \tau\nu$	8-17 GeV	17-35 GeV	35-70 GeV	70-140 GeV
$E_T^{Miss} > 40$ GeV	7957	154	90	3282	5762
Fake/crack removal	5769 (72%)	85 (55%)	45 (50%)	1804 (55%)	1023 (18%)
No 0-charge lead jet	5749 (99.7%)	56 (66%)	36 (80%)	1735 (96%)	1014 (99%)

Table A.3: Impact of fake E_T^{Miss} removal cuts in the $W \rightarrow \tau\nu$ events and QCD samples with full simulation $E_T^{Miss} > 40$ GeV. Relative efficiencies are given in parenthesis.

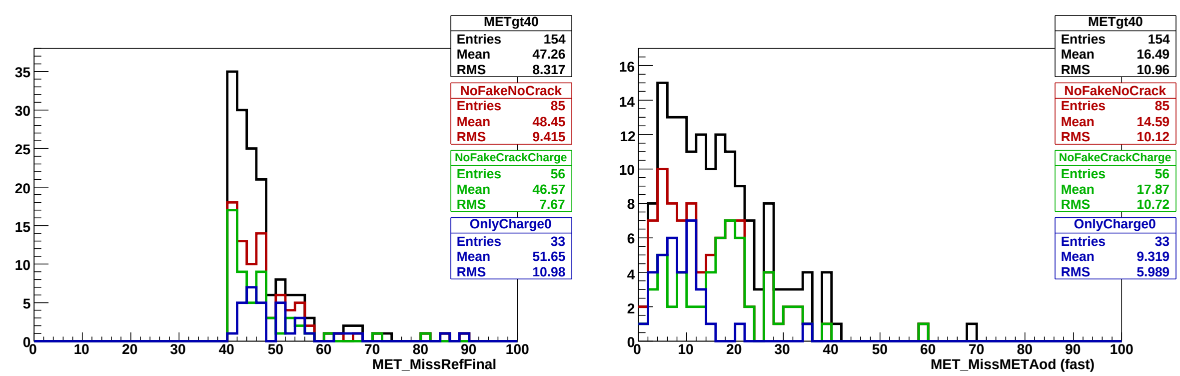

Figure A.4: E_T^{Miss} full (left) and fast simulation (right) spectra for J0 events with full simulation $E_T^{Miss} > 40$ GeV. Black: all events; red: after excluding events with jets in the crack region or with $|\Delta\phi(E_T^{Miss}, jet)| < 0.5$; green: after also removing events with the leading jet not associated to any track (see text); blue: only events with no track associated to the leading jet.

The jet multiplicity from those events (with jet $p_T > 15$ GeV) is low and close to 1, whereas for a typical QCD event with fake E_T^{Miss} above 40 GeV the jet multiplicity is close to 5, or 3 after the first two cuts for fake E_T^{Miss} removal. This is shown on the left plot in

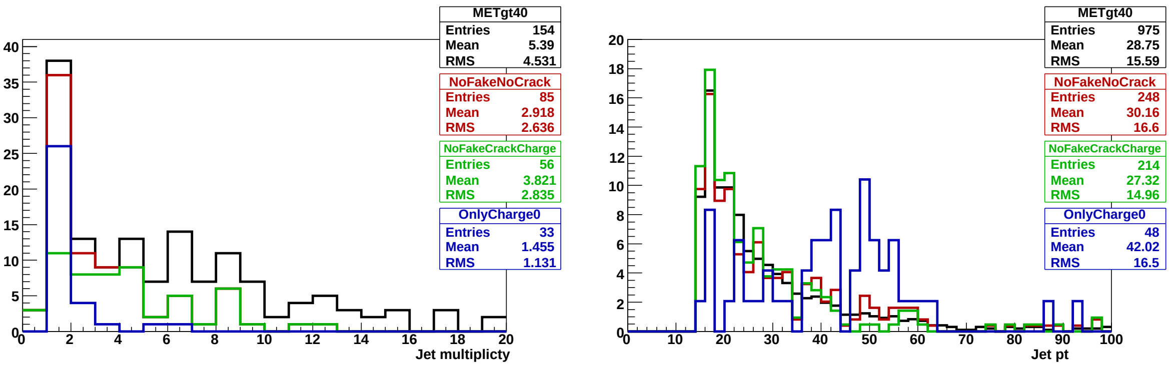

Figure A.5: Jet multiplicity for jets with $p_T > 15$ GeV (left) and normalised jet p_T spectra (right) for J0 events with full simulation $E_T^{Miss} > 40$ GeV. Black: all events; red: after excluding events with jets in the crack region or with $|\Delta\phi(E_T^{Miss}, jet)| < 0.5$; green: after also removing events with the leading jet not associated to any track (see text); blue: only events with no track associated to the leading jet.

Figure A.5. The transverse momentum of the leading parton in the no-track jets is lower (around 16 GeV) than the average leading parton p_T in the events with $E_T^{Miss} > 40$ GeV (around 23 GeV). The p_T spectrum of jets in such events is relatively hard, as be seen in Fig. A.5 (right). No obvious hot region of the calorimeter is observed, so this is not the reason for the discrepancy.

After a separate look at each E_T^{Miss} component, already a E_T^{Miss} of 30 GeV can be observed, counting only the cells with $|E| > 2\sigma$ (noise), before any calibration. The direction of the E_T^{Miss} is mostly back-to-back with the direction of the leading jet (usually the only one in the event as said before). This jet does not match any true or `ATLFAST I` jet, as no such objects with $p_T > 15$ GeV are usually present.

Appendix B

Unfolding of cosmic muon momentum spectrum

The performance of the Inner Detector was crucial for all analyses presented in this thesis. Prior to the start of collisions in LHC, the only possible source to study a real detector performance was to exploit the existence of cosmic rays penetrating the ATLAS experimental setup. In addition, unfolding techniques applied here are commonly used in modern data analyses and are important to be understood, as they may provide results independent of detector conditions and easily comparable with other experiments.

This part of author's work was conducted in 2009, before the winter re-start of the LHC. The analysis was prepared with cosmic data collected in Summer of 2009 with full Inner Detector turned on. The aim was to perform first measurement of cosmic muon charge ratio between 400 GeV and 1 TeV of transverse momentum region, significantly contributing to world's average. However, it turned out, that both the systematic and statistical uncertainties, which could be reached, are larger than the previously published measurements, so this measurement was never published.

Author's work in that analysis was limited to obtaining detector-unfolded muon p_T spectrum. The resulting corrections, needed to be applied to the spectrum directly measured were however small, and well below the sensitivity of this analysis, due to huge uncertainties from other sources, mostly from detector misalignment influence on momentum measurement. Also, the available data statistics did not allow for a measurement precise enough to provide a contribution to previous results from other experiments.

This Section outlines the method and results of measuring the cosmic muon charge spectrum and describes the method of estimating detector influence with unfolding. This second point represents author's own work.

B.1 Introduction to charge-ratio analysis

The analysis of cosmic muon charge-ratio has been documented in [62]. This Section outlines its main aspects.

Motivation and general remarks The measurement of cosmic ray-induced muon charge ratio (of the number of positive to negative muons) at the earth surface was already performed by several experiments, including L3-Cosmics [60] (below 400 GeV) and

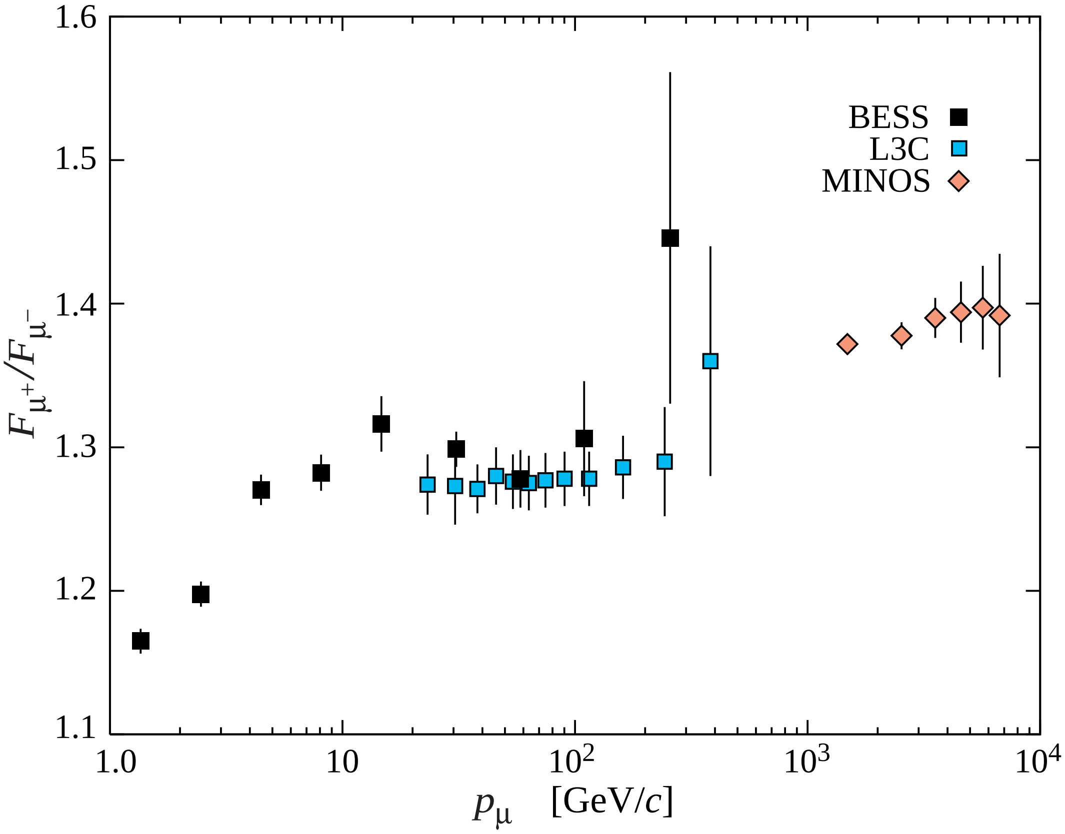

Figure B.1: World results of muon charge ratio spectrum measurement at the surface of the earth[14]

MINOS[61] (above 1 TeV). The combined results are shown in Fig. B.1. Quite surprising is the fact, that there is a gap in measurements between 400 GeV and 1 TeV. In this region the charge ratio is expected to change from around 1.3 to 1.4. In this particular area it is expected, that the ATLAS detector could provide a competitive measurement. This is because of its large size and high precision of measurement.

The muons arriving at the underground ATLAS cavern originate from the upper layers of atmosphere, where the primary cosmic ray particles (mostly protons) interact with atmosphere nuclei and produce a cascade of particles. The muons are produced in the decays of secondary particles - K and π mesons:

$$K^+/\pi^+ \to \mu^+\nu_\mu, \quad \mu^+ \to e^+\nu_e\bar{\nu}_\mu, \tag{B.1}$$

$$K^-/\pi^- \to \mu^-\bar{\nu}_\mu, \quad \mu^- \to e^-\bar{\nu}_e\nu_\mu. \tag{B.2}$$

The measured muon charge ratio is directly related to the meson ratio, which in turn is sensitive to the primary cosmic rays composition and the interaction model of particles in the atmosphere. For instance, the fraction of positive kaons may be different than that of pions, as the $K^+(\bar{s}u)$ meson is produced together with $\Lambda(sdu)$, whereas the $K^-(s\bar{u})$ is not.

Besides, there is also a direct coupling of muon and neutrino fluxes, so this may be an important contribution to the atmospheric neutrino measurements.

The muon charge ratio measured with the ATLAS detector (100m underground) may in principle differ from the actual charge ratio at the surface, due to a number of effects, which include:

- Mis-measurement of track parameters (p_T, θ, ϕ, d_0, z_0) which happens because of misalignments or incorrect magnetic field estimations. It may affect charge ratio measurement by biasing the curvature $1/p_T$ or azimuthal angle θ results.

- Charge-dependent detector performance and acceptance - the incident muons take different trajectories, depending on their charge and momentum. The detector regions traversed by differently charged muons may have different momentum resolutions and also different efficiencies.

- Energy losses - a typical cosmic muon losses approximately 30 GeV while passing through the 100 m of rock above ATLAS. Still, if a muon passes through one of the service shafts, its energy losses are negligible (several MeV). Therefore - number of muons varies at different detector areas and so does their momentum.

The possible biases are measured and corrected for in the course of this analysis. The steps listed below are also a general outline of this work.

1. The only part of ATLAS used to reconstruct tracks for this analysis is the Inner Detector. The reconstructed tracks are divided into two disjoint categories: pixel and non-pixel tracks. The biasing effects have been separately measured and corrected for in each category separately.

2. A fiducial region of the detector with the same acceptance for positive and negative tracks is created.

3. The trigger and tracking efficiencies, together with track parameter resolution and bias are measured versus momentum and charge.

4. An apparent charge ratio versus measured momentum at the perigee point needs to be corrected for any systematic effect found in the above. For each correction we estimate the systematic uncertainty.

5. The resulting charge ratio spectrum is then corrected for any bin migration effects caused by finite detector resolution. After those correction we obtain a spectrum versus the actual momentum (see Section B.2).

6. The spectrum is obtained with respect to actual momentum in the middle of ATLAS, 100 m underground. It is needed to correct the spectrum for the energy losses in the region above ATLAS.

Acceptance Due to non-uniform distribution of material above the detector and the presence of toroidal magnetic field, the overall acceptance differs for positive and negative muons. Therefore, a fiducial region of detector was defined, with charge-independent acceptance. A measured track of a certain charge is extrapolated up to the top of ATLAS detector, its charge is flipped and the track is then extrapolated back to the perigee. If it still passes basic selection criteria, the primary track is accepted for further analysis.

Trigger and tracking performance In this analysis, a TRT-based trigger was used. Its performance was measured with reference trigger based on RPC's of ATLAS Muon System. No trigger bias on charge ratio estimation was found, and a conservative systematics of 1% is assigned.

Tracking performance has also been found to be charge-independent. Both the pattern recognition procedure and application of selection cuts have proven to be consistent with no charge bias. Again, a 1% systematic uncertainty is assigned here.

Charge mis-measurement, parameter resolutions and bias The percentage of tracks with wrongly reconstructed charge was estimated with so-called half-track method. A muon track is cut into two parts, with hits above ($y > 0$) and below ($y < 0$) detector center. Each half is then re-fitted, and fractions of same-sign and opposite-sign events are calculated. This is done in bins of transverse momentum, estimating a correction factor for each bin, which would be later applied to the spectrum of charge ratio. It has been found, that for non-pixel tracks the deviation of correction factor from 1.0 is well below statistical error of measurement in each bin. For pixel tracks the opposite-sign fraction was found to be 0.0, so no correction factor was applied.

Resolution and bias on track parameters were also measured with half-tracks, by comparing differences between parameters in bins of transverse momentum. In each bin there was a histogram created for each parameter, and differences between upper and lower half-tracks were histogrammed. A gaussian curve was then fitted, obtaining bias (as mean value) and resolution (as gaussian σ). The most significant result from these studies shows, that there is an apparent charge-dependent bias on curvature measurement, due to Inner Detector misalignments.

The impact on charge ratio transverse momentum spectrum was estimated by generating a Monte Carlo sample of cosmic muon tracks. The charge ratio was rising monotonically from 1.24 at $p_T = 10$ GeV up to 1.4 at 2 TeV. The momentum spectrum was generated with PDG formula [14]. Influence of parameter resolutions and biases was assessed by smearing the generated track parameters with random gaussian resolution term and fixed bias term. Small effects are observed up to p_T of 75 GeV, whereas at higher momenta these effects become more significant reaching 3% at 300 GeV, 6% at 600 GeV and above 20% above 1 TeV. These effects are well above correction factors obtained with unfolding procedure described in next Section.

B.2 Transverse momentum unfolding

The spectrum of transverse momentum of cosmic muons measured in the ATLAS detector is strongly affected by systematic effects, namely the finite detector resolution, bias on measured parameters and overall momentum scale. We have to correct the measured spectrum for those effects in order to obtain the spectrum versus actual momentum of incoming muons, to be able to compare our results with other experiments and provide detector-independent result.

We therefore need to assess the possible influence of the detector resolution on the measured spectrum. The procedure involves using the Monte Carlo simulated samples, resolutions measured with the real data and unfolding techniques. The following steps are taken to estimate the possible biases and obtain correction factors:

- start with the true p_T distribution - let us call it p_T^{truth};

- apply gaussian smearing based on measured resolution functions to p_T^{truth} to determine full detector influence - $p_T^{sm,data}$.;
- at each level one can fill the Resolution Matrix, which is an estimate of detector effects, but also provides a direct input to unfolding algorithms;
- train the unfolding algorithms with p_T^{truth} (as the "truth" input) and consequently with $p_T^{sm,data}$. Resolution Matrices will be obtained this way, they will be then applied to unfolding of the proper spectra;
- apply the unfolding to the p_T spectrum obtained with Monte Carlo based reconstructed variables, as a cross-check;
- apply the unfolding to the p_T spectrum reconstructed from real data.

Curvature resolution was measured with half-track method, described in earlier Sections. Using the error propagation formula we can easily obtain the functional form of σ_{p_T} vs p_T which will then be used for smearing. The resolution function becomes: $\sigma_{p_T}(p_T) = \sigma_\infty p_T \sqrt{p_T^2 + p_X^2}$, where σ_∞ and p_X are free parameters and are obtained from fits to data.

Resolution smearing The p_T^{truth} Monte Carlo spectra may, in principle, be far from the real true spectra. But the point of our interest in this case is the influence of detector effects on them and the possible bias on the positive to negative muon ratio. These effects can be seen in Figure B.2, where the ratios of smeared to truth p_T are shown for pixel (left) and non-pixel(right) tracks, separately for each charge sign.

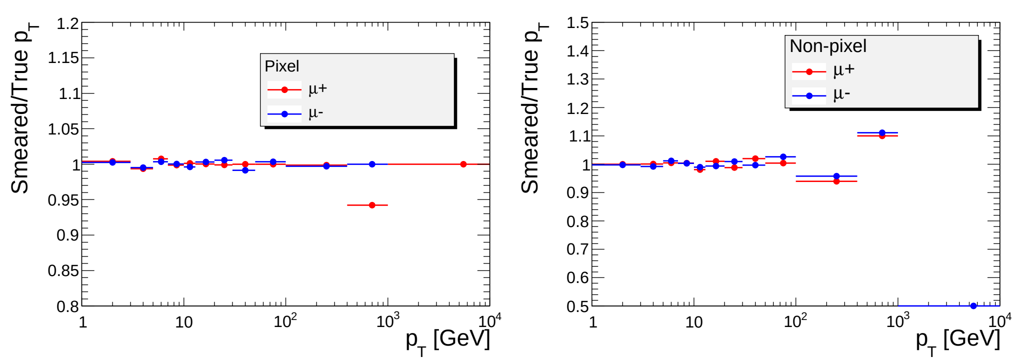

(a) Pixel tracks (b) Non-pixel tracks

Figure B.2: Ratios of smeared to true p_T spectra

As can be seen from Fig. B.2 the discrepancies between smeared and true spectra are larger for tracks without pixel hits below 400 GeV. Pixel tracks show much smaller charge dependence (much less than 1%), however it is still noticeable. The discrepancy seen in 0.4 - 1 TeV bin is probably the result of low statistics.

Resolution matrices Using the Monte Carlo events we can now fill the resolution matrices. They may be thought of as 2-dimensional histograms of p_T^{truth} vs $p_T^{smeared}$. Filling of these matrices according to the procedure described above can be considered as the training of an unfolding algorithm, that will then be applied to the measured spectra.

The resolution matrices obtained are shown in Fig. B.3.

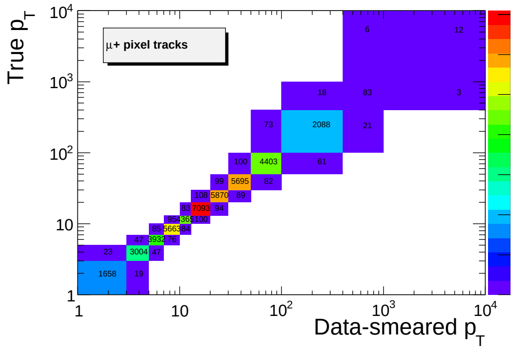

(a) Data $\mu+$ pixel

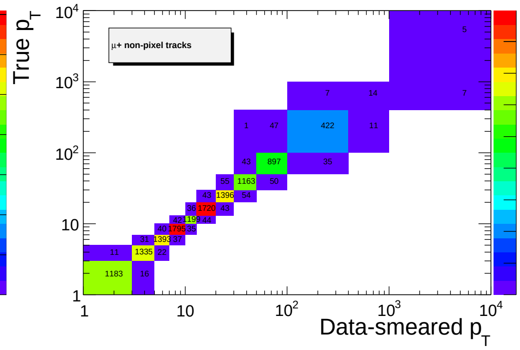

(b) Data $\mu+$ non-pixel

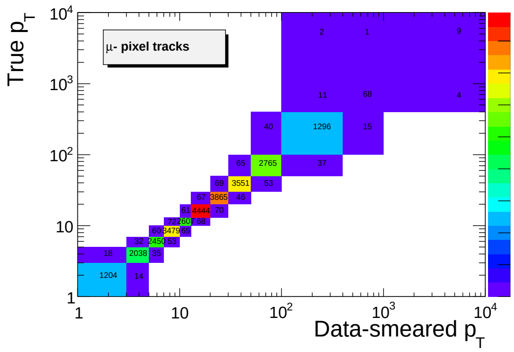

(c) Data $\mu-$ pixel

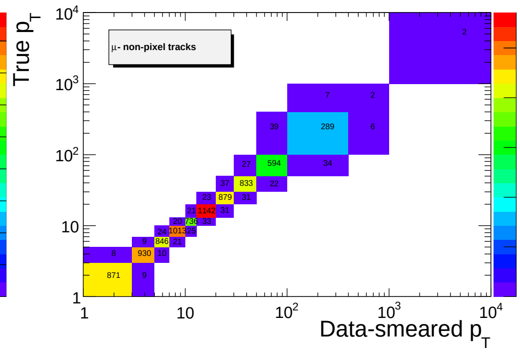

(d) Data $\mu-$ non-pixel

Figure B.3: Resolution matrices

As it can be seen, the resolution matrices are close to diagonal, but some migration effects are present, however they affect only the neighbouring bins.

Unfolding The data analysis technique called unfolding has been described in [63], [64]. In this analysis we use the RooUnfold package (see [65]). It provides several algorithmic approaches to the problem, out of which we have chosen the Bin-by-Bin unfolding as a baseline (the most simple and least robust method) and Bayesian unfolding as a more sophisticated technique.

The following Figure (Fig. B.4) shows the result of unfolding together with the measured p_T spectra.

Clearly, the effect is small. For a more detailed study next plots (Fig. B.5) show the ratio of unfolded p_T to measured p_T, separately for each technique. It seems that the Bayesian unfolding method yields more stable results with smaller errors, so, despite the simplicity of bin-by-bin technique we chose to use the Bayesian results, as the uncertainty in each bin does not exceed 1%.

We can consider the ratios shown in Fig. B.5 as correction factors that should be applied to each bin to obtain unfolded p_T spectrum. However we are interested not in the separate spectra for each charge sign, but in the charge ratio spectrum. Therefore, the next

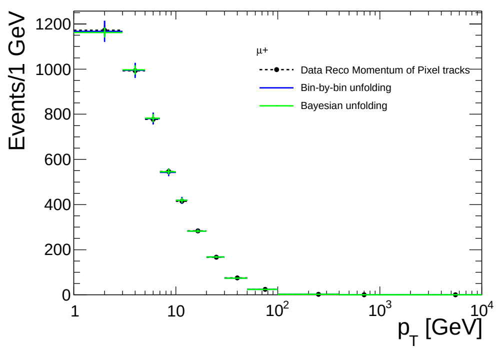

(a) Data $\mu+$ pixel

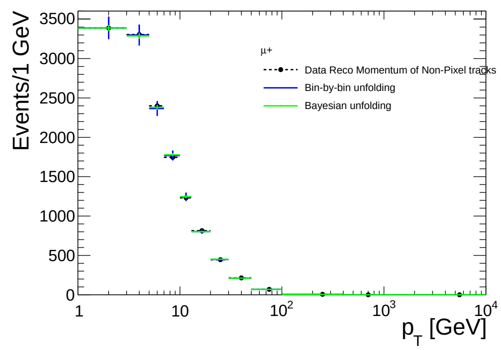

(b) Data $\mu+$ non-pixel

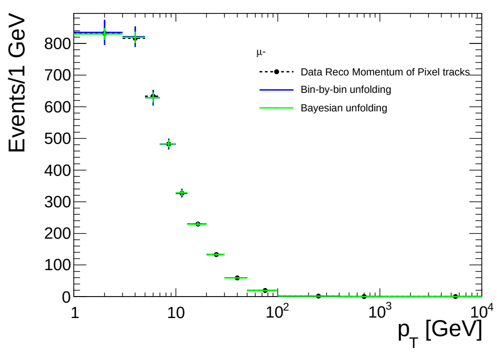

(c) Data $\mu-$ pixel

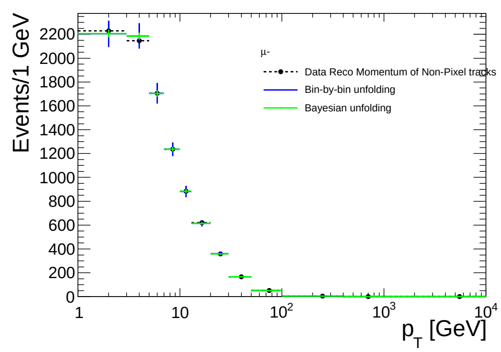

(d) Data $\mu-$ non-pixel

Figure B.4: Transverse momentum spectra

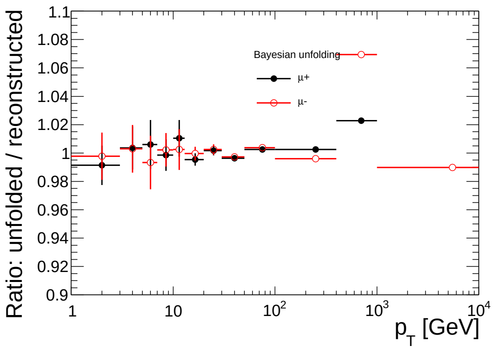

(a) Pixel tracks, Bayesian unfolding

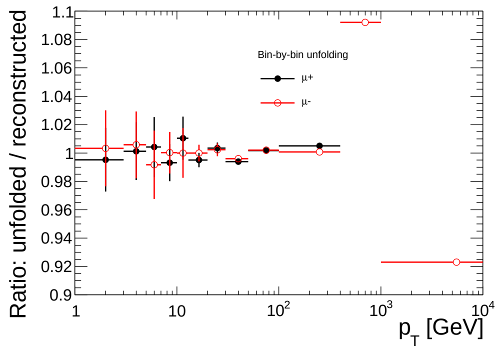

(b) Pixel tracks, Bin-by-bin unfolding

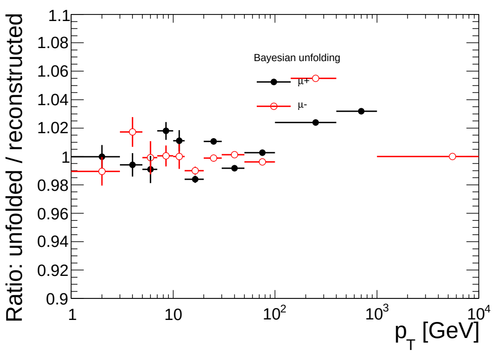

(c) Non-pixel tracks, Bayesian unfolding

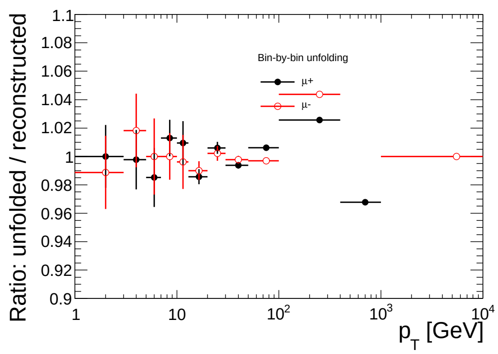

(d) Non-pixel tracks, Bin-by-bin unfolding

Figure B.5: Ratio of transverse momenta - unfolded to reconstructed transverse momentum plots (Fig. B.6) show the "ratio of ratios" (unfolded charge ratio divided by the measured charge ratio), from which we can try to extract correction factors for the final charge ratio spectrum. As expected, the correction factors for pixel tracks are much closer to 1.0 - much

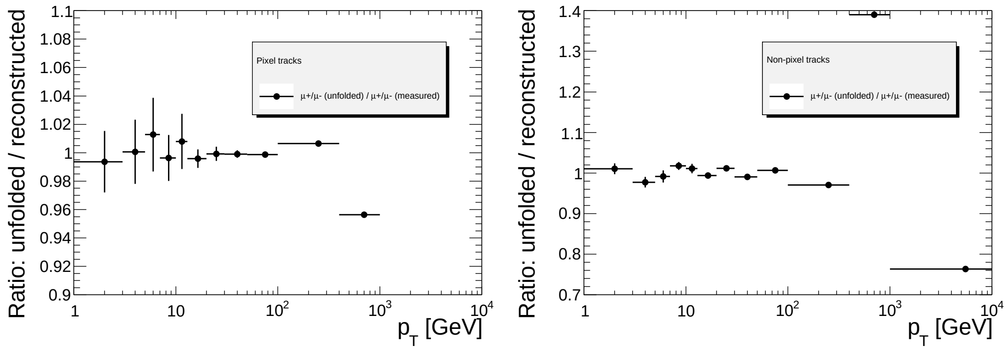

(a) Pixel tracks

(b) Non-pixel tracks

Figure B.6: Ratio of transverse momenta ratios - results of Bayesian unfolding from Fig. B.5 for positive and negative muons divided by each other.

less migration occurs (i.e. the p_T is much better measured) than for non-pixel tracks. The uncertainty related to statistical fluctuations is well below 1% level.

The expected correction factors from unfolding and correcting for detector effects turn out to be close to 1.0. Any deviations from this value are anyway suppressed by uncertainty caused by detector mis-alginments mentioned before, and therefore these corrections are not applied in further steps.

Systematic uncertainty The first option under consideration would be to take the statistical uncertainty of each correction factor as a systematic uncertainty of the method. The statistical uncertainty of each factor is the actual limit down to which we can understand the effect. In this case it is below 1%.

Another contribution may be the result of possible method bias. To determine if it may be significant, a toy test was performed.

The Monte Carlo samples, that were used to train the method, was divided into two equal parts. One part was used for training, whereas the events from the other part were used to mimic the measured data. Unfolding of such sample should result in a distribution very close to the true distribution used in training. Any differences found here may be a potential source of systematics of the method. This effect is estimated to be below 0.5%.

B.3 Final remarks

In the final step of this analysis, the ratios of pixel and non-pixel tracks are combined. Systematic uncertainties are added as uncorrelated. The resulting charge ratio with respect to muon momentum, measured in the center of ATLAS is presented in Fig. B.7. This result is dominated by statistical uncertainty. It was expected to decrease very significantly after adding data from Fall 2009 to this analysis. Most systematic uncertainty contributions are also expected to shrink with larger statistics available. However, the dominant contribution from detector misalignment, that strongly affects this measurement at large momenta is

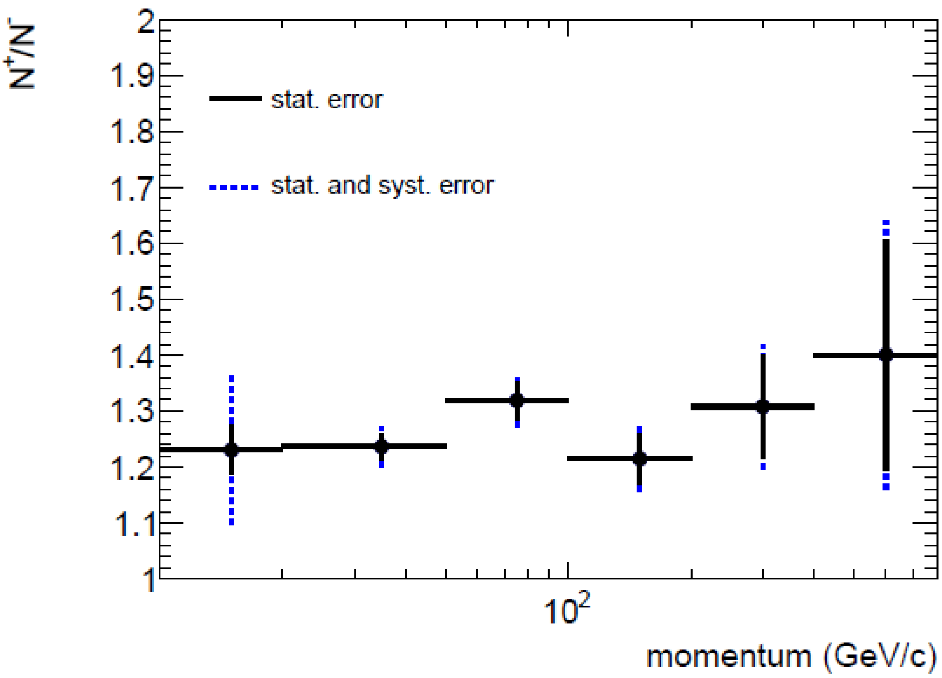

Figure B.7: Final cosmic muons charge ratio spectrum with respect to muon momentum (from [62])

limited by alignment systematics biasing the curvature measurement. This was expected to improve, after new alignment constants become available. Currently, a result with two times larger uncertainty than available from L3 Collaboration, was obtained.

The ATLAS Collaboration however has never published results of presented measurement with Fall 2009 cosmic data, neither with new alignment constants. In November 2009 the collision data became available and there was no manpower to conduct this analysis any further, as there was much work to be done with detector commisioning and early physics analyses. The methods for improving the cosmic muon charge ratio measurement are however in place, ready to be applied when needed. The unfolding technique may be also used to obtain the charge ratio spectrum with respect to muon momentum at sea level, directly comparable with earlier measurements.

Appendix C

Details on electron identification

The identification of electron candidates, mentioned already in Section 2.3, is based on cuts, applied to a number of variables, known for their good discrimination power against possible sources of fake electrons, resulting from QCD jets. The set of variables is presented in Table C.1. The detailed cuts are optimised and tabulated versus detector region in pseudorapidity and versus electron transverse momentum. They are not presented here.

Type	Description
	Loose cuts
Detector acceptance	$\|\eta\| < 2.47$ with the exception of transition region ($1.37 < \|\eta\| < 1.52$).
Hadronic leakage	Ratio of transverse energy in the first layer of hadronic calorimeter to the transverse energy of the electromagnetic cluster (in $\|\eta\| < 0.8$ or $\|\eta\| > 1.37$) or ratio of transverse energy in hadronic calorimeter to the energy of electromagnetic cluster (in $\|\eta\| > 0.8$ and $\|\eta\| < 1.37$).
Second layer of EM Calorimeter	Lateral width of the shower, ratio of energies of cell-sets (in $\eta \times \phi$) 3×7 to 7×7.
	Medium cuts
Strip layer of EM Calorimeter	Lateral shower width in strips, Ratio of energy difference between first and second maximum deposit over the sum of these energies.
Track quality criteria	At least one pixel hit, At least 7 hits in silicon detectors (Pixels and SCT), Transverse impact parameter $d_0 < 5$ mm.
Track - cluster matching	$\Delta\eta$ between track extrapolated to the strip layer and electromagnetic cluster.
	Tight cuts
B - layer hit	At least one hit in B-layer (if the candidate track does not cross a dead B-layer module).
Track - cluster matching	$\Delta\phi$ between track and cluster in the second layer of EM Calorimeter, Ratio of cluster energy to track momentum.
Transition Radiation Tracker	Total number of hits in the TRT, Ratio of the number of high-threshold TRT hits to the total number of TRT hits (within TRT acceptance of $\|\eta\| < 2.0$).

Table C.1: Variables used in cut-based electron identification [34].

List of Figures

List of Tables